Excited state spatial distributions in a cold strontium gas

GRAHAM LOCHEAD

How to cite:

LOCHEAD, GRAHAM (2012) Excited state spatial distributions in a cold strontium gas. Doctoral thesis, Durham University.

Excited state spatial distributions in a cold strontium gas

Graham Lochead

This thesis describes the development of a new technique for measuring the spatial distribution of Rydberg atoms in a cold strontium gas. Strontium atoms are cooled and trapped in a magneto-optical trap and coherently excited to Rydberg states in a two-photon, three-level ladder scheme. Several methods of stabilizing the frequency to the cooling transition are discussed and characterized. A frequency stabilization scheme based on electromagnetically-induced transparency for the second laser required for Rydberg excitation is also explained. The Rydberg population dynamics are studied experimentally and modeled using an optical Bloch equation simulation.

The divalent nature of strontium allows doubly excited "autoionizing" states to be accessed using resonant optical excitation. These states ionize in sub-nanosecond timescales, with the ions recorded on a micro-channel plate being proportional to the amount of Rydberg atoms. Translation of an autoionizing laser focused to a waist of 10 μm gives a spatially resolved Rydberg signal. A two-dimensional map of the Rydberg spatial distribution has been made using this autoionizing microscopy technique.

Excited state spatial distributions in a cold strontium gas

Graham Lochead

A thesis submitted in partial fulfilment
of the requirements for the degree of
Doctor of Philosophy

Department of Physics
Durham University

December 16, 2012

Contents

List of Figures

Declaration

I confirm that no part of the material offered has previously been submitted by myself for a degree in this or any other University. Where material has been generated through joint work, the work of others has been indicated.

Graham Lochead
Durham, December 16, 2012

Acknowledgments

I only decided to do a PhD after accidentally going to a lunchtime talk by, my now supervisor, Matt Jones. In that talk he convinced me that studying Rydberg atoms (something I'd not heard of up until that point) in strontium (an element I'd never heard of) was truly interesting. If I'd gone somewhere else for lunch that day then this thesis would not exist and my life would be very different. For persuading me to do a PhD, and putting up with my constant bothering over the years, I must thank Matt immensely.

The original PhD student on the strontium project, and my several year-long lab partner, James Millen must be thanked for introducing me to, and aiding me in, the world of experimental cold atomic physics. His constant enthusiasm and upbeat attitude made the lab a fun place to be. The late-night data marathons we endured will never be forgotten. Team strontium has now grown with the addition of Danielle Boddy and Daniel Sadler taking up the baton in my stead, adding their unique skills to the group. It was a pleasure to work with them both.

The AtMol research group of which I have been apart of for the last four years has been an amazing place to work, with everyone friendly and willing to discuss things from overarching physical concepts to technical minutiae. In particular, I would like to thank my second supervisor, Charles Adams, for scientific guidance; Ifan Hughes for explaining many things and helping with error analysis; Jon Pritchard for discussions of Rydberg physics and three-level atoms; Ulrich Krohn for his technical expertise; and Rich Abel for his banter. I am also heavily indebted to all those who proof-read this thesis.

Outside of physics, the friends I have made at Ustinov College, while playing frisbee, or from other places besides, have my gratitude for keeping me sane during the past four years.

Last, but not least, my family have my eternal love for the continued understanding and encouragement they have given me.

To my family, for the love and support
they give me in everything I attempt.

Chapter 1

Introduction

The aim of the work in this thesis is to develop a technique which is able to measure the spatial distribution of a cold Rydberg ensemble. For the spatial correlations we wish to study - those created by the dipole blockade - the ensemble has to be coherently excited to the Rydberg state, requiring careful control of the laser system and stray electric/magnetic fields. The technique also needs to be decoupled from the excitation dynamics of the system, so as not to affect it. A property of divalent atoms, strontium atoms in the case of this thesis, called autoionization [1] will be used to facilitate the creation of a spatial Rydberg probe.

Rydberg atoms

Atoms with a bound electron in a high principal quantum number ($n > 10$) state are referred to as Rydberg atoms [2]. These states are characterised as having properties quite different to low lying states with large orbital radii $r \propto n^2$; long radiative lifetimes $\tau \propto n^3$; and a close spacing in energy to nearby states $\Delta \propto n^{-3}$ [3].

Rydberg atoms were instrumental in humankind's understanding of the theory of the atom [3]. Following the invention of the laser [4], spectroscopy of Rydberg states in cavities lead to fundamental tests of atom-light interactions [5, 6].

Combining laser cooling [7–9] with Rydberg states enabled the study of a wide range of phenomena: ultra-cold neutral plasmas [10]; the giant Kerr effect [11]; molecular dimers [12]; and circular Bohr-like wavepackets [13] to name a few.

There is great interest currently in using Rydberg atoms for quantum computing/simulation/information processing. The idea of using Rydberg atoms for quantum computing was put first forward by D. Jaksch *et al.* [14]. Ultra-cold Rydberg atoms are an attractive proposition for several reasons: their long coherence times, tens of microseconds depending upon the state used; their simple, well established trapping schemes; and the fact they are less sensitive to coupling to external fields compared to ions, because they are neutral atoms. Compared to ground state atoms the interactions between Rydberg atoms are many orders of magnitude stronger, and much longer range. By selecting which Rydberg state to excite to, the interaction strength can be controlled [15]. The coupling scheme required to create qubits out of Rydberg atoms is based upon long-range dipole-dipole interactions [15].

The dipole-dipole interaction causes the suppression of excitation and entanglement of atoms within a certain region, referred to as the dipole blockade [16]. The distance over which only one excitation is permitted is called the “blockade radius”. The origin of the dipole blockade will be described in section 2.1.2. The blockade mechanism is caused by one atom excited to a Rydberg state shifting all other atoms out of resonance with the driving laser field via the dipole-dipole interaction. The dipole blockade causes a spatial correlation of the Rydberg atoms [17]. This is illustrated in figure 1.1a.

The dipole blockade between Rydberg atoms was initially observed between two individual atoms held in microscopic dipole traps [18, 19]. In these

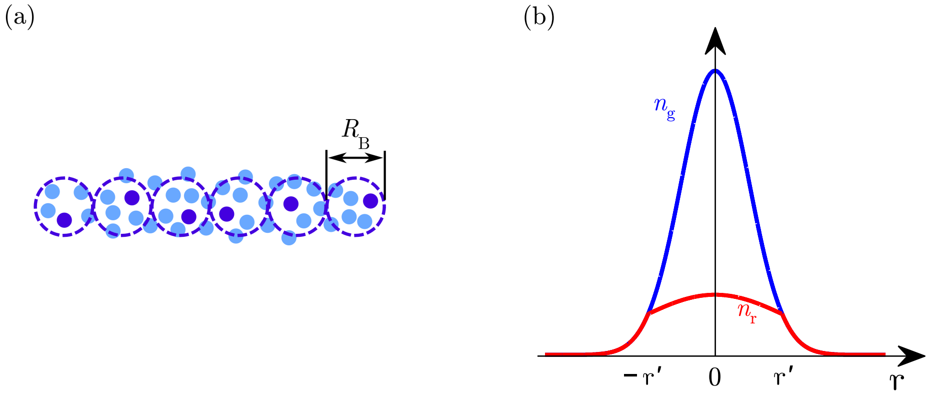

Figure 1.1: (a) A series of blockade regions where only one Rydberg excitation is allowed. The blue dots are the ground state atoms and the purple dots are the Rydberg atoms. The purple, dashed circles show the regions within which only a single Rydberg excitation is allowed due to the dipole blockade. The blockade radius is labeled as R_{B}. It should be noted that the blockade radius is not the orbital radius of the Rydberg electron, for realistic experimental parameters the blockade radius is much larger. (b) The effect of interactions on the Rydberg density. The blue line indicates a Gaussian ground state density, n_{g}, whereas the red line indicates the Rydberg density, n_{r}, with strong dipole-dipole interactions.

dipole traps, entanglement between the two atoms has been achieved [20] and a controlled NOT gate has been realized [21].

The dipole blockade has also been observed in extended ensembles [22–25]. Figure 1.1b illustrates how the Rydberg density can differ to the ground state density because of the interactions. The ground state density in this example is a Gaussian distribution. In the centre of the Gaussian ($r = 0$) the density is the highest and there are several ground state atoms per blockade radius. Only one of these ground state atoms can be excited, hence the Rydberg density is much reduced compared to the ground state density. Between $r = 0$ and the distance where the average inter-particle spacing is the blockade radius, i.e. where there is only one ground state atom per blockade radius, $|r'|$, the ground state density decreases and therefore the amount of ground state atoms per blockade radius decreases, such that the difference between ground state and Rydberg state densities reduces. When $r > |r'|$ the ground state density has reached the point where the average inter-particle spacing is more than the blockade radius, i.e. there is only one ground state atom per blockade radius, hence there are no more blockaded Rydberg atoms and the Rydberg density follows the ground state density.

These strong interactions have lead to proposals for creating a single photon source using Rydberg atoms [26], with recent experiments confirming this [27, 28]. Applying microwave fields to these quantum optics experiments allows control over the properties of the photons stored in the medium [29].

Careful control of the parameters of the excitation lasers used to create a strongly interacting gas can imprint crystal structures within the Rydberg atom positions [30, 31]. Strong repulsive interactions are required to create these effects. The energy level scheme and Rydberg atom position for this are illustrated in figures 1.2a and 1.2b respectively. The repulsive interaction splits the energy level crossing of the multiply excited Rydberg states. By adiabatically sweeping the detuning of the excitation laser a state with a predetermined amount of Rydberg atoms can be created [30]. Due to the repulsive interactions the Rydberg atoms are located as far apart in the cloud as possible, creating a crystalline structure. With attractive interactions the many-body energy levels shift in the opposite direction, and the first adiabatically excited state after zero is the maximally excited state [32], leading to the creation of large scale Greenberger-Horne-Zeilinger (GHZ) states [33].

Studying these spatial correlations is garnering significant interest, with several groups investigating them using a variety of techniques: imaging the probe beam [34–37]; using high numerical aperture lenses to resolve individual lattice sites [38–40]; and field ionizing the Rydberg atoms with a pointed electrode tip close to the atoms and then imaging the ions on a spatially

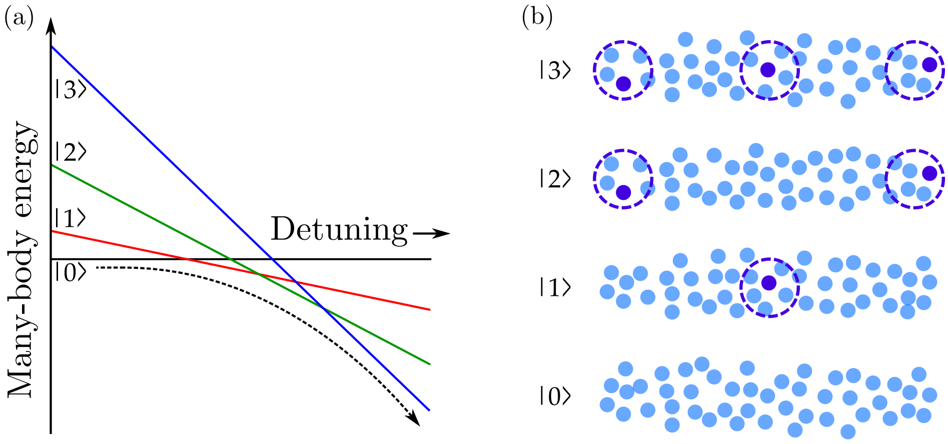

Figure 1.2: (a) Many-body energy level shifts due to repulsive interactions. The dashed line shows the state which is adiabatically excited. (b) Dynamical crystallization of Rydberg excitations due to shaped excitation pulses. As the detuning is swept from negative to positive, the amount of Rydberg excitations increases. To minimize energy the excitations are created as far as possible from each another. Modified from [30].

resolving micro-channel plate [41].

There has also been intense theoretical work concerning spatial dependencies of interacting Rydberg systems: non-local, non-linear optics [42]; creation of "matter-wave bullets" [43]; generation of supersolid-like states [44]; and production of quantum simulators [45].

Thesis layout

In previous work using the same vacuum chamber [46] we have studied the spectral and temporal dynamics of a cold strontium Rydberg gas [47, 48]. The work in this thesis builds upon these results by introducing the ability to coherently excite the Rydberg cloud and add spatial resolution to the measurements, the structure is as follows:

- Chapter 2 describes the properties of Rydberg atoms, the strong interactions that arise between them and what effect this has on the Rydberg state population. The coherent excitation to Rydberg states is theoretically considered, with special regard given to dephasing effects caused by finite laser linewidth.

- Chapter 3 has an overview of the laser frequency stabilization techniques necessary for the creation of a cold strontium gas and the coherent excitation to Rydberg states. For the laser addressing the ground state to first excited state transition several techniques are described. For the coupling laser used to excite to Rydberg states an EIT based frequency stabilization technique is employed and explained.

- Chapter 4 summarizes the cold atom setup: creation of a cold atom cloud; excitation to a Rydberg state; and detection of the ions created from the Rydberg atoms. Modeling of the coherent population dynamics is described.

- Chapter 5 describes autoionizing microscopy of a Rydberg gas and the spatial effects seen as a result of this technique.

- Chapter 6 details the attempt at seeing long-range dipole-dipole interactions in the Rydberg cloud and discusses how to move into this regime in the future. Spatial excitation shaping using the Stark effect is also described.

- Chapter 7 concludes this thesis, highlights the major achievements and discusses future directions this research could take.

Chapter 2

Coherent Rydberg excitation theory

As discussed in the previous chapter, the strong dipole-dipole interactions between Rydberg atoms lead to controllable correlations interesting for many areas of physics. The first half of this chapter will describe how the dipole-dipole interaction arises and some more general properties of Rydberg states.

The second half of this chapter will focus on the excitation to these Rydberg states using laser fields in a two-photon, three-level transition. The subtleties of working in a three-level system will be discussed with respect to the transmission properties of the lower transition laser field and the population in the Rydberg state. A simulation of the population dynamics of the system, which is used to model experimental results, will be described also.

2.1 Rydberg atoms

Rydberg atoms are atoms with a valence electron excited to a high principal quantum number, $n > 10$ [2]. They exhibit properties which scale strongly with n, such as orbital radius $\propto n^2$, or radiative lifetime $\propto n^3$ [3]. For hydrogen, where there is only one electron, these scalings are exact. For heavier alkali metals, such as rubidium, the core electrons interact with the Rydberg electron wavefunction and a small modification has to be made. The modification is called a quantum defect and is modeled using an effective quantum number $n^* = n - \delta_l$, where δ_l is the quantum defect of the Rydberg electron with orbital angular momentum l. To get the scaling for heavier elements n can be replaced by n^*. For higher l states, $l > 3$, the Rydberg wavefunction overlap with the core is very small such that $\delta \approx 0$ and these states are described as "hydrogen-like".

Strontium, the element used in this thesis, has two valence electrons. In this situation we consider that one valence electron is excited to a Rydberg state and the other electron remains in its ground state. Doubly excited states are possible and are considered in section 4.3. Singlet-triplet mixing and other configuration effects [49] cause additional perturbations to the Rydberg wavefunction. These perturbations are pronounced close in energy to the perturbing state, which are generally quite low in n, below 20 or so [49]. For the high n states explored in this thesis these perturbations can be incorporated into the quantum defect of the state.

To calculate Rydberg state energies, lifetimes, polarizabilities, and interaction strengths a single electron model has been developed [46, 50] based upon the work in [51]. The single electron model is a product state of the Rydberg wavefunction and a core wavefunction moving in a model potential [52]. In [51] the authors compared the results of the single electron model to Stark maps at $n = 12$ for strontium and achieved good agreement. In previous experiments we extended the model to higher n and compared simulated Stark maps at $n = 56$ and $n = 80$ to experimental data [47]. The agreement is very good indicating that the single electron model is a good approximation, even at high n where state mixing occurs. The single electron model enables us to calculate the strengths and signs of Rydberg states dipole-dipole interactions, as discussed in the next section.

It should be noted that a multi-channel quantum defect treatment (MQDT) could be performed on the system presented here for higher accuracy results [53]. However, this MQDT analysis is beyond the scope of this thesis and is not used.

2.1.1 Dipole-dipole interactions

As mentioned in chapter 1 the interactions between Rydberg atoms are a current source of interest. The origin of these interactions will be explained in this section. The following treatment for the interaction is set out in [50, 54, 55], and is in atomic units.

Consider a pair of atoms excited to the same Rydberg state $|n_i l_i n_i l_i\rangle$. The Rydberg atoms exert a position dependent energy shift on one another due to the Coulomb interaction between the Rydberg electrons. The Hamiltonian of the system is

$$\mathscr{H} = \mathscr{H}_{\mathrm{A}} + \mathscr{H}_{\mathrm{int}}(R) \ , \tag{2.1}$$

where $\mathscr{H}_{\mathrm{A}}$ is the Hamiltonian of the atom pair at infinite separation, and $\mathscr{H}_{\mathrm{int}}(R)$ is the position dependent energy interaction, where the atoms are separated by R, see figure 2.1a. The interaction Hamiltonian can be found in [50].

If $\mathscr{H}_{\mathrm{int}}(R)$ is small compared to $\mathscr{H}_{\mathrm{A}}$ then the system can be treated perturbatively. Physically, this corresponds to the atoms being far apart ($R > 2\ \mu$m). At separations less than $\approx 2\ \mu$m the system becomes much more complicated and molecular bound states start appearing [12, 56]. A diagonalization of the entire Hamiltonian is required in this case. At the densities accessible in our experiment the inter-particle separation means the perturbative approach is sufficient.

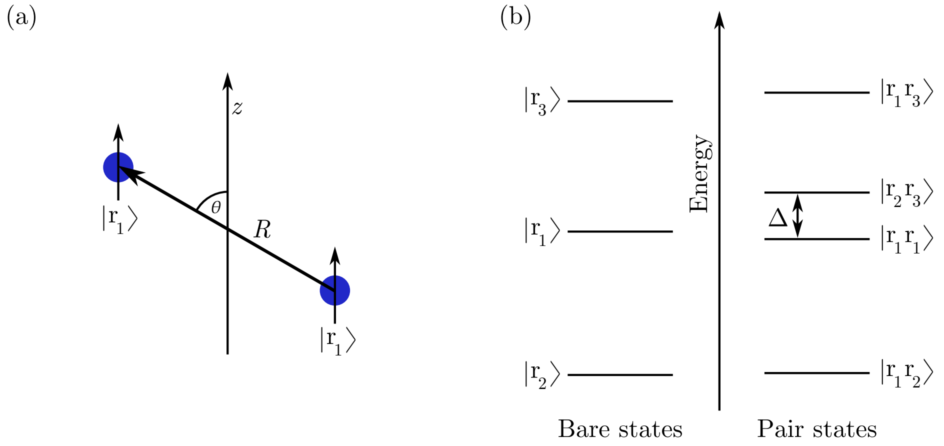

Figure 2.1: (a) Two dipoles aligned along the quantization axis z, separated by R, with an internuclear axis at an angle θ to the quantization axis. (b) The energy of the excited state $|\mathrm{r}_1\rangle$, and the two closest in energy dipole coupled states $|\mathrm{r}_2\rangle$ and $|\mathrm{r}_3\rangle$ shown in the single bare atom basis. The pair state basis due to the dipole-dipole interaction is shown on the right hand side. The energy difference, Δ, between two pair states is shown.

The interaction Hamiltonian can be expanded as a series of multipoles [57] and treating the expansion perturbatively, terms of the same power of R are grouped together, leading to an expression for the energy shift, ΔE, as

$$\Delta E = \sum_N \frac{C_N}{R^N} \ . \tag{2.2}$$

The effect of the higher order terms is minimal in the separations of interest to this experiment and the expansion is therefore truncated to the first few terms.

In the perturbative approach the first term that arises in the expansion is C_3, the first order dipole-dipole interaction. The C_3 coefficient is zero as it does not couple states of the same l. The next term is C_5, the first order quadrupole-quadrupole interaction. The C_5 coefficient is non-zero for most initial states, though at separations of interest to our experiment is smaller than the C_6 contribution to the energy shift, and is therefore neglected. The C_6 coefficient arises due to the second order dipole-dipole interaction (van der Waals interaction), and at the separations in our experiment is the dominant interaction. The rest of the treatment presented here will only deal with the C_6 coefficient. The energy shift due to interactions is then

$$\Delta E_{\mathrm{vdW}} = \frac{C_6}{R^6} \, . \tag{2.3}$$

The effect of the C_6 interaction term is to couple the initial pair state to other pair states, see figure 2.1b. The final pair state is made of states of different n and/or l. The difference in energy between the final pair state and the initial pair state is $\Delta = E_{\mathrm{r}_2} + E_{\mathrm{r}_3} - 2E_{\mathrm{r}_1}$, referred to as the energy or Förster defect. For simplicity the quantization axis of the two atoms is aligned along the internuclear axis, i.e. $\theta = 0$ in figure 2.1a. The angular dependence of the interaction will be discussed later.

The C_6 coefficient is determined from the sum over all states dipole coupled to the initial states, i.e. $|n_{i1}l_{i1}n_{i2}l_{i2}\rangle \rightarrow |n_{f1}l_{f1}n_{f2}l_{f2}\rangle$, where $n_{i1/2}$ and $l_{i1/2}$ are the n and l states of the initial atom pair and $n_{f1/2}$ and $l_{f1/2}$ are the n and l of the final pair state. Note that n_{f1} and n_{f2} can be different, as can l_{f1} and l_{f2}. Formally the sum is

$$C_6 = -\sum_{\substack{n_{f1},l_{f1}\\ n_{f2},l_{f2}}} \frac{\langle n_{i1}l_{i1}n_{i2}l_{i2}|\hat{r}_1\hat{r}_2|n_{f1}l_{f1}n_{f2}l_{f2}\rangle\langle n_{f1}l_{f1}n_{f2}l_{f2}|\hat{r}_1\hat{r}_2|n_{i1}l_{i1}n_{i2}l_{i2}\rangle}{\Delta_{n_{i1}l_{i1}n_{i2}l_{i2}n_{f1}l_{f1}n_{f2}l_{f2}}} \, , \tag{2.4}$$

where $\hat{r}_k$ is the dipole operator for atom k in atomic units. The energy defect with n for the closest in energy of each of the three dipole coupled channels for the 5$s$$n$d $^1\mathrm{D}_2$ series is shown in figure 2.2a. Due to the inverse relationship with energy defect, final pair states close in energy to the initial pair state dominate the sum, i.e. the $|n\mathrm{p}, (n-2)\mathrm{f}\rangle$ channel.

The sign of the interaction is dependent upon the sign of the dominant channel energy defect. If the defect is positive then attractive interactions are observed, if negative, the interactions are repulsive.

The magnetic sub-levels of the initial pair state have so far been neglected. The coupling between magnetic sub-levels is incorporated as a weighting to equation 2.3 which becomes $\Delta E_{\mathrm{vdW}} = \frac{D_\theta C_6}{R^6}$ [55]. The D_θ term contains the coupling between the magnetic sub-levels and is bounded between 0 and 1. Different initial magnetic sub-levels have different D_θ. The analytic expression for D_θ can be found in [55].

Although $J = J_1 + J_2$ is not conserved between initial and final pair states, the sum of their m_{J}, i.e. $M_{\mathrm{J}} = m_{\mathrm{J}1} + m_{\mathrm{J}2}$, is [50, 55]. For example, in the 5snd $^1\mathrm{D}_2$ state, if the initial atoms are both in the $m_{\mathrm{J}} = +2$ state, then $M_{\mathrm{J}} = +4$. The contribution from the $|\mathrm{n}_{f1}\mathrm{p}, n_{f2}\mathrm{p}\rangle$ channel is therefore zero in this case as it cannot satisfy this condition, affecting the interaction shift for this initial m_{J} pair. However, the $|\mathrm{n}_{f1}\mathrm{p}, n_{f2}\mathrm{p}\rangle$ channel is not the dominant channel, so does not affect the shift greatly.

The interaction strength for most initial m_{J} pair states is similar. However, for the 5snd $^1\mathrm{D}_2$ series for example, the $|m_{\mathrm{J}_1}, m_{\mathrm{J}_2}\rangle = |+2, -2\rangle$ state has a very small D_θ, and the interaction shift for this initial pair state is therefore very small. States with very low interaction shift are referred to as a Förster zero state [58]. These Förster zero states can have a strong effect on the total interaction.

So far the analysis has ignored angular effects between the dipoles. The individual atoms are excited with a well controlled m_{J} as they have been excited by the same laser, assumed to have perfect polarization. For initial dipoles whose internuclear axis is aligned along the quantization axis, i.e. $\theta = 0$ in figure 2.1a the interaction is between two atoms of the same m_{J}. However, if the internuclear axis and quantization axis are not aligned, i.e. $\theta \neq 0$, the projection of one dipole upon the other, due to the angle, means all possible two atom eigenstates will be populated, i.e. all magnetic sub-levels. An angle between the dipoles causes a superposition of all initial m_J pair states. The magnitude of the angle determines the amount of each pair state present. Figure 2.2b shows the interaction as a function of angle between the dipoles for the 5snd ^{1}D$_2$ stretched state. A clear variation of the interaction strength is seen, with the largest difference being a reduction of a factor of four from the $\theta = 0$ case.

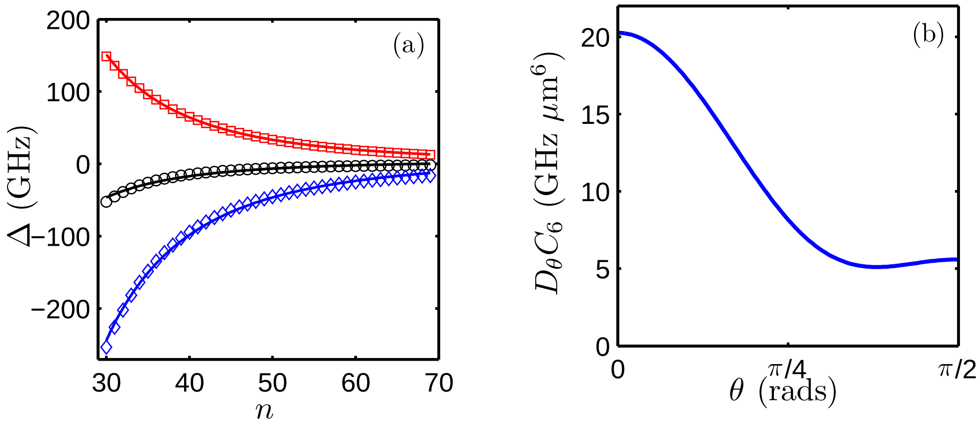

Figure 2.2: (a) The Förster defect of the three coupled final pair states of the 5snd ^{1}D$_2$ series. Black circles are the $|n\mathrm{p}, (n-2)\mathrm{f}\rangle$ final pair states, blue diamonds the $|n\mathrm{p}, n\mathrm{p}\rangle$, and red squares the $|n\mathrm{f}, n\mathrm{f}\rangle$. The solid lines are n^{-3} fits. (b) The angular dependence of the $D_\theta C_6$ coefficient of the 5s56d ^{1}D$_2$ state. Data in the graphs were calculated by C.L. Vaillant.

For a three-dimensional atom cloud the angle the quantization axis makes to the internuclear axis of the initial pair state is random. Therefore, the total interaction is the angular mean of the interaction. If the initially prepared state is a 5sns ^{1}S$_0$ state, then there is no angular dependence as there is only a single initial m_J sate that can be populated. The 5sns ^{1}S$_0$ state interaction is therefore isotropic. For the 5snd ^{1}D$_2$ state the angle between dipole clearly has an effect and will need to be addressed in the experimental setup, section 5.3.1.

C_6 calculations for our experiment

Due to our excitation scheme, section 2.2, the accessible initial Rydberg states in our experiment are the 5sns ^{1}S$_0$ and the 5snd ^{1}D$_2$ series. For the 5sns ^{1}S$_0$ series only a single final channel couples, that of the $|$5sn_{f1}p,5sn_{f2}p$\rangle$, due to the dipole coupling. For the 5snd ^{1}D$_2$ series three final channels couple, the $|$5sn_{f1}p,5sn_{f2}p$\rangle$, $|$5sn_{f1}f,5sn_{f2}f$\rangle$, and $|$5sn_{f1}p,5sn_{f2}f$\rangle$. At higher n the energy defects decrease (figure 2.2a) leading to stronger interactions. The tunability of the interaction is clear from this: since the excitation is a resonant process, by exciting to higher or lower n states, the strength of the interaction can be controlled.

The 5sns ^{1}S$_0$ and 5snd ^{1}D$_2$ series have different signs with the 5sns ^{1}S$_0$ series attractive, and the 5snd ^{1}D$_2$ series repulsive [50], opposite to the situation in rubidium/caesium. The magnitude of interactions at the same n are similar though.

Detailed calculations were carried out in [50] using the single electron model discussed above. The energy variation of the $D_\theta C_6$ coefficient can be fitted as a function of n using an empirical formula, given in table 2.1. The C_6 coefficient scales as approximately n^{11} because it is dependent upon the square of the dipole matrix element of atom 1, $\mu_1^2 = |\langle n_{i1}l_{i1}|\hat{r}_1|n_{f1}l_{f1}\rangle|^2$, multiplied by the dipole matrix element of atom 2 squared. Since the dipole matrix element scales as approximately n^2, this leads to a scaling of approximately n^8. The final power of three comes from the Förster defect which scales as approximately n^{-3}. The deviation from a pure n^{11} scaling is due to the dipole matrix elements and energy defects not having a pure n^2 and n^{-3} scaling, respectively.

Series	$\boldsymbol{a}$	$\boldsymbol{b}$	$\boldsymbol{c}$
5s*n*s $^1S_0$	3.2×10^{-3}	-0.51	3.6
5s*n*d $^1D_2$	-1.65×10^{-3}	0.365	-7.05

Table 2.1: The scaling of the C_6 coefficient with n for the 5s*n*s $^1S_0$ and 5s*n*d $^1D_2$ series. The dominant n^{11} scaling has been factored out to leave the fit as $C_6 = n^{11}(an^2 + bn + c)$. C_6 is calculated in atomic units. To convert these values to GHz μm^6 multiply by 1.4448×10^{-19}. C_6 is for the "stretched state" (state of maximum $|m_{\mathrm{J}}|$) in both cases, and is valid over the range $30 < n < 70$. Fits taken from [50].

2.1.2 Dipole blockade

The strong van der Waals interactions lead to interesting many-body physics via a process called the dipole blockade [16]. The energy scheme explaining the dipole blockade is shown in figure 2.3a. Two atoms initially in the ground state are considered. A laser resonant with a Rydberg transition addresses the atom pair simultaneously. The effect of this laser field on the atom pair now depends on the separation of the two atoms. If the two atoms are well separated then both atoms are excited to the Rydberg state. However, if the atoms are close together then the van der Waals interaction shifts the doubly excited state energy out of resonance with the laser so it won't be populated. Only one atom can be excited and the system is in an entangled state of $\frac{1}{\sqrt{2}}(|\mathrm{gr}\rangle + |\mathrm{rg}\rangle)$, under the assumption that both atoms are excited in an indistinguishable manner by the same laser beam. The interaction shift required for the dipole blockade depends upon the Rabi frequency of the driving laser field, the linewidth of the state, and the phase fluctuations of the driving laser field. The interaction induced shift has to be larger than these broadening mechanisms. The separation where the dipole blockade occurs is found by rearranging equation 2.3, and setting $\Delta E = \gamma_{\mathrm{b}}$, where γ_{b} is the largest of the broadening mechanisms mentioned previously. The "blockade radius", is therefore

$$R_{\mathrm{B}} = \sqrt[6]{\frac{D_\theta C_6}{\gamma_{\mathrm{b}}}} \,. \tag{2.5}$$

In a larger ensemble, where there are several ground state atoms in the blockade radius, still only one is excited. This situation is generally modeled using the "superatom" model [59]. In the superatom model, the system of N atoms within the blockade radius is modeled as an effective two-level system between $|\psi^{(N,0)}\rangle$ and $|\psi^{(N,1)}\rangle$, where $|\psi^{(N,0)}\rangle = |\mathrm{g}_1, \mathrm{g}_2, ..., \mathrm{g}_N\rangle$, i.e. the N-body ground state, and $|\psi^{(N,1)}\rangle = \frac{1}{\sqrt{N}} \sum_k |\mathrm{g}_1, \mathrm{g}_2, ..., \mathrm{r}_\mathrm{k}, ..., \mathrm{g}_N\rangle$ is the N-body ground state with one excitation. The effective two-levels are coupled by a Rabi frequency of $\sqrt{N}\Omega$. The usefulness of the superatom model is to remove the need for a complex many-body theory.

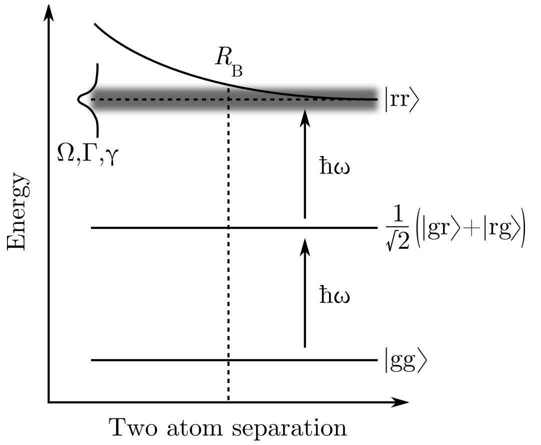

Figure 2.3: The dipole blockade between two Rydberg atoms. The black line shows the shift of the doubly excited state, with the horizontal dashed line a non-interacting doubly excited state. The grey, shaded region shows the width of the largest of the driving Rabi frequency (Ω), state linewidth (Γ), or the laser linewidth (γ). R_B is the blockade radius where the interaction shift is larger than the broadening mechanisms, allowing only one excitation to be present.

2.2 Coherent excitation to Rydberg states

To access the Rydberg states described above, a two-photon, three-level, ladder type scheme is used. Two photons are used to make the scheme experimentally tractable, as a single photon transition from the ground state to the Rydberg state directly would require a ≈ 218 nm laser. The wavelengths of the lasers used and the states they access are shown in figure 2.4a.

A more generalized three-level system is shown in figure 2.4b, where the 461 nm laser beam is referred to as the probe beam, and the 413 nm laser beam is referred to as the coupling beam. Only dipole allowed transitions are considered in the treatment presented here, hence $|\mathrm{r}\rangle$ does not couple to $|\mathrm{g}\rangle$. The lasers are narrow in frequency compared to the spacing between energy levels such that no other states are populated.

The electric field due to the laser beam, moving along z, is $\vec{E} = \vec{e}E_0 \cos(kz - \omega_\mathrm{L}t)$, with a polarization along $\vec{e}$, E_0 is the max electric field strength, k is the wavevector along z, and ω_L is the laser frequency. The Rabi frequency associated with the laser driving a transition between states $|i\rangle$ and $|j\rangle$ is

$$\Omega_{ij} = \frac{eE_0}{\hbar}\langle i|\hat{r}|j\rangle \ , \tag{2.6}$$

where $\langle i|\hat{r}|j\rangle$ is the position operator acting between states $|i\rangle$ and $|j\rangle$, and e is the elementary charge of the electron [60]. The Rabi frequency of the probe and coupling lasers are denoted as Ω_p and Ω_c respectively.

The three considered states can be written as $|\mathrm{g}\rangle = (1, 0, 0)^\mathrm{t}$, $|\mathrm{e}\rangle = (0, 1, 0)^\mathrm{t}$, $|\mathrm{r}\rangle = (0, 0, 1)^\mathrm{t}$. The Hamiltonian in this basis is then

$$\mathscr{H} = \hbar \begin{pmatrix} 0 & \frac{\Omega_\mathrm{p}}{2} & 0 \\ \frac{\Omega_\mathrm{p}}{2} & -\Delta_\mathrm{p} & \frac{\Omega_\mathrm{c}}{2} \\ 0 & \frac{\Omega_\mathrm{c}}{2} & -\Delta_\mathrm{p} - \Delta_\mathrm{c} \end{pmatrix} , \tag{2.7}$$

where we have transformed to a co-rotating frame of the laser field and

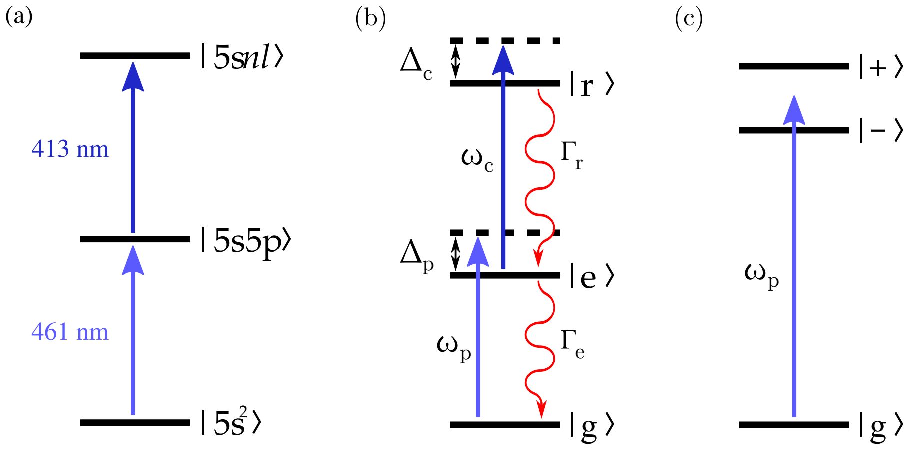

Figure 2.4: (a) The actual states and approximate wavelengths required for excitation in our experiment. (b) The driven three-level system corresponding to the optical Bloch equation modeling of our experiment. $|\mathrm{g}\rangle$ is the ground state, $|\mathrm{e}\rangle$ is the intermediate state, and $|\mathrm{r}\rangle$ is the Rydberg state. A laser field, ω_p, addresses the $|\mathrm{g}\rangle \rightarrow |\mathrm{e}\rangle$ transition, and is detuned from resonance, ω_eg, by $\Delta_\mathrm{p} = \omega_\mathrm{p} - \omega_\mathrm{eg}$; this laser field is referred to as the probe laser. The spontaneous decay rate from $|\mathrm{e}\rangle$ is $\Gamma_\mathrm{e} = 1/\tau_\mathrm{e}$, where τ_e is the lifetime of the intermediate state. A second laser field, ω_c, addresses the $|\mathrm{e}\rangle \rightarrow |\mathrm{r}\rangle$ transition, and is detuned from resonance, ω_er, by $\Delta_\mathrm{c} = \omega_\mathrm{c} - \omega_\mathrm{er}$; this laser field is referred to as the coupling laser. The spontaneous decay rate from $|\mathrm{r}\rangle$ to $|\mathrm{e}\rangle$ is Γ_r. (c) The dressed state picture of the three-level system.

the rotating wave approximation has been used to remove terms varying faster than the driving laser frequency, as they average to zero [61]. The Hamiltonian describes the driving between states due to the laser fields, i.e. no decay or decoherence is incorporated. To include the effect of spontaneous emission and other decoherence mechanisms the density matrix formalism is used [62]. The density matrix of the system is

$$\rho = \begin{pmatrix} \rho_\mathrm{gg} & \rho_\mathrm{ge} & \rho_\mathrm{gr} \\ \rho_\mathrm{eg} & \rho_\mathrm{ee} & \rho_\mathrm{er} \\ \rho_\mathrm{rg} & \rho_\mathrm{re} & \rho_\mathrm{rr} \end{pmatrix}, \tag{2.8}$$

where the on-diagonal terms, ρ_{ii}, describe the population in state i, and the off-diagonal terms, ρ_{ij}, describe the coherences between states i and j. Note that $\rho_{ij} = \rho^*_{ji}$. The time-dependent dynamics of the system can then be worked out by applying the Lindblad master equation [63]

$$\dot{\rho} = \frac{i}{\hbar}[\rho, \mathscr{H}] - \mathscr{L}(\rho) \;, \tag{2.9}$$

where $\mathscr{L}$ is the Lindblad super-operator for spontaneous emission in this system, given by

$$\mathscr{L}(\rho) = \begin{pmatrix} -\Gamma_{\mathrm{e}}\rho_{\mathrm{ee}} & \frac{1}{2}\Gamma_{\mathrm{e}}\rho_{\mathrm{ge}} & \frac{1}{2}\Gamma_{\mathrm{rg}}\rho_{\mathrm{gr}} \\ \frac{1}{2}\Gamma_{\mathrm{e}}\rho_{\mathrm{eg}} & \Gamma_{\mathrm{e}}\rho_{\mathrm{ee}} - \Gamma_{\mathrm{r}}\rho_{\mathrm{rr}} & \frac{1}{2}(\Gamma_{\mathrm{e}} + \Gamma_{\mathrm{r}})\rho_{\mathrm{er}} \\ \frac{1}{2}\Gamma_{\mathrm{rg}}\rho_{\mathrm{rg}} & \frac{1}{2}(\Gamma_{\mathrm{e}} + \Gamma_{\mathrm{r}})\rho_{\mathrm{re}} & \Gamma_{\mathrm{r}}\rho_{\mathrm{rr}} \end{pmatrix} \;. \tag{2.10}$$

Again, the on-diagonal terms redistribute population and the off-diagonal terms affect the coherence of the system. The terms in $\mathscr{L}_{31/13}$ are the effect on the coherence between the ground and Rydberg states due to spontaneous decay from the Rydberg state to the ground state, Γ_{rg}, which is zero as they are not dipole coupled. The above Lindblad super-operator is correct if there are no other sources of decoherence in the system. However, the lasers used to excite the transitions have a finite linewidth and therefore the effect of this has to be included in the master equation [64]. The finite laser linewidth is modeled as a phenomenological Lindblad super-operator

$$\mathscr{L}_{\mathrm{d}}(\rho) = \begin{pmatrix} 0 & \gamma_{\mathrm{p}}\rho_{\mathrm{ge}} & (\gamma_{\mathrm{p}} + \gamma_{\mathrm{c}})\rho_{\mathrm{gr}} \\ \gamma_{\mathrm{p}}\rho_{\mathrm{eg}} & 0 & \gamma_{\mathrm{c}}\rho_{\mathrm{er}} \\ (\gamma_{\mathrm{p}} + \gamma_{\mathrm{c}})\rho_{\mathrm{rg}} & \gamma_{\mathrm{c}}\rho_{\mathrm{re}} & 0 \end{pmatrix} \;, \tag{2.11}$$

where $\gamma_{\mathrm{p/c}}$ is the linewidth of the probe/coupling laser. The terms in $\mathscr{L}_{\mathrm{d}_{31/13}}$ are the two-photon linewidth, modeled as the arithmetic sum of the individual laser linewidths. However, as the coupling laser is locked to the probe laser, there may be some correlations in the noise distribution which would narrow this term. The effect of the laser linewidth is not to redistribute population but to increase the rate of decoherence in the system, hence there are no diagonal terms. The master equation is modified to include the phenomenological Lindblad term to become

$$\dot{\rho} = \frac{i}{\hbar}[\rho, \mathscr{H}] - \mathscr{L}(\rho) - \mathscr{L}_{\mathrm{d}}(\rho) \ . \tag{2.12}$$

2.2.1 Optical Bloch Equations

The coupled differential equations described by the master equation are known as the optical Bloch equations (OBE). The optical Bloch equations are a standard way of solving atomic state population dynamics, the formalism can be found in many references such as [61] or [64]. The Lindblad master equation, equation 2.12, is solved numerically using an ordinary differential equation solver in *MATLAB*. The decay paths are modeled as only going back to the state from which it was excited. However, in reality the Rydberg state could decay to a large range of $5sn\mathrm{p}\ ^1\mathrm{P}_1$ or $5sn\mathrm{f}\ ^1\mathrm{F}_3$ states. However, the factor of ω^3 in the radiative decay rate means that transitions to lower n states are favoured [65]. For the intermediate state the only dipole coupled state lower in energy, other than the ground state, is the 5s4d $^1\mathrm{D}_2$ state and the branching ratio is $\sim$ 1:50000 in favour of the ground state, hence this approximation should be valid. The optical Bloch equations are employed to model how spectra taken in our experiment respond to probe and coupling Rabi frequency, and detuning variations. Figures 2.5 and 2.6 were created using the *MATLAB* program.

The OBEs are solved as a function of time. In our experiment the relevant time scales are the excitation pulse length for a given set of parameters, and the intermediate state lifetime. The lifetime of the intermediate state in our experiment is 5 ns, meaning that for the 1 μs pulses used in the cold atom experiment the steady state is reached.

In the OBE simulation the Rydberg fraction is calculated at several probe frequencies to obtain spectra from which amplitude and spectral width information can be extracted. For the simulation, several parameters are required: the Rabi frequencies of the probe and coupling lasers, Ω_p and Ω_c; the linewidths of the intermediate and Rydberg states, Γ_e and Γ_r; the linewidths of the lasers, γ_p and γ_c; and the detuning of the coupling laser, Δ_c.

The probe Rabi frequency is calculated from the probe beam intensity, I, and the saturation intensity, I_sat, of the $5\mathrm{s}^2\ {}^1\mathrm{S}_0 \rightarrow 5\mathrm{s}5\mathrm{p}\ {}^1\mathrm{P}_1$ transition, $\Omega_\mathrm{p} = \Gamma_\mathrm{e}\sqrt{\frac{I}{2I_\mathrm{sat}}}$. The saturation intensity of this transition is 43 mW cm^{-2}. The coupling Rabi frequency is calculated from the coupling beam intensity and the oscillator strengths of the $5\mathrm{s}5\mathrm{p}\ {}^1\mathrm{P}_1 \rightarrow 5\mathrm{s}nl$ transition [66]. The oscillator strengths are taken from [67]. The linewidth of the $5\mathrm{s}^2\ {}^1\mathrm{S}_0 \rightarrow 5\mathrm{s}5\mathrm{p}\ {}^1\mathrm{P}_1$ transition is $2\pi \times 32$ MHz [68]. The linewidth of the $5\mathrm{s}5\mathrm{p}\ {}^1\mathrm{P}_1 \rightarrow 5\mathrm{s}nl$ transitions are extracted from the lifetime of the state [48] as $\Gamma_\mathrm{r} = 1/\tau_\mathrm{r}$. As we have no independent method of measuring the linewidth of the probe and coupling lasers these parameters are allowed to vary to best fit our data. The detuning of the coupling laser is also allowed to vary to take into account the effect of the stray magnetic/electric fields on the resonance and variations in laser lock point caused by changes in atomic flux in the locking cell and coupling laser power available for locking.

The OBE model described here will be used to simulate the Rydberg population which is measured experimentally in the cold atom setup, chapter 4.

2.2.2 Dressed state picture

The above treatment is useful for calculating the dynamics of the system, however, it is more instructive if the three-level system is considered in a dressed state picture [61], figure 2.4c. In the dressed state basis the intermediate state and Rydberg state are coupled together with the coupling laser.

If the two-photon resonance condition is fulfilled, $\Delta_\mathrm{p} + \Delta_\mathrm{c} = 0$, then the Hamiltonian in equation 2.7 can be diagonalized to give new eigenstates of

$$\begin{aligned}
|+\rangle &= \sin\theta\sin\phi|\mathrm{g}\rangle + \cos\phi|\mathrm{e}\rangle + \cos\theta\sin\phi|\mathrm{r}\rangle \ , \\
|0\rangle &= \cos\theta|\mathrm{g}\rangle - \sin\theta|\mathrm{r}\rangle \ , \\
|-\rangle &= \sin\theta\cos\phi|\mathrm{g}\rangle - \sin\phi|\mathrm{e}\rangle + \cos\theta\cos\phi|\mathrm{r}\rangle \ ,
\end{aligned} \tag{2.13}$$

where θ and ϕ are the Stückelberg mixing angles, given by

$$\tan\theta = \frac{\Omega_\mathrm{p}}{\Omega_\mathrm{c}} \ , \tag{2.14}$$

and

$$\tan 2\phi = \frac{\sqrt{\Omega_\mathrm{p}^2 + \Omega_\mathrm{c}^2}}{\Delta_\mathrm{p}} \ . \tag{2.15}$$

A "dark state", $|0\rangle$, is formed as it does not couple to the intermediate state, and can therefore absorb no photons from the driving laser fields. Population falls into the dark state at a rate comparable to the intermediate state lifetime, due to spontaneous emission from the intermediate state, where it becomes trapped.

Next the optical response of the probe laser and the Rydberg state population will be looked at in more detail by studying the solutions to the OBE. The optical response is important as it is used to lock our coupling laser, section 3.4.2.

The density matrix encodes information on the population in each state via the diagonal terms. The off-diagonal elements of the density matrix yield information on the optical response of the laser fields. The transmission of the probe beam is related to the complex susceptibility, $T = I/I_0 = \exp(-kl\chi_\mathrm{I})$, where k is the wavevector, and l is the length of the medium [69], and the susceptibility is proportional to the ρ_{ge} term in the density matrix, $\chi \propto \rho_{\mathrm{ge}}$ [70].

2.2.3 Electromagnetically induced transparency

Electromagnetically induced transparency (EIT) is a process whereby the the probe transition becomes transparent due to the coupling to another state [71]. In our system the coupled state is a Rydberg state. EIT requires phase coherent lasers addressing both transitions and can result in features narrower than the intermediate state linewidth, down to the linewidth of the Rydberg state [70].

The transparency arises in the weak probe regime where $\Omega_{\mathrm{p}} \ll (\Omega_{\mathrm{c}},\ \Gamma_{\mathrm{e}})$, hence, $\sin\theta \rightarrow 0$ and $\cos\theta \rightarrow 1$ in equation 2.13. The eigenstates of the system therefore simplify to

$$
\begin{aligned}
|+\rangle &= +\cos\phi|\mathrm{e}\rangle + \sin\phi|\mathrm{r}\rangle \ , \\
|0\rangle &= |\mathrm{g}\rangle \ , \\
|-\rangle &= -\sin\phi|\mathrm{e}\rangle + \cos\phi|\mathrm{r}\rangle \ .
\end{aligned}
\tag{2.16}
$$

The dark state is now only the ground state, hence population becomes trapped there and no other states are excited. With the probe laser on resonance, i.e. $\Delta_{\mathrm{p}} = 0$, the upper states become $|\pm\rangle = \frac{1}{\sqrt{2}}(\pm|\mathrm{e}\rangle + |\mathrm{r}\rangle)$. As the intermediate state is now coupled with probabilities of equal and opposite magnitude, Fano type interference of the excitation pathways [72] mean the intermediate state cannot be addressed and the probe laser is not absorbed. The width of the transmission feature is dependent upon the Rabi frequency of the coupling laser, the linewidth of the $|\mathrm{e}\rangle \rightarrow |\mathrm{r}\rangle$ transition, and the laser linewidths.

Figure 2.5 shows the effect on the probe spectrum of different coupling Rabi

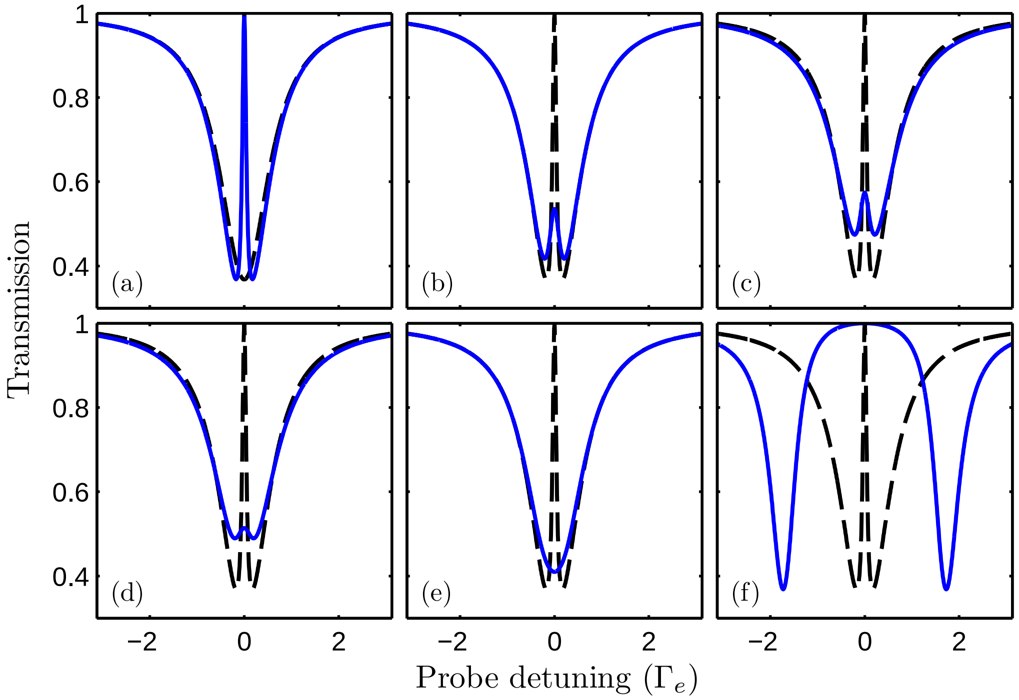

Figure 2.5: Theoretical EIT spectra. The probe transmission with $\Omega_{\mathrm{p}} = 0.02\Gamma_{\mathrm{e}}$ for all spectra is shown. The black, dashed line in (a) is with $\Omega_{\mathrm{c}} = 0$ and the blue, solid line is with $\Omega_{\mathrm{c}} = 0.34\Gamma_{\mathrm{e}}$. The dephasing rates γ_{p} and γ_{c} are both zero. The black, dashed lines of (b) - (f) are the same as the blue, solid line from (a). The blue, solid lines of (b) - (e) all have $\Omega_{\mathrm{c}} = 0.34\Gamma_{\mathrm{e}}$ and the laser linewidths are varied. (b) having $\gamma_{\mathrm{p}} = 0$ with $\gamma_{\mathrm{c}} = 0.1\Gamma_{\mathrm{e}}$. (c) shows $\gamma_{\mathrm{p}} = 0.1\Gamma_{\mathrm{e}}$ with $\gamma_{\mathrm{c}} = 0$. (d) shows $\gamma_{\mathrm{p}} = 0.1\Gamma_{\mathrm{e}}$ and $\gamma_{\mathrm{c}} = 0.1\Gamma_{\mathrm{e}}$. (e) shows $\gamma_{\mathrm{p}} = 0$ with $\gamma_{\mathrm{c}} = 0.5\Gamma_{\mathrm{e}}$. (f) shows the Autler-Townes regime where $\Omega_{\mathrm{c}} = 3.4\Gamma_{\mathrm{e}}$ with zero dephasing.

frequencies and dephasing rates. The effect of including a coupling laser can be seen in (a) with a narrow resonance creating full transmission of the probe again. On resonance transmission reaches 100 % only when the linewidth of the laser involved is much narrower in frequency than the natural linewidth of the transition. Rydberg states have linewidths in the region of tens of kilo-Hertz making laser linewidths narrower than these transitions experimentally challenging. The reduction in transmission of the EIT feature is shown for differing laser linewidths and is due to mixing of the intermediate state. The coherence between the ground state and the Rydberg state is the relevent parameter that controls the fidelity of the EIT transmission. The ground-Rydberg state coherence is affected by the two-photon laser linewidths as discussed above, which is why the fidelity reduces in both (b) and (c). (d) shows a spectrum where both of the exciation lasers have broadened linewidths, similar to experimental conditions, and the EIT feature is quite small as a consequence. The linewidth of the coupling laser is very broad in (e) and the EIT is entirely washed out. With a much larger coupling laser Rabi frequency, (f), the EIT condition disappears and the Autler-Townes regime is reached [73]. Minimising the linewidth of the excitation lasers is clearly important to enable these spectroscopic techniques to be employed.

The Autler-Townes effect causes a splitting of a resonance in a three-level system due to the AC-Stark effect [73]. The oscillating electric field is caused by the laser field used to address the transition. An example of Autler-Townes splitting is shown in figure 2.5f where the coupling laser has a high Rabi frequency relative to the probe linewidth and probe Rabi frequency. The transparency in EIT arises due to interference of the excitation pathways. Whereas, the transparency in Autler-Townes splitting is caused by the $|+\rangle$ and $|-\rangle$ states being split apart by further than the intermediate state linewidth, hence two Lorentzians are resolved.

Differentiating where EIT becomes Autler-Townes splitting is not straight forward as there is a smooth progression from one to the other with a crossover region where both occur. Several papers give criteria of how to distinguish between them [74, 75].

2.2.4 Coherent population trapping

A related phenomenon to EIT is that of coherent population trapping (CPT) [76, 77]. In CPT the probe Rabi frequency is no longer vanishingly weak, so the eigenstates are described by equation 2.13. The dark state is a superposition state of $|\mathrm{g}\rangle$ and $|\mathrm{r}\rangle$, hence there is population in the Rydberg state and none in the intermediate state. CPT is fundamentally different from incoherent excitation of Rydberg states, which would populate the intermediate state and lead to features as broad as the intermediate state linewidth.

In the cold atom experiments we measure a signal proportional to the population in ρ_{rr}, hence the evolution of the CPT spectrum is important for us to simulate.

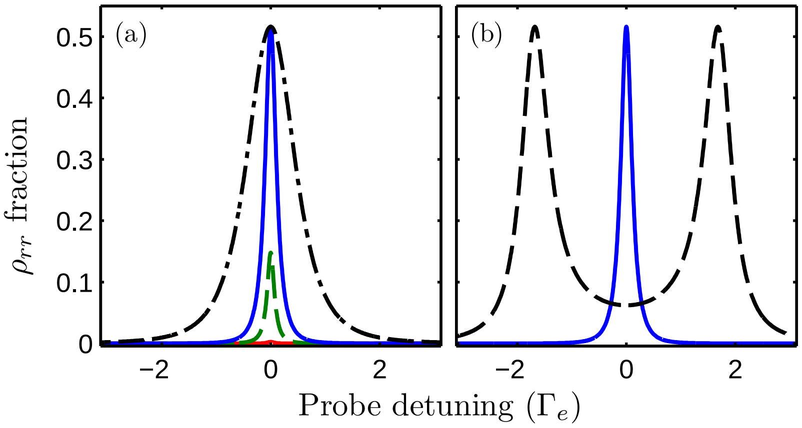

Figure 2.6: The fraction of population in the Rydberg state, ρ_{rr}, as a function of probe detuning. (a) The red, solid line has $\Omega_{\mathrm{p}} = 0.02\Gamma_{\mathrm{e}}$, the green, dashed line has $\Omega_{\mathrm{p}} = 0.14\Gamma_{\mathrm{e}}$, and the blue, solid line has $\Omega_{\mathrm{p}} = 0.34\Gamma_{\mathrm{e}}$. The black, dashed line in (a) shows the Rydberg population if the state is incoherently populated, scaled to the same amplitude as the blue, solid line. $\Omega_{\mathrm{c}} = 0.34\Gamma_{\mathrm{e}}$, and $\gamma_{\mathrm{p}} = \gamma_{\mathrm{c}} = 0$ for all spectra. (b) The blue, solid line is the same as in (a) with the black, dashed line $\Omega_{\mathrm{p}} = 3.4\Gamma_{\mathrm{e}}$, showing Autler-Townes splitting of the CPT spectrum, scaled to the same amplitude as the blue, solid line. The dephasing rates γ_{p} and γ_{c} are both zero for all simulations.

Figure 2.6 shows the population in the Rydberg state, ρ_{rr} as a function of coupling laser power. The weak probe regime, the red, solid line in (a), corresponding to the same parameters used in figure 2.5a to create a narrow EIT resonance, only negligibly populates the Rydberg state as expected. Higher probe Rabi frequency, depicted as the green, dashed and blue, solid lines, increase the population in the Rydberg state as expected. The effect of finite laser linewidth is to reduce the population in the Rydberg state. The linewidth of the CPT spectrum and the total population transferred to the Rydberg state is set by the Rabi frequencies of the probe and coupling lasers, the linewidth of the $|\mathrm{e}\rangle \rightarrow |\mathrm{r}\rangle$ transition, and the laser linewidths. If the Rydberg state is populated via an incoherent mechanism then the CPT spectrum cannot be narrower than the intermediate state linewidth, displayed as the black, dot-dashed line in (a). Autler-Townes splitting is also present in the Rydberg population, as shown in (b).

A similar process to CPT is that of stimulated Raman adiabatic passage (STIRAP) [78]. In STIRAP a non-intuitive pulse sequence is used where the coupling laser is turned on before the probe laser. The main differences to CPT are that STIRAP is done quite far from an atomic resonance to avoid populating the intermediate state, as a result the process takes quite a long time ($\sim$ ms) and is therefore normally done in a Λ three-level system, to avoid spontaneous decay. STIRAP can transfer 90 % of the population [79]. Although STIRAP has a better transfer efficiency than CPT the time scales involved are much slower than the Rydberg dynamics we wish to study and hence is not used.

Conclusion

Rydberg atoms have strong, tunable, long-range van der Waals interactions. The strength of these interactions in strontium have been calculated using a single electron model. Analysis of the angular effects shows that the $5sns\ ^1\mathrm{S}_0$ states have spatially isotropic, attractive interactions whereas the $5snd\ ^1\mathrm{D}_2$ states have a Förster zero state which reduce the interaction strength. If the blockade regime is to be reached then knowledge of the interaction strengths and signs is crucial. The sign of interaction of these two states are different allowing different physical processes to be investigated [32].

A two-photon, three-level excitation scheme to Rydberg states is used later in the experimental results section of this thesis. To understand the intricacies of coherent excitation in the three-level system, a dressed state picture is presented with the origin of EIT, CPT and Autler-Townes splitting described. An optical Bloch equation model is implemented to simulate the Rydberg population dynamics, with particular regard to the Rydberg fraction as this is the measured quantity in the cold atoms.

Chapter 3

Laser frequency stabilization

In a cold atom experiment there needs to be laser light at specific detunings from resonance to cool, trap, and excite the atoms. Lasers naturally drift in frequency due to temperature fluctuations, in our lab rates of ≈ 1 GHz per hour are normal. Consequently the laser frequency had to be stabilized, commonly referred to as “laser locking”. Three common ways to stabilize laser frequency are: using atomic vapour spectroscopy [80]; using a reference cavity [81]; or using a hollow cathode lamp [82]. Hollow cathode lamps are quite expensive and will therefore not be used. Reference cavity locking requires a high-finesse cavity that does not drift in frequency; due to the difficulties and expense inherent with building such a cavity we decided to use atomic vapour spectroscopy locking.

The generation of a thermal vapour of strontium is not a trivial exercise and the complications of working with strontium compared to alkali elements will be detailed.

To frequency stabilize a laser a dispersive feature is required to give the correct feedback to the laser. For a closed $J = 0 \rightarrow J = 1$ transition, like the $5\mathrm{s}^2\ {}^1\mathrm{S}_0 \rightarrow 5\mathrm{s}5\mathrm{p}\ {}^1\mathrm{P}_1$ transition used for cooling and trapping of strontium, there are many spectroscopic methods available for creating these dispersive features. Four of these methods will be discussed in this chapter.

To do CPT in the cold atoms a coupling laser, which is phase stable with the probe laser, is required. A recently conceived method of stabilizing the coupling laser using EIT [83] was implemented and will be discussed.

This chapter will:

- detail the vapour cell needed for strontium spectroscopy in section 3.1
- describe modulation-free spectroscopy in section 3.2
- describe frequency modulation spectroscopy in section 3.3
- describe electromagnetically induced transparency for laser locking in section 3.4

3.1 Vapour cell

To do atomic spectroscopy a source of atomic vapour is required. For some of the alkali metals (rubidium, caesium, and potassium) an atomic vapour is easily made in small, evacuated glass cells with a reservoir of the metal. The vapour pressure at room temperature is sufficient for spectroscopy. In strontium, however, the vapour pressure at room temperature is negligible [84, 85]. A further problem is that strontium metal reacts with glass [86]. To obtain an atomic vapour of strontium for spectroscopy different methods have been employed: heat pipes with buffer gases to protect the viewports [87, 88]; or evacuated cells with heated sapphire viewports which don't react with strontium [86, 89].

For atomic vapour spectroscopy on our experiment a new vapour cell was developed by L. Bridge [90]. A dispenser (*Alvatec AS-Sr-500-F*) holding 500 mg of strontium is held inside a small vacuum chamber. The cell is evacuated to $\sim 10^{-8}$ torr but is not actively pumped during operation as strontium acts as a getter for water and oxygen. The dispenser is resistively heated by passing current (~ 15 A) through it via electrical feedthroughs. The temperature the dispenser reaches has not been measured, though as absorption is seen, the temperature must be around 900 K. The heated dispenser creates a weakly collimated jet of strontium vapour. The optical access for spectroscopy is orthogonal to the atomic jet. The viewports are held 14 cm from the atomic jet to prevent strontium deposition. The viewports are not heated but after four years of use no strontium can be seen on the viewports. No buffer gas is present in the cell to remove collisional broadening from the spectroscopy seen [87]. The dispenser operates for approximately 10,000 hours at a stable absorption of ≈ 30 % on the singlet $5s^2\ ^1S_0 \rightarrow 5s5p\ ^1P_1$ transition before emptying and needing to be changed.[1]

3.1.1 The $5s^2\,^1S_0 \rightarrow 5s5p\,^1P_1$ transition

In a vapour cell the velocity profile of the atoms means the Doppler effect generally broadens the observed spectral feature to be greater than the transition being probed. To resolve sub-Doppler features saturated absorption spectroscopy is used. Figure 3.1a shows a saturated absorption spectroscopy setup. An intense beam, referred to as the "pump" beam, is overlapped counter-propagating with a weak probe beam. The probe is detected on a photodiode. Sub-Doppler features are resolved due to spectral hole burning [80]. An example saturated absorption spectroscopy signal is shown in figure 3.1b. The laser used to interrogate the atoms is a frequency doubled diode laser (*Toptica TA-SHG 110*) operating at 461 nm. By taking the difference of a Doppler and sub-Doppler absorption profile the transmission can be calculated. All of the laser locking techniques described below use pump-probe setups to generate sub-Doppler locking signals. The challenge is to create

---

[1] A second cell with two dispensers facing each other reached ≈ 100 % absorption though the isolation of the viewports from the atomic vapour was insufficient and over the course of several months a layer of strontium built up on the viewports impeding use.

a dispersive lineshape which has a zero crossing and sharp gradient at the resonance value ideal for locking.

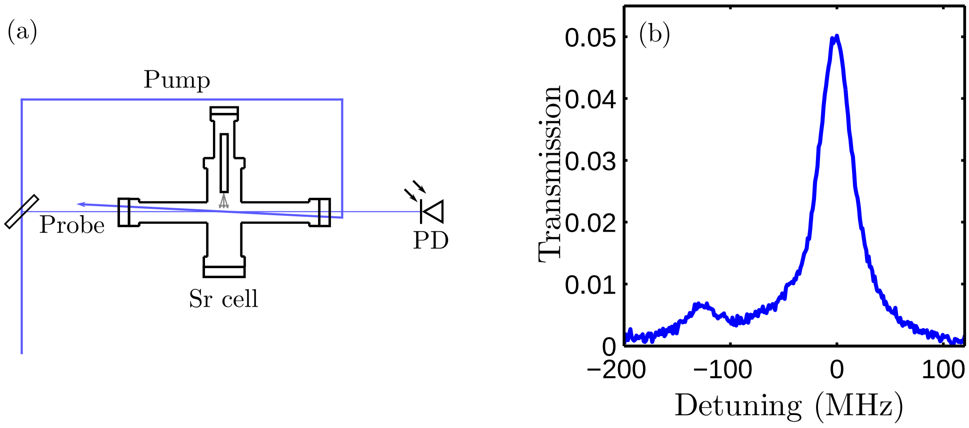

Figure 3.1: (a) Optical layout for saturated absorption spectroscopy. The weak probe beam is split off from the strong pump beam via a glass plate and is detected on a photodiode (PD). (b) Example saturated absorption spectroscopy signal in the thermal cell. The peak centred at zero detuning is the 83 % abundant ^{88}Sr isotope. The smaller peak on the negative detuning side is the 10 % abundant ^{86}Sr isotope. The splitting between these two isotopes is 124.5 MHz [91].

To stabilize a laser to a frequency a reference signal which changes sign across resonance, is required. This anti-symmetry is necessary because a feedback signal to correct the laser frequency needs to have a different sign on either side of resonance.

The key parameters for an error signal are the amplitude of the signal, the gradient of the locking slope and the capture range of the lock. The capture range of the lock is the extent in frequency over which the feature has the correct sign to return the laser to the zero crossing. The gradient is the limit as to how tightly the laser can be locked to resonance.

An analogue electronic circuit is used to feed back to the laser's diffraction grating piezoelectric stack to correct the frequency and is shown in figure A.6.

Four methods of generating these dispersive signals are described in this chapter in two different general setups; modulation-free and frequency modulation spectroscopy.

Initially modulation-free spectroscopies were used for creating locking signals for cold Rydberg experiments due to simplicity and expense. A paper detailing the performance of these modulation-free techniques was published [92].

The desire for more accurate control of the stability and offsets of the lock lead to using frequency modulation spectroscopies.

3.2 Modulation-free spectroscopy

Dispersive lineshapes can be generated by carefully controlling the polarization of the light used to excite the atoms' magnetic sub-levels. The polarization of the light detected is also crucial. As these techniques do not require modulation of the pump or probe beams they are therefore described as modulation-free types of spectroscopy. Two such techniques will be described in this section, polarization spectroscopy [93] and sub-Doppler dichroic atomic vapour laser locking (SDDAVLL) [94]. The advantage of modulation-free spectroscopy is the lack of need for an expensive phase modulator or the residual amplitude modulation caused by laser drive current modulation.

3.2.1 Polarization spectroscopy

Polarization spectroscopy creates a dispersive feature by a difference in absorption of the orthogonal circular polarization components of light across the resonance (i.e. birefringence) [95]. The measured signal is the difference between the amount of vertically and horizontally polarized light, analyzed using a polarizing beam splitter. The differenced signal can be shown to be [95]

$$I_{\text{signal}} = I_0 e^{-\alpha L} \cos(2\phi + 2\Phi) \;, \tag{3.1}$$

where I_0 is the input intensity, α is the total absorption coefficient on resonance, L is the length of the medium, ϕ is the polarization angle of the initial linear beam (set to $\pi/4$ so that, when off resonance, the signal is zero), and the absorption induced rotation Φ is

$$\Phi = L \frac{\Delta\alpha_0}{2} \frac{x}{1+x^2} \;, \tag{3.2}$$

where $\Delta\alpha_0$ is the on resonance difference in absorption between the two circularly polarized components, and $x = 2(\omega - \omega_0)/\Gamma'$, where ω is the laser frequency, ω_0 is the resonance frequency of the transition, and Γ' is the power broadened linewidth of the transition. With only a probe beam no dispersion signal is generated, as there is no difference in absorption across resonance, therefore a circularly polarized pump beam is required.

In the alkali metals the birefringence is caused by the pump beam optically pumping the ground state population to a state of maximum $|m_{\text{J}}|$, and the difference in Clebsch-Gordan coefficients between the left and right circularly polarized transitions [93, 96].

In elements with unique ground states, such as the bosonic alkaline-earth elements, the birefringence arises from a different mechanism. The level setup for the transition being probed is shown in figure 3.2a. The pump beam saturates the $\sigma^{+(-)}$ transition meaning the two circular components of the probe beam are absorbed differently.

The optical layout is shown in figure 3.2b. A glass plate is used to split off some laser light for saturated absorption spectroscopy for frequency stability tests. A polarizing beam splitter cube (PBS) is used to set the polarization to be horizontally linear. Another glass plate is used to split light off for the probe beam. The pump beam is circularly polarized using a $\lambda/4$ waveplate. The pump and probe beams are then overlapped, counter-propagating in the cell with a small angle between them (~ 20 mrad). The probe beam is analyzed using another PBS and the two linear polarization components detected on a differencing photodiode (DPD). The $\lambda/2$ waveplate before the analyzing PBS is set so that the polarization is at $\pi/4$ to the axis of the cube such that off resonance half the light exits each port of the cube. The $\lambda/2$ waveplate is rotated slightly to remove any birefringence caused by the cell windows.

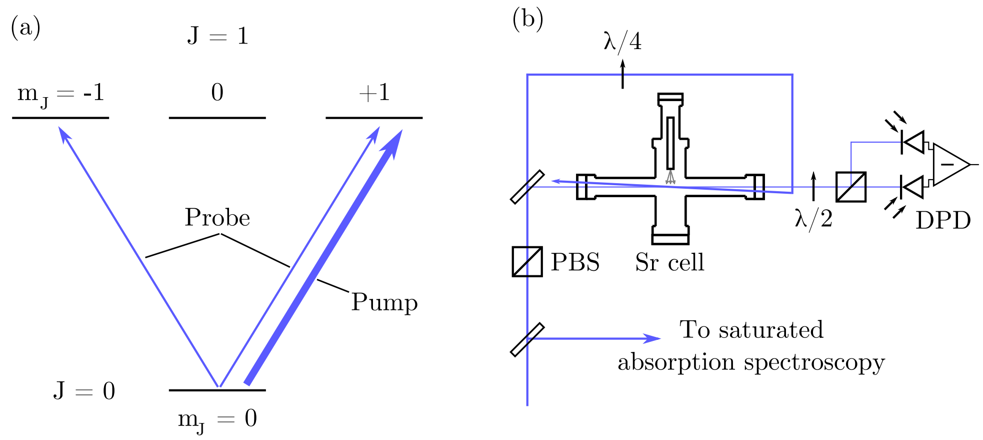

Figure 3.2: (a) The level diagram for the $5s^2\ ^1S_0 \rightarrow 5s5p\ ^1P_1$ transition. The probe is a linear combination of both circular polarizations of light, and the pump is set to one or the other, in this setup it is set to drive the σ^+ transition. (b) Optical layout for polarization spectroscopy.

An example polarization spectroscopy signal is shown in figure 3.3. A clear dispersion shape is seen with no Doppler background, ideal for locking for the ^{88}Sr isotope. The smaller feature to the left of the main feature is the ^{86}Sr isotope. The polarization spectroscopy signal should be anti-symmetric, but clearly is not. The magnitude of the amplitude of the signal to the positive detuning side of resonance is larger than the negative detuning side. The reason for the asymmetry is that the fermionic ^{87}Sr isotope resonances lie close to the ^{88}Sr resonance and to the negative detuning side and hence interfere with the dispersion signal.

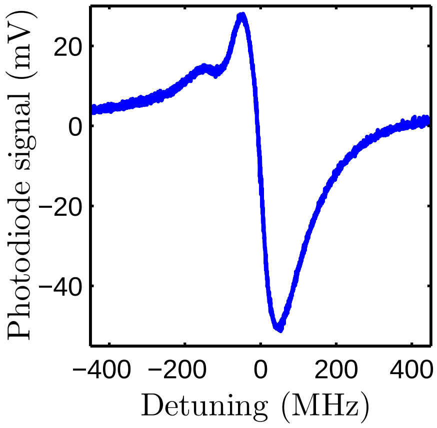

Figure 3.3: Example polarization spectroscopy error signal in the thermal cell taken with a pump beam intensity of 0.93 W cm^{-1}.

The error signal was compared with a concomitantly acquired saturated absorption spectroscopy signal in the second generation cell to check the detuning of the zero crossing from the resonance line centre. The detuning was 10 MHz, a value which is useful to know for setting the detunings of the cooling and trapping light used in chapter 4. The zero crossing can be changed via an electronic offset in the locking circuit or a small rotation of the $\lambda/2$ waveplate. The stability of the zero crossing was also investigated by using the saturated absorption spectroscopy signal. The RMS variation was 0.8 MHz over an hour. The performance of the lock is described in detail in [92].

The amplitude, figure 3.4a, and gradient between 25 % and 75 % of the amplitude, figure 3.4b, of the polarization spectroscopy error signal as a function of pump intensity were investigated. The data points are the mean of five successive shots and the error bars are the standard deviation. For the gradient data a 1.7 % statistical error on the frequency measurement is also incorporated in the error bar. The amplitude follows a saturation trend. The saturation intensity for the singlet 5s^2 ^{1}S$_0$ $\rightarrow$ 5s5p ^{1}P$_1$ transition being addressed here is 43 mW cm^{-2}, agreeing with the data. The gradient increases as the amplitude increases and then starts decreasing at higher intensities due to power broadening of the transition increasing the width.

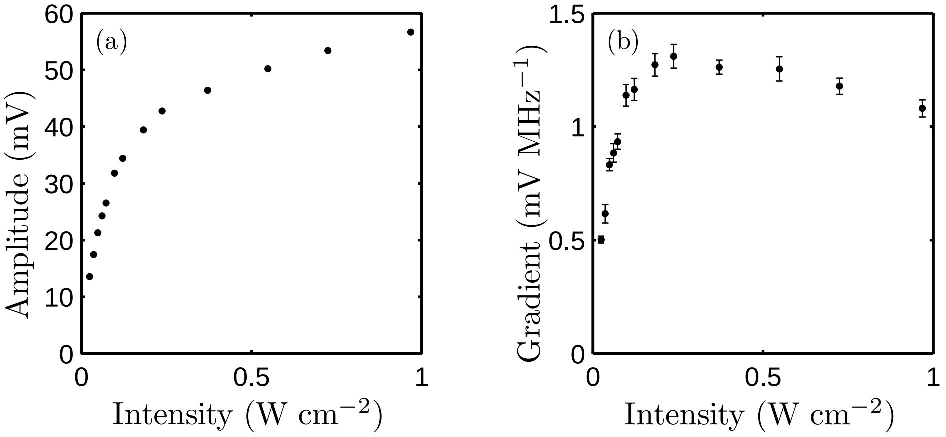

Figure 3.4: Variation of the (a) amplitude of the polarization spectroscopy error signal and (b) gradient of the error signal with pump beam intensity. The probe beam power is kept fixed at 41 μW

3.2.2 Sub-Doppler dichroic atomic vapour laser locking

The Zeeman effect can be used to create dispersive signals, in a process called dichroic atomic vapour laser locking (DAVLL) [97, 98]. A magnetic field is applied along the laser beams, and the Zeeman effect splits the magnetic sub-levels by $m_{\mathrm{J}}\mu_{\mathrm{B}}B$, [99], as shown in figure 3.5a. On opposite detunings of the zero field resonance the two circular polarization components are therefore absorbed differently when a magnetic field is applied and the dispersive lineshape arises due to this.

The beam layout is shown in figure 3.5b. A pair of coils is attached to the vapour cell to apply an uniform magnetic field. The probe beam is linearly polarized and, as with polarization spectroscopy, analyzed by a PBS onto a differential photodiode. A $\lambda/4$ is used before the PBS in DAVLL, unlike

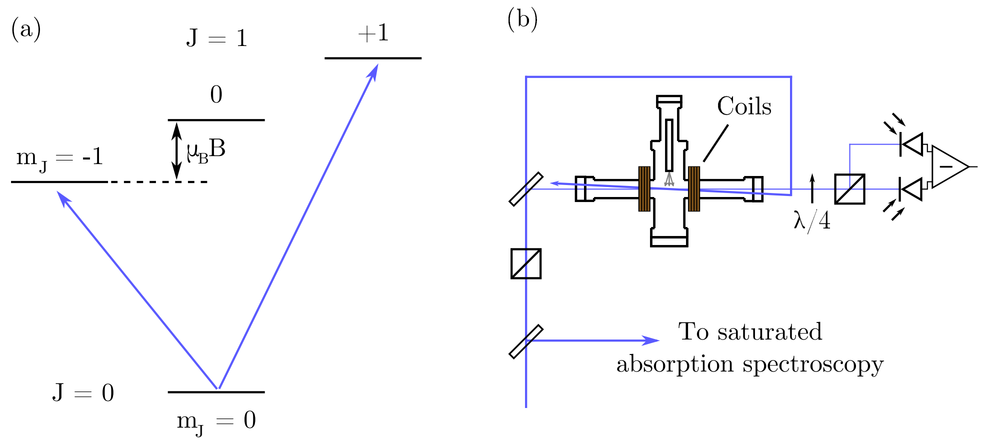

Figure 3.5: (a) The level diagram for the 5s^2 $^1S_0$ → 5s5p $^1P_1$ transition with a magnetic field applied. (b) Optical layout for SDDAVLL spectroscopy.

polarization spectroscopy, so that the output from the two ports of the PBS are now the two circular polarization components.

By including a counter-propagating, linearly polarized pump beam, DAVLL can resolve sub-Doppler features [94], and is hence called sub-Doppler dichroic atomic vapour laser locking (SDDAVLL).

Example traces of both DAVLL and SDDAVLL are shown in figure 3.6. The sub-Doppler signal has a much steeper error signal compared to the probe only DAVLL, as expected, but sits on a Doppler background signal.

The dependence of the amplitude and 25 %-75 % gradient of the ^{88}Sr isotope sub-Doppler DAVLL feature as a function of pump beam intensity (figures 3.7a and 3.7c) and magnetic field (figures 3.7b and 3.7d) were investigated.

The amplitude and gradient trends as a function of pump beam intensity are similar to the trends for polarization spectroscopy. The amplitude saturates at a pump intensity of 0.4 W cm^{-2}. The gradient increases sharply with intensity, reaching a maximum again at a pump intensity of about 0.4 W cm^{-2} before trending downward at higher intensities when power broadening becomes comparable to the Zeeman splitting. Both the amplitude and magnitude of the gradient as a function of applied magnetic field increase at

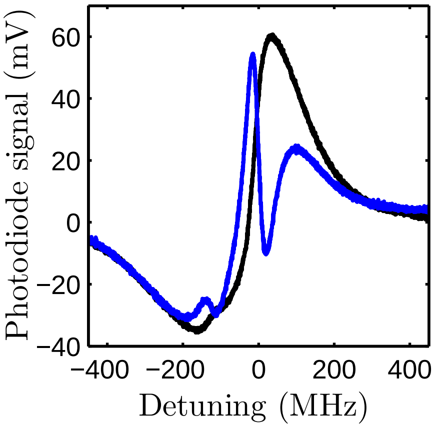

Figure 3.6: Example DAVLL spectroscopy error signal in the thermal cell. The black line is probe only DAVLL and the blue line is pump-probe sub-Doppler DAVLL.

low field before turning over and decreasing at higher fields. The decrease at higher fields is due to the Zeeman splitting being larger than the power broadened linewidth of the transition. The magnetic field of the coils was measured using a Gauss meter before attaching the coils to the cell. The gradient changes sign when the magnetic field direction is switched because the polarization is defined by the angle between the k-vector of the laser beam and the magnetic field, i.e. σ^+ becomes σ^- and vice versa. The optimum magnetic field is when the Zeeman splitting between the two stretched states is equal to the power broadened linewidth. The optimum is at 12 G, corresponding to a splitting of 34 MHz, indicating a small power broadening from the natural linewidth of 32 MHz.

The zero crossing of the lock relative to the line centre and locking stability were measured by comparison to saturated absorption spectroscopy. The zero crossing offset was found to vary with magnetic field due to the Doppler background between 10 and 30 MHz. The locking circuit allows a voltage offset to be added to the error signal to overcome the issue of frequency offset. The RMS stability was found to be 3 MHz over an hour period. Compared to the polarization spectroscopy signal stability the sub-Doppler DAVLL signal

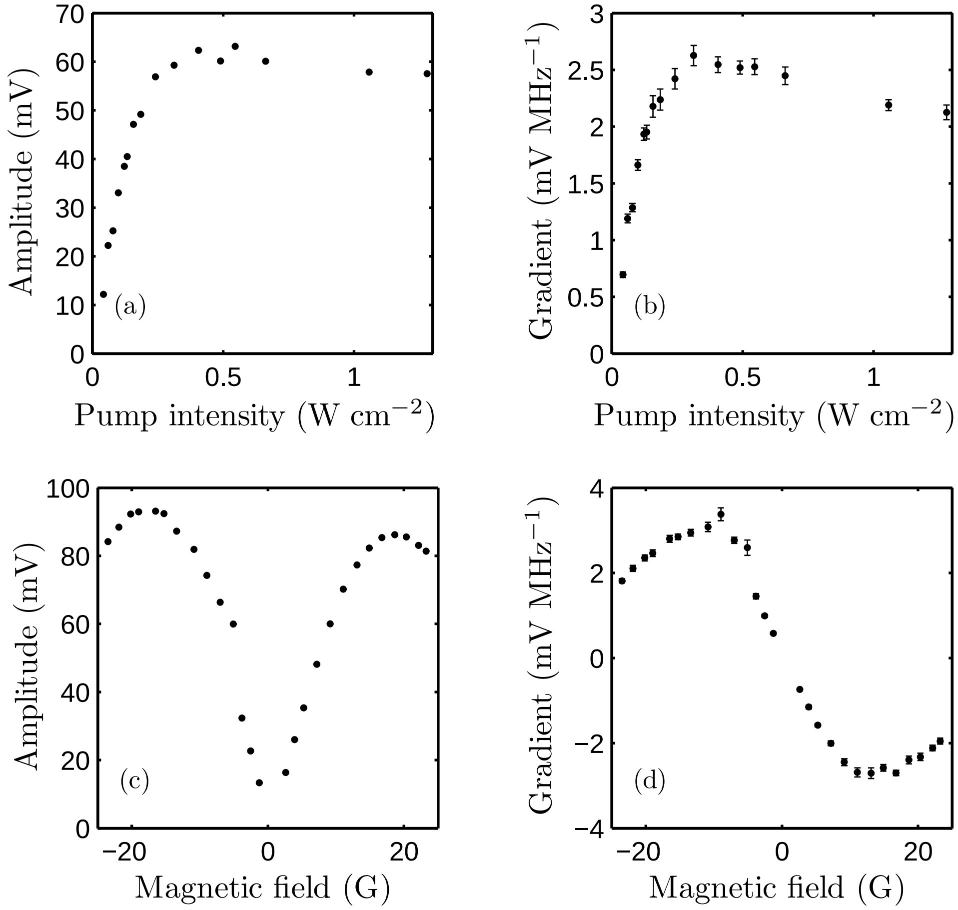

Figure 3.7: Variation of the amplitude (a) and gradient (b) of the sub-Doppler DAVLL signal as a function of pump beam intensity, with the magnetic field fixed at 9.5 G. Variation of the amplitude (c) and gradient (d) of the sub-Doppler DAVLL signal as a function of applied magnetic field. The pump intensity was fixed at 0.66 W cm^{-2}.

is worse, probably due to the Doppler background present in the sub-Doppler DAVLL signal.

Conclusion

Polarization spectroscopy and sub-Doppler DAVLL both create sharp dispersion features suitable for laser locking, without the need for modulation of the laser beam. The stability of the polarization spectroscopy signal is better than the sub-Doppler DAVLL signal and was used to lock the laser for several experiments on cold atom Rydberg spectroscopy [46–48].

3.3 Modulation spectroscopy

The previous section described the generation of error signals using simple spectroscopic techniques. Phase modulation of the laser beam can directly lead to error signals, and is therefore referred to as modulation spectroscopy. The major advantage of modulation spectroscopy is that polarization control is less critical for generation of error signals. Thermal fluctuations in the lab cause changes in the polarization due to changes in waveplates and PBS cubes.

The two types of modulation spectroscopy described in this section are sub-Doppler frequency modulation spectroscopy (SDFM) [100] and modulation transfer spectroscopy (MT) [101]. Both these techniques rely on modulation of the phase of the laser beam which is done by using an electro-optic modulator, EOM (*Photonics Technologies EOM-01-10-U*), working at 9.5 MHz.

3.3.1 Sub-Doppler frequency modulation spectroscopy

In SDFM the probe beam is modulated which adds sidebands at the modulation frequency. The measured signal arises from a beat signal between the carrier and the sideband of the probe beam on a photodiode [81, 100]. The beat signal is at the modulation frequency of the sidebands. The optical and electronic layout is shown in figure 3.8a. An electronic mixer is used for down conversion of the signal to DC. Varying the phase of the local oscillator used to drive the EOM relative to the measured signal means either the in phase signal or the quadrature signal can be obtained.

There are two operating regimes depending on relative size of the modulation frequency and the natural linewidth of the transition being probed [102, 103]. With a modulation frequency lower than the half width half maximum (HWHM) of the feature being probed the in phase signal is proportional to the first derivative of the absorption and the quadrature signal is proportional to the second derivative of the absorption. With a modulation frequency much higher than the HWHM the in phase signal is proportional to the absorption, and the quadrature signal is proportional to the first derivative of the absorption. The first derivative signal gives rise to the dispersion lineshape necessary for locking. In our experiments the modulation frequency is 9.5 MHz and the HWHM is 16 MHz, hence we are in the low modulation frequency regime.

The beam layout for SDFM is shown in figure 3.8a. The probe beam goes through an EOM which adds sidebands to the laser beam at the driving frequency of the EOM. The 9.5 MHz driving frequency is from a tunable frequency generator (*TTi TG120*). Part of the driving frequency signal is diverted to a level 7 double balanced mixer (*Mini Circuits ZLW-1-1*) via a phase shifter (*Mini Circuits JSPHS-12 (+)*). The probe is detected on a home-built fast photodiode, see appendix A.3. The phase shifter is adjusted such that the in phase signal is acquired to obtain a dispersive feature. A dispersion signal can be obtained with only a probe beam, however this signal will be related to the Doppler profile of the thermal vapour. As with SDDAVLL, including a pump beam allows the sub-Doppler features to be resolved. The pump and probe beams are both horizontally polarized. The waveplate in the pump beam is to correct any polarization rotation caused by the optics. A 10 kHz low pass active filter reduces high frequency noise but also means the linewidth of the laser cannot be narrowed.

SDFM is analogous to Pound-Drever-Hall laser locking to a cavity [103]. The spectral feature used for locking is an atomic reference in SDFM and a cavity peak in PDH, otherwise the processes are physically the same.

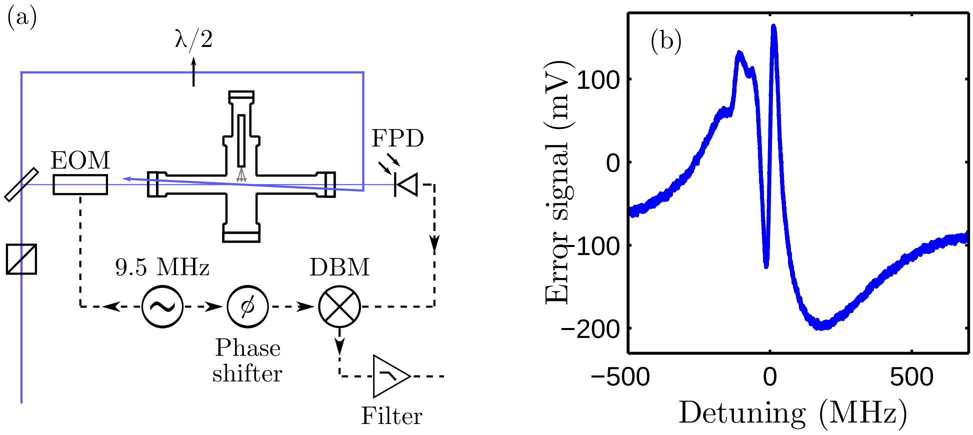

Figure 3.8: (a) SDFM optical (solid line) and electronic (dashed line) layout. (b) Example SDFM spectroscopy error signal in the thermal cell with a probe beam intensity of 3m W cm^{-2} and a pump beam intensity of 0.43 W cm^{-2}. The RF voltage for the EOM was set to 6 V.

An example SDFM signal is shown in figure 3.8b. The error signal is qualitatively similar to the SDDAVLL signal shown in figure 3.6, though inverted. A sharp dispersion signal caused by the ^{88}Sr isotope is superimposed on a Doppler broadened background. Smaller features due to the ^{86}Sr and ^{87}Sr isotopes are also visible.

The amplitude and 25 %-75 % gradient of the ^{88}Sr isotope dispersion signal as a function of probe intensity and pump intensity are shown in figure 3.9. The amplitude as a function of probe intensity, (a), shows a saturation type behaviour. The saturation intensity for this transition is 0.043 W cm^{-2}, which is roughly where half the maximum amplitude occurs as expected. The gradient as a function of probe beam intensity, (b), also shows a saturation type behaviour though not as pronounced.

The amplitude and gradient as a function of pump beam intensity, (c) and (d) respectively, both show saturation as well but at a higher intensity. From these results the probe and pump beams were set to intensities just below the saturation value, ≈ 50 mW cm^{-2} and 300 mW cm^{-2} respectively, for

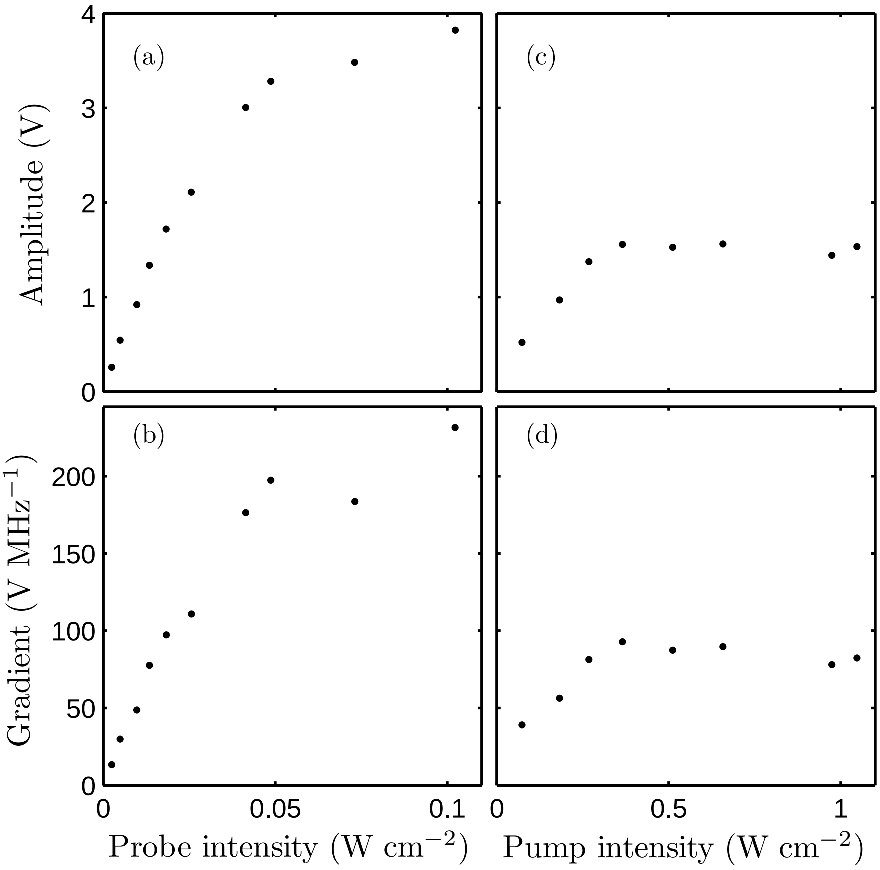

Figure 3.9: The amplitude, (a), and gradient, (b), of the SDFM error signal as a function of probe beam intensity with a pump intensity of 1.02 W cm^{-2}. The amplitude, (c), and gradient, (d), of the SDFM error signal as a function of pump beam intensity with a probe intensity of 0.017 W cm^{-2}. The RF voltage for the EOM was set to 6 V.

locking of the laser.

The amplitude and gradient as a function of modulation voltage applied to the EOM are shown in figures 3.10a and 3.10b respectively. Unfortunately the axis cannot be calibrated into the ratio of sideband amplitude to carrier amplitude as a Fabry-Pérot etalon was not available at a wavelength of 461 nm. Low laser beam intensities were used for this test to ensure that atomic saturation did not influence the data and the trends are a result of the modulation voltage only. The optimal modulation depth arises because the modulation depth is proportional to the square root of the product of the power in the sidebands and the carrier, which as the total power is constant means there is an optimum ratio for the beat measurement [81]. The amplitude increases with modulation voltage at low modulation voltages before reaching a maximum and decreasing again. The gradient shows similar behaviour. From these tests the optimal modulation voltage used for laser locking in SDFM was 6 V.

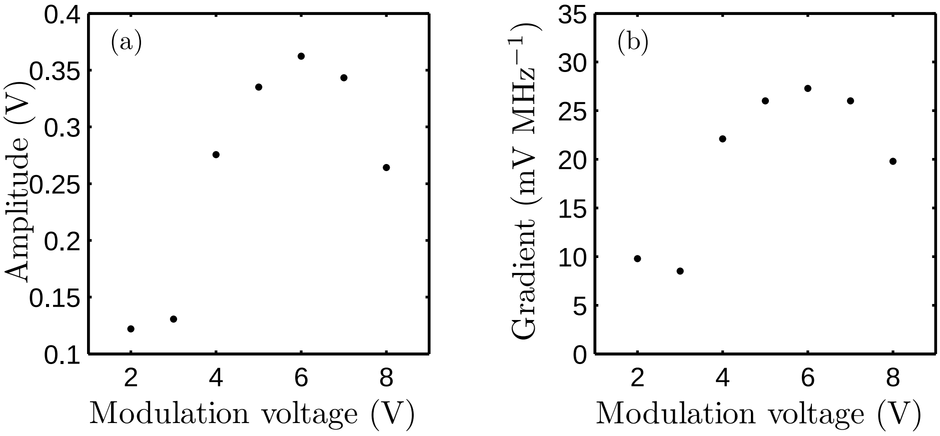

Figure 3.10: Characterization of the SDFM signal with applied modulation voltage for the amplitude (a), and the gradient (b). For these tests the probe intensity was 2.7 mW cm^{-2}, and the pump intensity was 0.15 W cm^{-2}.

3.3.2 Modulation transfer spectroscopy

In modulation transfer spectroscopy the pump beam is modulated and the probe beam detected [101, 104]. The dispersive signal arises due to a four wave mixing process [105]. The carrier and sideband of the pump interact with the probe via the non-linear susceptibility (χ^3) of the atomic vapour to create sidebands on the probe [106]. The sidebands of the probe then beat with the carrier on the photodiode and the signal demodulated in the same way as in SDFM.

An advantage of MT over SDFM is that the Doppler background is removed

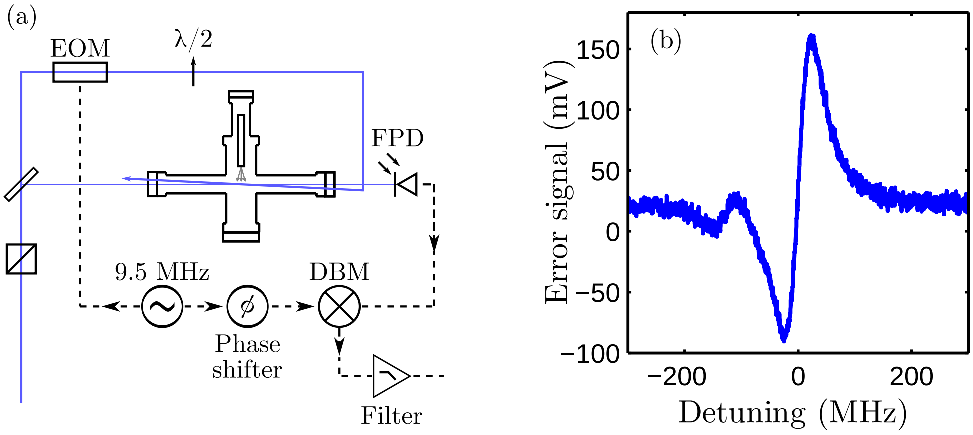

Figure 3.11: (a) Optical (solid line) and electronic (dashed line) layout for modulation transfer spectroscopy. (b) Example modulation transfer spectroscopy error signal in the thermal cell. The probe beam intensity is 6 mW cm^{-2} and the pump beam intensity is 0.97 W cm^{-2}.

and the zero crossing is therefore more stable as small changes in atomic absorption or magnetic field will not change the locking frequency. The reason for the removal of the Doppler background is that there is only transfer of modulation when the pump and probe beams are simultaneously resonant, i.e. with the zero velocity class of atoms.

The beam layout for MT is shown in figure 3.11a. The setup is the same as for SDFM except the EOM has been moved from the probe beam to the pump beam. An example MT spectrum is shown in figure 3.11b. The slight non-zero background is an electronic offset which can be controlled with a lock circuit.

The MT error signal was not characterized as it was not used for laser locking for the cold atom experiment due to the reasons given in section 3.4.3.

Conclusion

Modulation spectroscopy leads to sharp dispersion signals ideal for laser locking. SDFM is used for locking the laser to the singlet $5s^2\ {}^1S_0 \rightarrow 5s5p\ {}^1P_1$

transition used for cooling and trapping of strontium. Although stability data in the second cell could not be taken, experiments on the cold atoms suggest that the stability is better than the polarization spectroscopy locking system.

3.4 Electromagnetically induced transparency spectroscopy

In previous Rydberg excitation experiments in our cold atom setup the excitation laser was not locked [46–48]. The ability to do coherent excitation of the Rydberg atoms is desirable. As we use a two-photon excitation scheme to excite to Rydberg states, the Rydberg coupling laser needs to be phase coherent with the probe laser, i.e. needs to be locked to it. To lock the coupling laser an EIT locking scheme is used [83].

3.4.1 EIT in a vapour cell

To use the EIT locking scheme, a Rydberg EIT signal is required. We have previously used a thermal beam to do spectroscopy of low lying Rydberg states [107]. For the EIT locking the vapour cell will be used again. The coupling laser light is created by another frequency doubled diode laser (*Toptica TA-SHG 110*) operating at a wavelength of 413 nm. The level setup is the same as shown in figure 2.4a. The beam layout for EIT is the same as for saturated absorption spectroscopy, as seen in figure 3.1a, except the pump beam is replaced with a laser beam coupling to the Rydberg state. Figure 3.12a shows a spectrum with the probe scanning across the $5s^2\ ^1S_0 \rightarrow 5s5p\ ^1P_1$ resonance and the coupling laser on resonance with the two-photon transition to the $5s56d\ ^1D_2$ Rydberg state. A 5 % change in transmission is seen. As discussed in section 2.2.3, the small change in transmission is likely due to finite laser linewidths of the probe and coupling beams. A higher absorption of the probe light, without a coupling beam, would also increase the overall change in transmission with a coupling beam. However, as we wish to do on resonance CPT in the cold atoms, the coupling laser has to be locked off resonance such that when an AOM is used to direct light to the cold atoms that beam is on resonance. A spectrum is shown in figure 3.12b with the coupling laser at the detuning required for locking. The feature is much smaller now, with the change in transmission ≈ 2 % due to the velocity distribution of the atoms in the vapour cell.

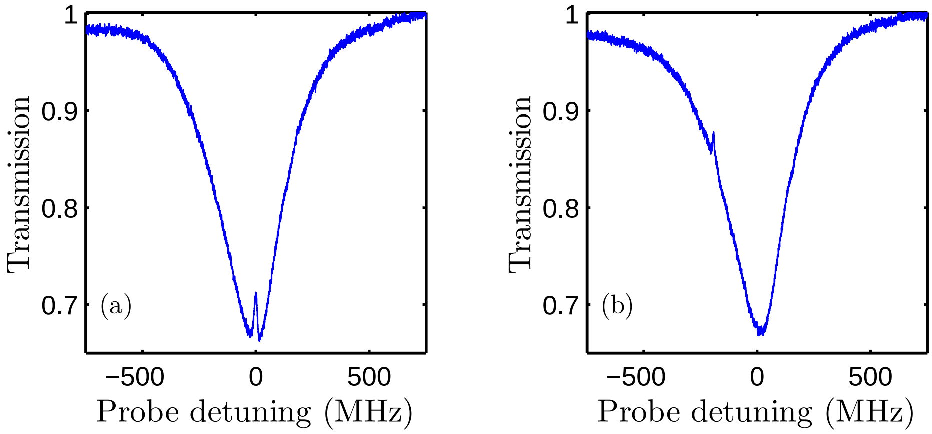

Figure 3.12: EIT spectroscopy of the 5s56d $^1D_2$ state in the thermal cell. The probe beam is scanned over the Doppler width of the absorption while the coupling laser is held at a constant frequency. The coupling laser is: (a) on resonance, (b) at the detuning required for locking.

3.4.2 Frequency modulated EIT spectroscopy

To convert the EIT absorption signal seen in figure 3.12 into a dispersion signal a technique based upon frequency modulation spectroscopy is used [83]. The optical and electronic layout necessary for frequency modulated EIT spectroscopy is shown in figure 3.13a. A probe beam is modulated with an EOM and detected on a fast photodiode (FPD). A coupling laser to excite to Rydberg states is aligned counter-propagating through the vapour cell using a dichroic mirror. To increase the coupling Rabi frequency the beam is focused to approximately 120 μm. The probe beam has to be smaller than the coupling beam, and is therefore focused to approximately 90 μm. The probe and coupling beams are circularly polarized using $\lambda/4$ waveplates to select the most strongly coupled m_J states. The signal is again demodulated using a mixer. As the EIT signal is so small, the coupling laser is amplitude modulated as well using an optical chopper (*Scitec Instruments 300H*) and demodulated using a lock-in amplifier (*Stanford Research Systems SR510*). The lock-in amplifier allows us to strongly filter the signal to remove noise as well. The optical chopper modulates the coupling beam at a frequency of 1 kHz, and the lock-in amplifier has a time constant of 30 ms, limiting the available bandwidth for frequency correction.

An example EIT error signal for the 5s56d $^1\mathrm{D}_2$ after the lock-in amplifier used for locking is shown in figure 3.13b. The probe laser is locked using SDFM and the coupling laser is scanned to generate the error signal. A sharp slope is obtained, usable for locking. The signal is non-symmetric due to the steep side of the Doppler profile on which it is found. The non-symmetry means the exact resonance position is hard to locate, meaning the coupling laser could be off-resonance by several MHz.

The stability of the EIT lock is difficult to measure as there is not enough power available from the laser for two separate EIT spectroscopy setups. However, by doing CPT spectroscopy in the cold atom setup, see chapter 4, and fitting the centre of the measured feature over time an upper limit on the frequency drift of the lock can be obtained. The lock drifts by no more than 1 MHz per hour. The short term linewidth of the laser is difficult to measure without doing a beat measurement, though an approximate value can be obtained by fitting spectra in the cold atoms with optical Bloch equation simulations, see section 4.6 for further details.

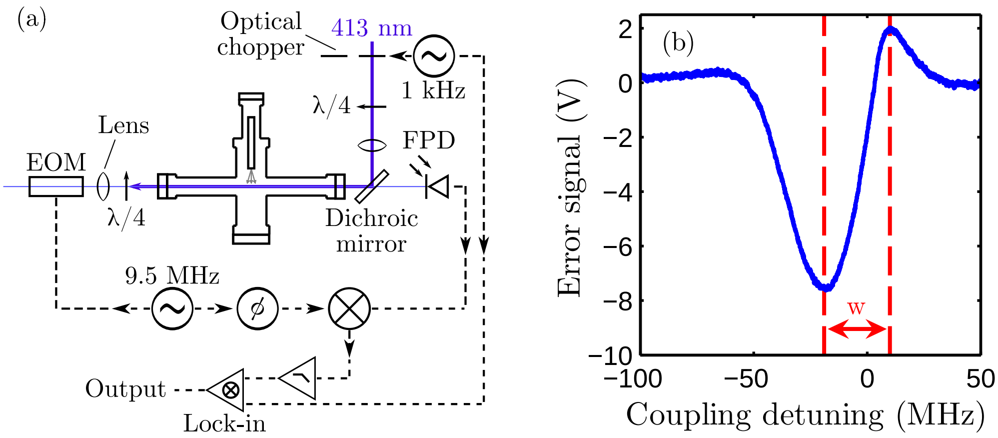

Figure 3.13: (a) The optical (solid line) and electronic (dashed line) setup for generating an EIT error signal. (b) Example EIT error signal of the 5s56d $^1D_2$ state in the thermal cell used for locking the coupling laser. The widths plotted in figures 3.14b and 3.14d, are the frequency difference between the dashed lines, labeled w.

The amplitude and width of the EIT locking feature, for the 5s56d $^1D_2$ state, as a function of the probe and coupling power are shown in figure 3.14. The amplitude of the feature is defined as the difference between the maximum and minimum of the feature. The width is defined as the frequency difference between the maximum and minimum amplitudes, shown by the difference between the dashed line in figure 3.13b, labeled w. The gradient is not used as the slope is not linear over a large enough section. The amplitude as a function of probe power, figure 3.14a, increases linearly with probe power; as expected since the probe intensity is much lower than saturation and the signal is proportional to light incident on the photodiode. The width as a function of probe power, figure 3.14b, increases due to an increase in Rabi frequency and then plateaus at a value slightly below the FWHM of the probe transition, though the method by which the width is defined could explain the difference. The amplitude as a function of coupling power, figure 3.14c, shows a slight saturation type behaviour due to the Rabi frequency of the coupling beam. The width as a function of coupling power, figure 3.14d, has

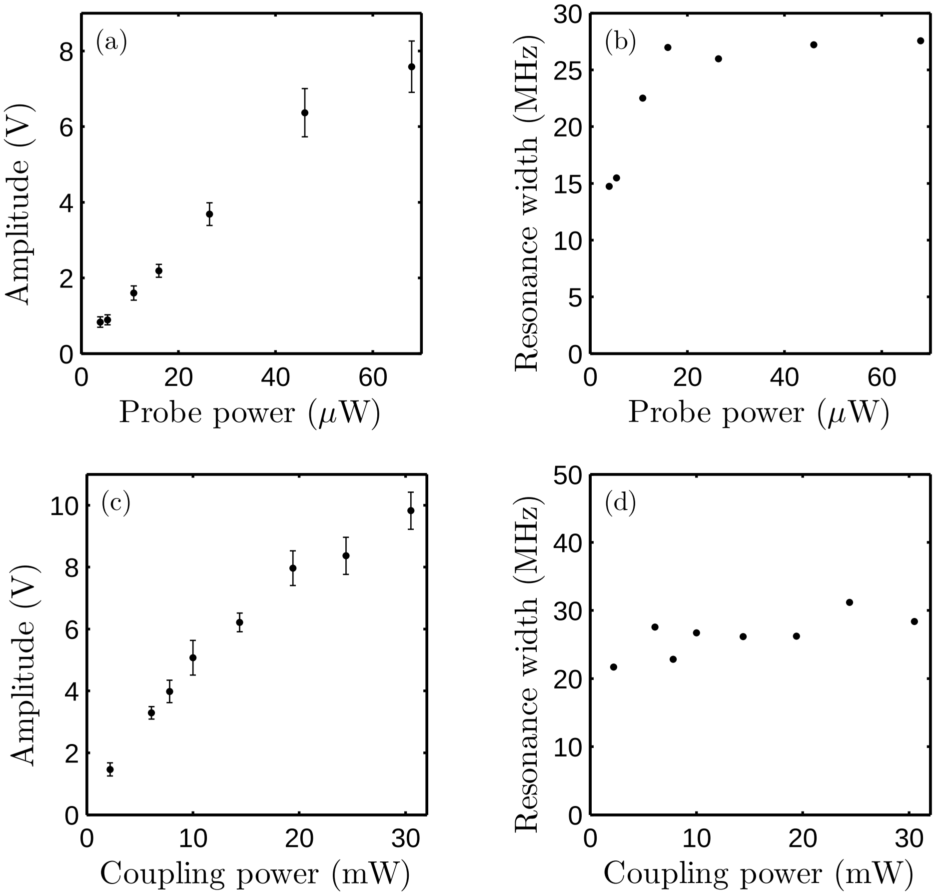

Figure 3.14: Variation of the amplitude, (a), and the width, (b), of the EIT error signal with probe beam intensity, coupling beam intensity fixed at 18.3 mW. Variation of the amplitude, (c), and the width, (d), of the EIT error signal with probe beam intensity fixed at 69 μW.

a very slight increase due to the increase in Rabi frequency of the coupling beam broadening the transition.

3.4.3 Laser locking setup

Due to experimental constraints only one EOM was available for locking both the probe and coupling lasers. Further, only a single instance of the first generation vapour cell was available. The probe lock and the coupling lock also had to be detuned by $\approx$ 200 MHz due to the AOMs available.

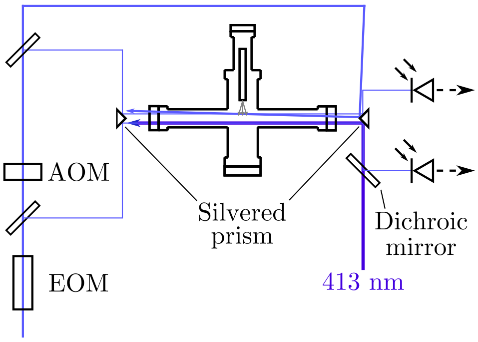

Figure 3.15: The final setup for both SDFM and EIT locking in the first generation cell.

These facts limited the locking setup. The final locking setup is shown in figure 3.15. Sidebands are applied to all 461 nm laser beams. A probe beam for EIT locking is split off by a glass plate. The laser beams for the 5s^2 ^{1}S$_0$ $\rightarrow$ 5s5p ^{1}P$_1$ lock then pass through an AOM. A probe beam for the SDFM lock is split off using another glass plate. The two probe beams are made parallel and sent through the cell using the external faces of a silvered right angle prism (*OptoSigma, PALR-LEGS/S7/BK7*). The separation of the centres of the probe beams is ≈ 3 mm. The pump beam for the SDFM and the coupling beam for the EIT similarly enter the vapour cell reflected off of a right angle prism. The probe beams are detected on fast photodiodes and the signals are sent to demodulation electronics to generate the locking signals.

The pump and probe of the SDFM setup both have sidebands on, indicating we are not doing purely SDFM spectroscopy. However, we have not noticed any problems caused by MT that should be present.

3.4.4 EIT error signals at different n and l

As the dipole-dipole interaction scales as n^{11} it can be advantageous to lock the coupling laser to as high an n as possible. Unfortunately the oscillator strength decreases as $n^{-3/2}$, so the EIT feature for locking decreases with constant coupling power. Figure 3.16 shows the locking signal at several different 5snd ^{1}D$_2$ states. The locking signal amplitude clearly decreases with n to the point where the lock is very unreliable. The highest n where a stable/reliable locking signal was achieved was 5s75d ^{1}D$_2$, shown in (e). As the signal to noise ratio decreases with n, the lock also becomes less tight so the relative linewidth of the excitation becomes wider.

As discussed in chapter 2 the sign of the interactions between different l states is different, it is therefore useful to be able to lock to different l states to access the different interaction regimes. As the probe laser can only be resonant with the 5s5p ^{1}P$_1$ state, the dipole allowed states accessible with the coupling laser are 5sns ^{1}S$_0$ and 5snd ^{1}D$_2$ states. Figure 3.16 shows how the 5s57s ^{1}S$_0$ locking signal compares to the 5snd ^{1}D$_2$ locking signals. The 5s57s ^{1}S$_0$ is the closest 5sns ^{1}S$_0$ state in energy to the 5s56d ^{1}D$_2$ state. The 5s57s ^{1}S$_0$ state is clearly much more weakly coupled than the 5s56d ^{1}D$_2$ state. The reason for lower coupling is the amount of degenerate sub-levels each state contains [108]. The 5sns ^{1}S$_0$ state has only one sub-level, whereas the 5snd ^{1}D$_2$ state has five. The size of the error signals is in approximate agreement with this scaling. Due to the very poor locking signals for 5sns ^{1}S$_0$ states, they are not used in the majority of the experiments in this thesis. The maximum power out of the coupling laser limited the Rabi frequency that could be reached, hence the size of the error signals at higher n and for the 5sns ^{1}S$_0$ states.

Conclusion

We have a compact vapour cell for spectroscopy of thermal strontium atoms. Several different spectroscopic techniques have been investigated and characterized, both unmodulated: polarization spectroscopy and sub-Doppler DAVLL; and modulated: sub-Doppler frequency modulation spectroscopy

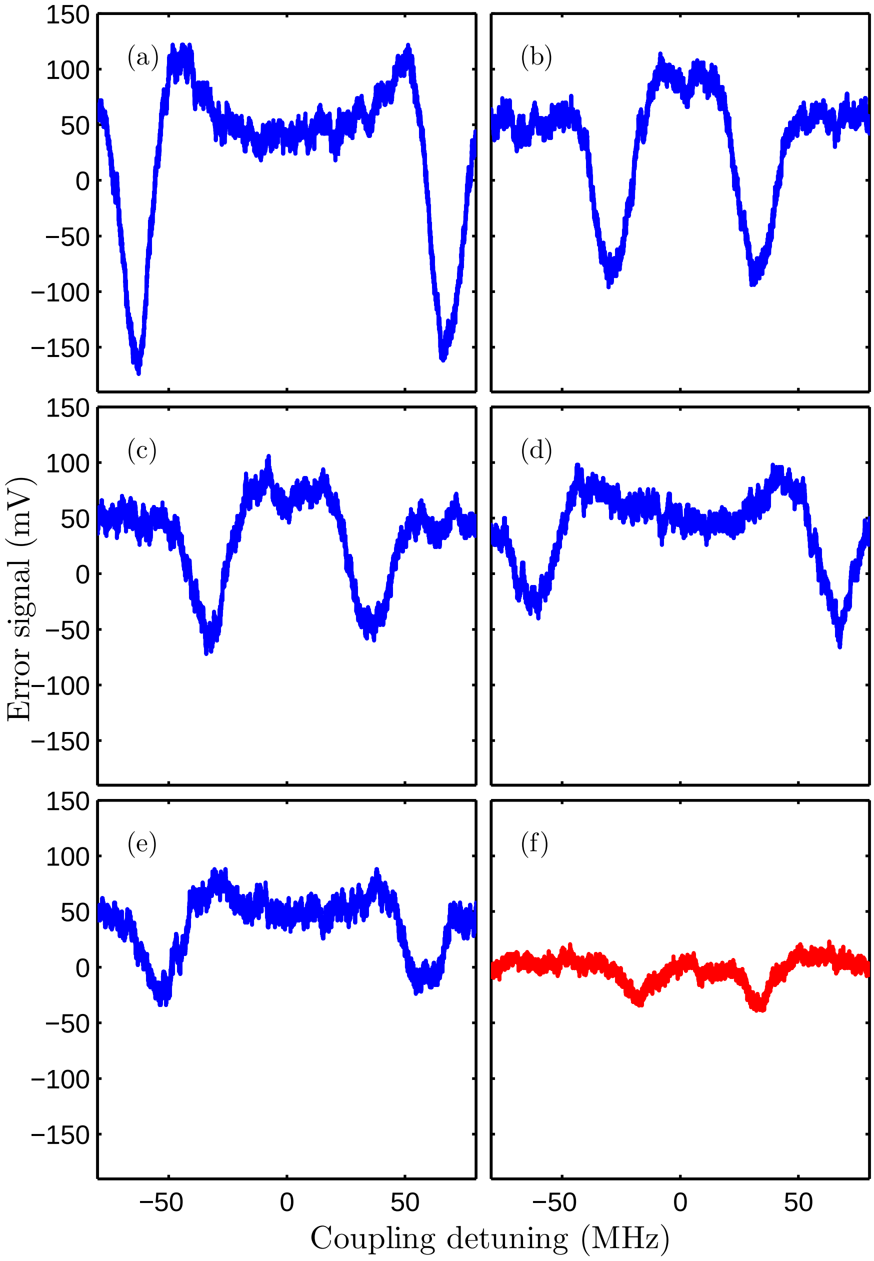

Figure 3.16: (a)-(e) The EIT error signal for the $5snd\ ^1D_2$ state at different n. n = (a) 56, (b) 64, (c) 68, (d) 72, (e) 75. (f) The EIT error signal for the $5s57s\ ^1S_0$ state. The x and y axis scales are the same for ease of comparison.

and modulation transfer spectroscopy.

Of the unmodulated locking techniques polarization spectroscopy gave a superior stability to sub-Doppler DAVLL, 0.8 MHz per hour drift RMS, compared to 3.0 MHz per hour drift RMS, probably due to the Doppler background in sub-Doppler DAVLL.

Thermal effects causing a birefringence in the polarization optics limited the performance of the polarization spectroscopy locking setup. To circumvent this source of instability, modulation based techniques were employed. Sub-Doppler FM was used over MT due to the need for a second frequency modulated probe beam for the EIT locking.

These techniques have lead to the ability to lock a laser to the $5s^2\ {}^1S_0 \rightarrow 5s5p\ {}^1P_1$ transition for several hours with only small frequency fluctuations. The stability of this laser locking system enables the reliable creation of a cold ensemble of atoms, described in the next chapter.

By conducting EIT spectroscopy in the thermal cell an error signal is obtained which allows the stabilization of a laser resonant to the $5s5p\ {}^1P_1 \rightarrow 5sns(d)$ transitions to Rydberg states up to $n = 75$. The ability to frequency stabilize the coupling laser means that coherent population trapping of Rydberg states in the cold ensemble can be achieved.

Chapter 4

Coherent population trapping in cold atoms

We wish to reduce the translational motion of the atoms and create a "frozen Rydberg gas" [109] such that the motion of the atoms during excitation can be essentially neglected. Creating a frozen gas allows us to study the population dynamics and interactions solely.

To cool and trap the atoms several requirements need to be met: a source of strontium atoms in vacuum; a way of applying a quadrupolar magnetic field; and a near-resonant laser system [110]. The method of controlling the laser frequency was described in chapter 3.

After cooling the atoms we wish to coherently excite the atoms to specific magnetic sub-levels in controlled Rydberg states. A simulation to model the population dynamics with experimental parameters will be necessary in understanding our experiment.

This chapter will:

- describe the vacuum chamber and method of creating and slowing a beam of strontium atoms in section 4.1

- detail ion detection in section 4.2
- describe the mechanisms of autoionization and spontaneous ionization in sections 4.3 and 4.4
- detail how we coherently excite Rydberg atoms in section 4.5
- describe the OBE simulation used to fit our spectra and model population dynamics in section 4.6
- describe the effect of applied magnetic and electric fields on the spectra in section 4.7

4.1 Cold atom setup

4.1.1 Vacuum chamber and cold atom source

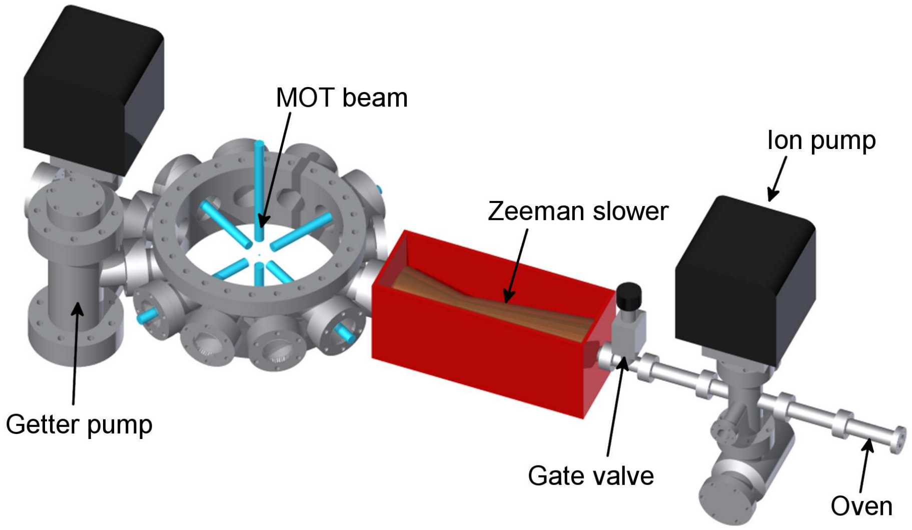

Figure 4.1: Computer aided design (CAD) image of the vacuum chamber setup.

A CAD image of the vacuum chamber is shown in figure 4.1. The vacuum chamber and cold atom source were developed during the thesis of J. Millen and further details can be found in [46]. To create an atomic vapour, dendritic pieces of 99.9 % pure strontium (*Sigma-Aldrich 460346-5G*) are heated in the oven using resistive heater wire (*Thermocoax SEI 20/150*). The vapour is then collimated using 169 stainless steel capillaries that are 170 μm in diameter and 8 mm in length, which gives the atomic beam a full-width divergence of 43 mrad. The oven and capillary design is based on the work of [111]. The oven is separated from the main chamber by a gate valve allowing replenishment of the strontium when the oven becomes empty without breaking the vacuum of the main chamber. The oven region and the main chamber are separately pumped by 20 l s^{-1} ion pumps (*Gamma Vacuum TiTan 20S*). The ion pump gauge in the main chamber indicates a background pressure of $\approx 3 \times 10^{-11}$ torr when the gate valve is closed and $\approx 1 \times 10^{-10}$ torr when the gate valve is open, suggesting a very good background vacuum. The main chamber is also pumped by a non-evaporative getter pump (*SAES Getters CapaciTorr B200*) to remove hydrogen. The hot strontium atoms from the oven are continually travelling through the magneto-optical trap (MOT), colliding with the trapped atoms as there is no shutter in the atomic beam.

The oven is heated to $\approx$ 900 K, giving the strontium atoms a mean velocity along the slower of $\approx$ 500 m s^{-1}. To slow the atoms to a trappable velocity a Zeeman slower of the "spin-flip" type is used [60]. The magnetic field for the Zeeman slower was calculated by Dr. M.P.A. Jones based upon algorithms from [112]. The coils of the Zeeman slower are housed in a mild steel yoke (red box in figure 4.1) as this yoke helps to reduce the magnetic field at the end of the slower. The Zeeman slowing laser beam is counter-propagating to the atomic beam and has a $1/e^2$ waist of 13.62 mm and 8.88 mm, parallel and perpendicular to the bench respectively, at the entrance to the vacuum chamber. The slowing beam is focused using an $f = +750$ mm lens to counteract the divergence of the atomic beam. It is estimated that focusing the Zeeman slowing laser beam increases the capture efficiency by a factor of three [112]. The Zeeman slowing beam has a detuning of -490 MHz (-15.3 Γ)

from the $5s^2\ {}^1S_0 \rightarrow 5s5p\ {}^1D_2$ transition. A few percent of the atomic flux is slowed to a trappable velocity.

4.1.2 Magneto-optical trap

The Zeeman slowed atoms are trapped and cooled in a six beam retro-reflected magneto-optical trap [113]. The three pairs of beams are orthogonal. The beam layout for the MOT beams is shown in figure 4.2. The MOT beams have a $1/e^2$ waist of 6.35 mm and 4.44 mm, and are detuned by -36 MHz (-1.12 Γ). The quadrupolar magnetic field is created by a pair of anti-Helmholtz coils inside the vacuum chamber; these can be seen at the top and bottom of figure 4.3a. The trapping gradient used in the experiments in this thesis was 30 G cm^{-1}. Power dissipation limitations within the coils meant larger fields could not be used. The quadrupolar field is switched using the circuit in shown in figure A.4. Figure 4.3a shows a true colour image of the MOT being continually loaded from the Zeeman slowed beam, taken on a webcam.

To calculate the atom number and density of the cold atom cloud fluorescence imaging is used. The MOT beams are pulsed on and an image taken on a charge-coupled device (CCD) camera (*pco. PixelFly qe*). The camera has a $2f$ imaging system and a solid angle of 0.0037 steradian. Trap populations of approximately 5×10^6 atoms are routinely trapped in the MOT with a generally Gaussian distribution with a $1/e^2$ width of $\approx 500\ \mu$m. The peak density, n_0, is calculated from

$$n_0 = \frac{N_\mathrm{a}}{(2\pi)^{3/2}\sigma_x\sigma_y\sigma_z}\ , \tag{4.1}$$

where N_a is the atom number, σ_x and σ_y are the fitted Gaussian widths of the camera image in orthogonal directions, and σ_z, the unseen dimension, set to be the geometric mean of the two observed dimensions. A typical peak

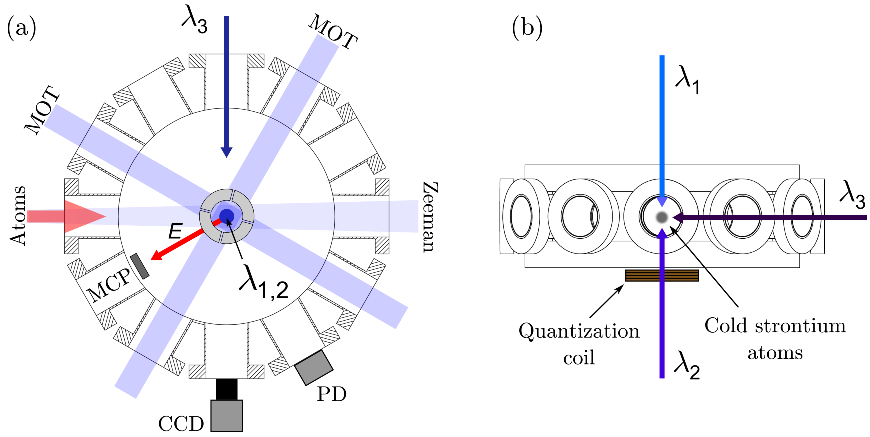

Figure 4.2: The optical layout for trapping atomic strontium and exciting it to Rydberg states. There are twelve DN40CF flanges in the x-y plane of the chamber, of which 9 are viewports, another DN40CD viewport is on the top of the chamber and a DN200CF viewport is on the bottom. (a) Top-down view of the vacuum chamber, along the axis of the excitation beams and the vertical MOT beam. The split-ring electrode geometry is shown in the centre. The arrow labeled E shows the direction of the electric field used to direct ions to the MCP. (b) Side view of the vacuum chamber, along the Zeeman slower axis.

density of 2×10^9 atoms cm^{-3} during Rydberg excitation experiments are seen. These measurements compare well with other groups measurements of strontium MOTs operating on the 461 nm transition [114–117]. The temperature of the MOT was measured using a time-of-flight technique [118] to be 5.5 ± 0.5 mK.

The variation of the atom number (red squares) and atomic density (black circles) with MOT beam power is shown in figure 4.3b. The camera images used to calculate the atom number and density were taken with the MOT being continually loaded. The MOT beam power is measured before the beam is split into the three orthogonal pairs. The Zeeman beam power was set to 44 mW for this experiment. The atom number and density follow similar trends indicating that the MOT is in the number-limited regime [110]. In the number-limited regime the physical size of the MOT stays the same

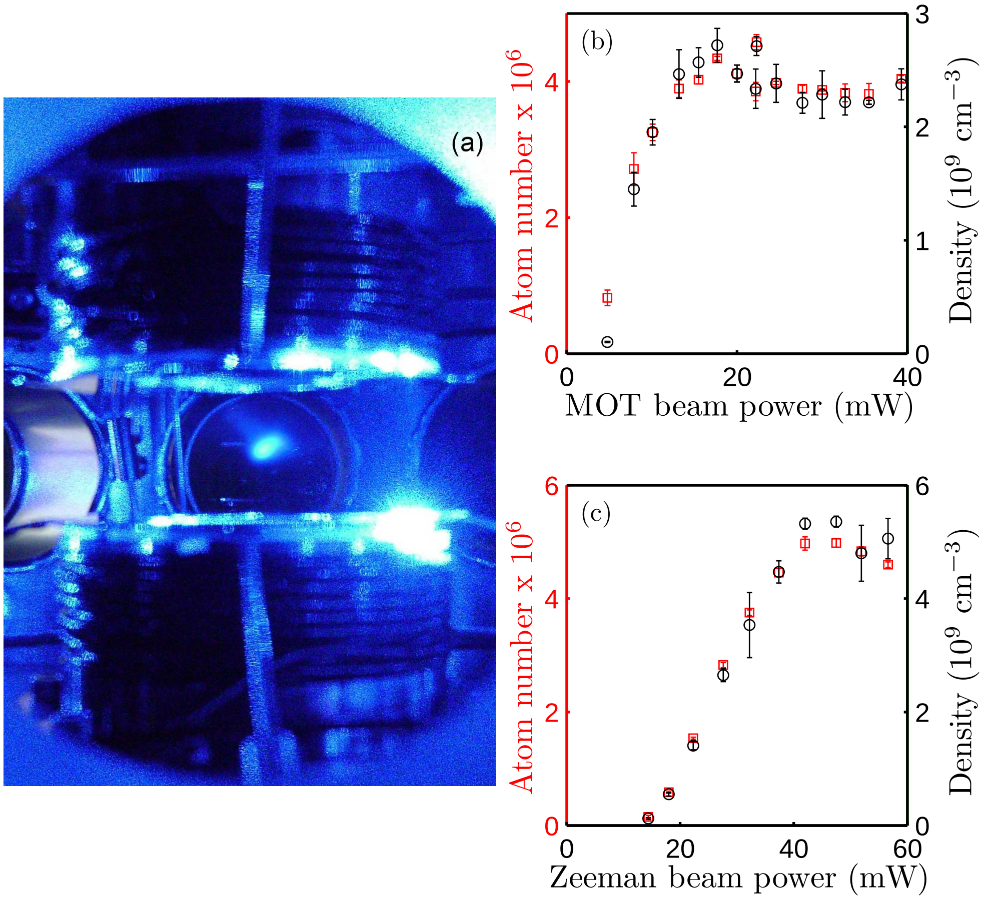

Figure 4.3: (a) Photograph of the MOT taken using a webcam. The MOT is being continually loaded from the Zeeman beam using the $5s^2\ {}^1S_0 \rightarrow 5s5p\ {}^1P_1$ transition. The coils used to create the magnetic quadrupole for the MOT can be seen at the top and bottom of the figure. The split ring electrodes are attached to the MOT facing sides of the coil formers. (b) The variation in atom number (red squares) and density (black circles) with MOT beam power. (c) The variation in atom number (red squares) and density (black circles) with Zeeman beam power.

and more trapped atoms increase the density. When the repump lasers are used, section 4.1.3, the MOT enters the density-limited regime [110]. In the density-limited regime there are enough atoms in the MOT such that photons emitted by trapped atoms have a non-negligible probability of absorption by other trapped atoms. Re-absorption causes a repulsive force between trapped atoms, limiting the density.

There is a threshold power associated with trapping the atoms as the atoms have to scatter enough photons to be cooled sufficiently to become trapped. The atom number increases initially with power since a greater proportion of the velocity distribution of the Zeeman slowed atoms can be trapped. The saturation in atom number with MOT beam power is caused by power broadening of the trapping transition [119]. The power broadening increases the spectral overlap of the counter-propagating trapping beams causing a reduction in the frictional force. At higher trapping intensities still, the atom number starts to decrease as atoms are pumped into the untrapped 5s4d $^1D_2$ state [114].

The variation of the atom number (red squares) and atomic density (black circles) with Zeeman slower beam power is shown in figure 4.3c. The MOT beam power was set to 24.5 mW for this experiment. Again the atom number and density follow similar trends. A threshold behaviour is seen as the thermal atoms need to scatter a certain amount of photons to be slowed sufficiently to be trapped by the MOT. The saturation of atom number with Zeeman slower power is caused by pumping of the atoms in the slowing beam into the unslowed 5s4d $^1D_2$ state.

Having characterized the MOT, for the rest of the experiments in this thesis the MOT beam power was set to $\approx$ 20 mW and the Zeeman slower power to $\approx$ 45 mW, as the atom number has saturated at these values.

4.1.3 Repump lasers

The cooling transition, 5s^2 $^1S_0 \rightarrow$ 5s5p $^1P_1$, is not a closed transition. There is a slight leak (the branching ratio is $\sim$ 1:50000 [120]) to the 5s4d $^1D_2$ state as shown in figure 4.4. From the 5s4d $^1D_2$ state the electron can decay into the triplet 5s5p $^3P_2$ or 5s5p $^3P_1$ states. The 5s5p $^3P_1$ state will decay back to the ground state along the 689 nm transition with a lifetime of 21 μs. However, the transition from the 5s5p $^3P_2$ state to the ground state is doubly forbidden and has a lifetime of 13 minutes [121] and, therefore, population that enters the 5s5p $^3P_2$ state is essentially lost from the trap.

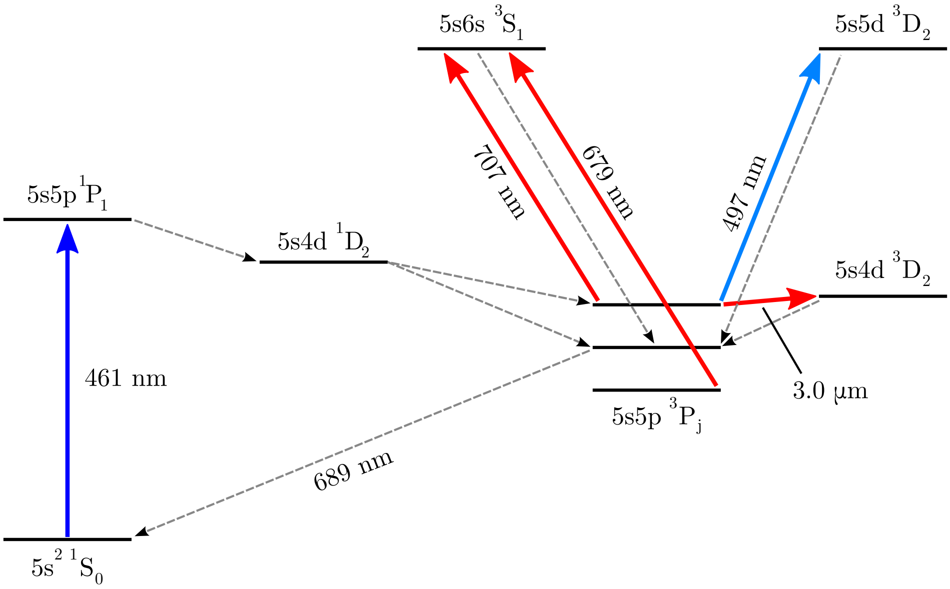

Figure 4.4: Energy level diagram of strontium showing three different repumping schemes. The j values of the 5s5p ^3P_j states are 2, 1, 0 from top to bottom.

There are several schemes which "repump" the population in the 5s5p $^3P_2$ back to the ground state via the 5s5p $^3P_1$ state. Two of the schemes require a single laser and go via the 5s4d or 5s5d $^3D_2$ states [122, 123]. Another scheme using two lasers and transferring population via the 5s6s $^3S_1$ state is also available [124]. Due to the availability of laser diodes the repump scheme via the 5s6s $^3S_1$ state was chosen. One laser at 707 nm is resonant with the 5s5p $^3P_2 \rightarrow$ 5s6s $^3S_1$ transition. From the 5s6s $^3S_1$ state the 5s5p $^3P_{0,1,2}$ states are populated via spontaneous decay. Unfortunately the $^3P_0$ is also very long lived [120] and population will become trapped here as well. A second laser at 679 nm resonant with the 5s5p $^3P_0 \rightarrow$ 5s6s $^3S_1$ transition is therefore also required. The laser diodes used were the *SDL-7311* at 679 nm and the *Toptica LD-0710-0010-AR-1* at 707 nm.

The diodes were built into Littrow configuration external cavity diode lasers (ECDLs) [125]. Stabilizing these lasers spectroscopically is very challenging due to the minimal population in these states in a thermal cell. A transfer cavity could be used but these are expensive. A highly accurate wavemeter (*HighFinesse/Ångstrom WS7*) is available in our laboratory. A method using feedback from the wavemeter to the piezo connected to the diffraction grating of the two lasers was developed and implemented by D. Main and D. Sadler [126]. It was found that the stability of the wavemeter locking was sufficient for these transitions.

A strontium MOT can easily be created without the repump lasers, however, using them increases both atom number and density. For most experiments in this thesis the repump lasers are not used. The repumps were only applied during the experiments while trying to reach the blockade, section 6.1. The repumps increase atom number up to a maximum of $(3.5 \pm 0.2) \times 10^7$ and density up to a maximum of $(4.9 \pm 0.3) \times 10^9$ atoms cm^{-3} after an expansion time of 408 μs. The expansion time is due to having to wait for the quadrupolar magnetic field to decay, see section 4.7.1

4.1.4 Computer control

A multi-function reconfigurable input/output card (*National Instruments NI7831R*) is used to bring the experiment under computer control. The architecture for computer control is shown in figure 4.5. The card includes a field-programmable gate array (FPGA) which is used via its digital output (DO) ports to supply TTLs to switch processes on/off with 2 μs resolution. The FPGA also has analogue output (AO) and analogue input (AI) ports. The control program is written in *National Instruments LabVIEW*. An advantage of using *LabVIEW* is that a lot of the hardware used in the experiment has compatible drivers for it. The AI port is used to read in a signal from the photodiode pointing at the MOT. When the fluorescence reaches a set level the timing sequence shown in figure 4.12 is triggered. The DO is used to control the timing for the MOT and Zeeman slowing light, the camera trigger, the MOT quadrupole magnetic field and the quantization field. For the timing of the probe, coupling, and autoionization beams a pulse generator (*Berkeley Nucleonics Model 575 Digital Delay/Pulse Generator*) is used for the finer time resolution it provides (250 ps). The pulse generator can also give out voltage pulses up to 45 V. The electric fields used to direct ions towards the MCP are created using the pulse generator. Data from the oscilloscope (*Tektronix DPO 4054*) is read into the computer memory via the *LabVIEW* control program, as is data from the camera.

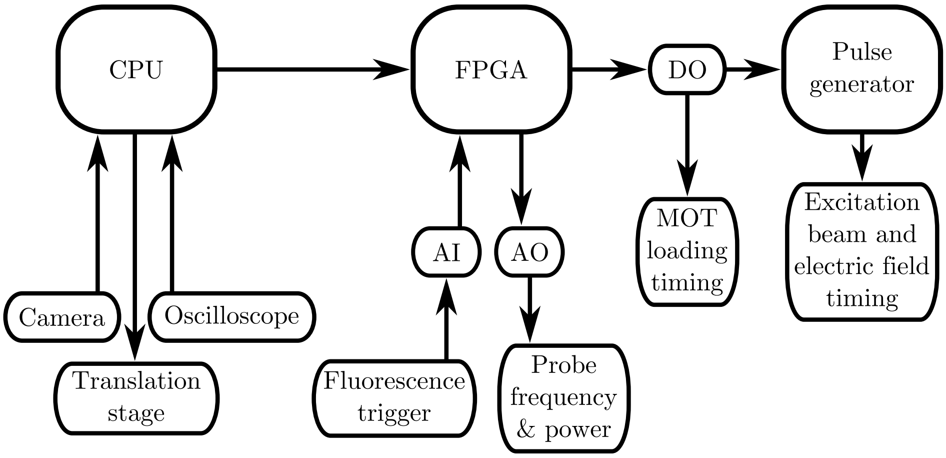

Figure 4.5: Computer control diagram. The oscilloscope and camera are read into the computer (CPU) and the translation stage 5.4 is controlled by the computer. The FPGA card is programmed by the *LabVIEW* control software. The fluorescence trigger is read into the FPGA card via the analogue input port. The frequency and power of the probe AOM are controlled by the analogue output port. The MOT beams, MOT coils, Zeeman beam and quantization coil are all controlled by the digital output port of the FPGA. The pulse generator is also triggered by the DO. The excitation beams and electric fields are controlled by the pulse generator.

Conclusion

With the vacuum chamber and Zeeman slower we can repeatably create cooled, trapped strontium atom clouds, of $(5.0\pm0.3)\times10^6$ atoms and densities of $(2.0 \pm 0.1) \times 10^9$ atoms cm^{-3}. Using the repump lasers these values are increased to $(3.5\pm0.2)\times10^7$ atoms and $(4.9\pm0.3)\times10^9$ atoms cm^{-3}. The time scale for loading a MOT on the 5s^2 ^{1}S$_0$ $\rightarrow$ 5s5p ^{1}P$_1$ transition is approximately 30 ms leading to a high repetition rate of the experiment.

4.2 Detecting Rydberg atoms

Now that the reliable source of cold, trapped strontium atoms has been described, the method of detecting Rydberg atoms will be discussed. The Rydberg atoms are created via two-photon excitation, discussed in section 4.5. The Rydberg atoms then ionize via autoionization, section 4.3, or spontaneous ionization, section 4.4. The ions are collected on a microchannel plate - MCP (*Hamamatsu Compact MCP Assembly F4655*) - see figure 4.6 for MCP setup. The MCP cathode is held at -2 kV to increase the signal per ion, while the anode is at 100 V. The MCP stack is a series of 4 μm channels inclined at 12°. Electrons or ions impacting the stack create an avalanche of electrons, and therefore a voltage pulse at the anode. The MCP has two amplifiers, which are attached to the output, referred to as the “first stage” amplifier, figure A.1, and the “second stage” amplifier, figure A.2.

To shield the atoms from the large electric field caused by the cathode it is covered by a metal mesh, referred to as the “grid” (*Goodfellow FE228710*). The grid is held at a small, constant, negative voltage to attract the ions to the MCP. To direct the ions from the MOT region where they are created to the MCP, a small electric field pulse is applied. The electric field pulse is created by a pair of split ring electrodes attached to the MOT coil formers, based on the design in [127]. The electrodes can be seen at the centre of figure 4.2a. The electrodes are grounded and then the pair furthest from the MCP have a positive voltage applied creating an electric field towards the MCP.

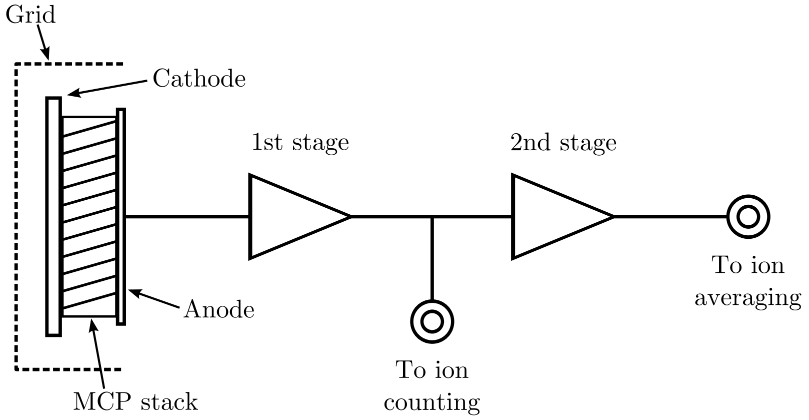

Figure 4.6: MCP and amplifier chain. A voltage pulse is created at the anode of the MCP. The signal used for ion counting is taken after the first stage amplifier. The signal for ion averaging is taken after the second stage amplifier.

With very low ion count rates, less than five counts per experimental shot, these pulses can be counted, see section 4.2.1. If the count rate increases however multiple counts will overlap and will therefore be missed making the counting method unreliable. For the regime of large count rates, more than five per shot, the ion signals are averaged on the oscilloscope over several experimental cycles, see section 4.2.2.

4.2.1 Ion counting

To count the ion pulses, the signal after the first stage amplifier is sent to the oscilloscope. The first stage amplifier is an inverting amplifier causing the ion pulses to be negative. Figure 4.7a shows an example trace with several ion pulses. The different heights of the pulses are due to the stochastic nature of gain within the MCP. Signal pulses straight out of the MCP are 500 ps in length. However, the first stage amplifier broadens these pulses to 2.5 ns. The oscilloscope is used as a discriminator and counter with the number of pulses below a certain reference value recorded per experimental shot. Two of the three troughs would have been counted and one missed. The reference level has to be set such that electronic ringing, as seen after the first trough, is not counted. Counting the ringing events as “true” events changes the statistics collected, though missing events does not, see section 5.5.2. The amount of “true” events (blue squares) and ringing events (black circles) missed as a function of reference level is shown in figure 4.7b. The missed count statistics come from analyzing 140 individual ion pulses. The red, dashed line indicates the reference level where there are no ringing events, -61 mV. At a reference level of -61 mV $\approx$ 40 % of “true” events are also missed.

The number of counts with no Rydberg atoms being created (“noise counts”) as a function of reference level is shown in figure 4.7c. Counts detected here are therefore either dark counts or electronic noise. The error bars on the mean ion count are the standard error on the mean. The number of “noise counts” tends to zero at a reference level of about -52 mV. Therefore, for the reference level used to avoid ringing events, -61 mV, there should be very few “noise counts”.

The time base resolution of the oscilloscope could cause some pulses to be missed: pulses can arrive separated by several μs in time due to the arrival time and gain processes in the MCP. Figure 4.7d shows the amount of counts detected with time base setting. The signal saturates at a setting of 400 ns, indicating all pulses are being collected. In all subsequent experiments where ion counting is used the time base setting of the oscilloscope is set to 1 μs to avoid missing counts.

The maximum dark count rate for the MCP is 33 pulses per second, as quoted in the manual. Dark counts are voltage pulses generated by the MCP that are indistinguishable from voltage pulses created by ions. If these dark counts are all larger than the set reference level, and are therefore counted, and are also randomly distributed in time then 0.00033 dark counts could be expected on average per experimental shot. The dark count rate is neglected as being very small compared to signal sizes.

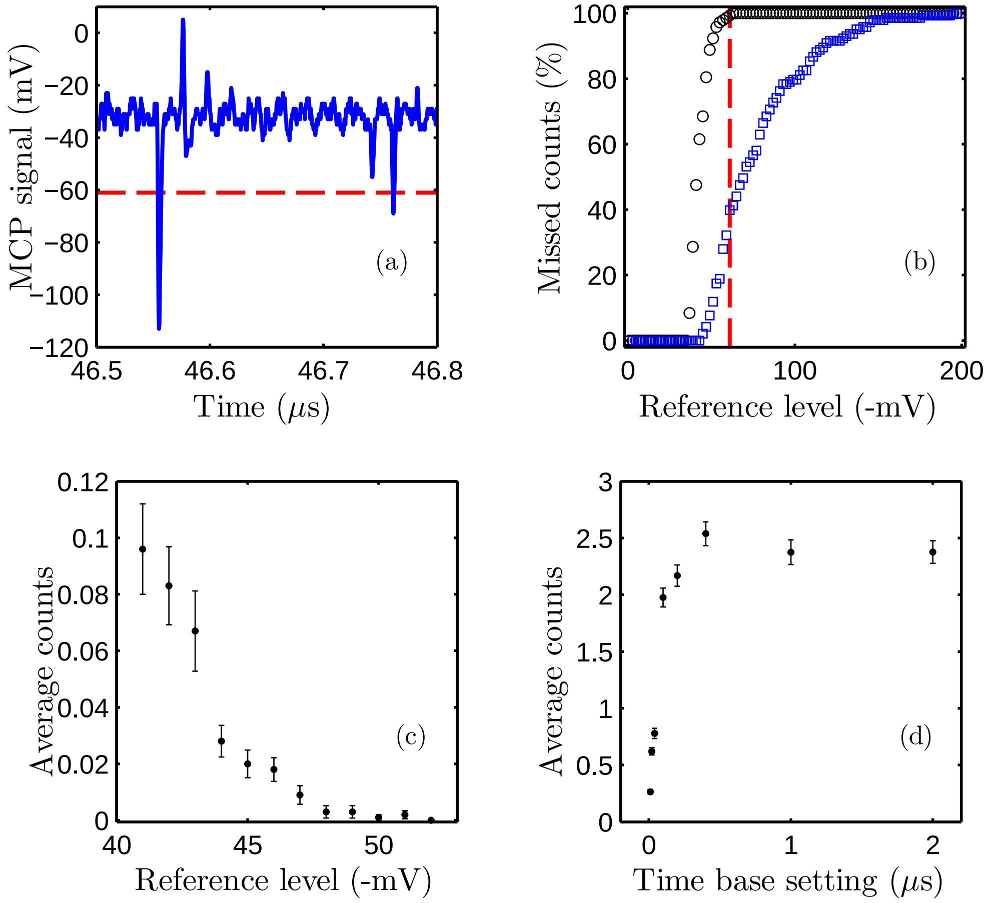

Figure 4.7: (a) Example of ion signals used for counting. The time delay is the time after the start of the excitation pulses and relates to the time of flight of the ions. The red, dashed line shows the reference level used in experiments for counting ions. (b) The percent of missed counts as a function of reference level for the initial peak (blue squares), and ringing peaks, i.e. double counting of ions (black circles). Again the red, dashed line shows the reference level used in experiments for counting ions. (c) Average amount of counts detected with no Rydberg atoms created as a function of reference level. (d) Average counts detected with time base setting on the oscilloscope.

For each run of the experimental sequence a number of pulses is detected by the oscilloscope. The number of pulses is then transferred to the *LabVIEW* control program. Therefore, for each experimental data point the entire pulse count distribution is collected. The pulse count distribution will be used for statistical analysis in section 5.5.2.

4.2.2 Average ion signals

When the number of ions per experimental shot is large, greater than five, a different method of collecting ion signal is employed. The second stage amplifier is added to increase signal size and it is also inverting. An example of the ion signals detected from the MCP with both amplifiers is shown in figure 4.8a. For each experimental data point the ion signal is averaged over 100 or 200 shots on the oscilloscope, and the data is transferred to the computer. An example of the averaged ion signal is shown in figure 4.8b. The offset of the ion signal is due to electronic offset of the amplifiers. The averaged ion signal has the electronic offset removed and is then integrated in time to give the total ion signal in units of Vμs. The reason for counting the ions at low signal size is that due to discretization and dynamic range on the oscilloscope, the signal to noise ratio becomes very poor for the integrated averaged ion signal method. Using the averaging technique no statistics can be recovered as only the mean ion signal is recorded.

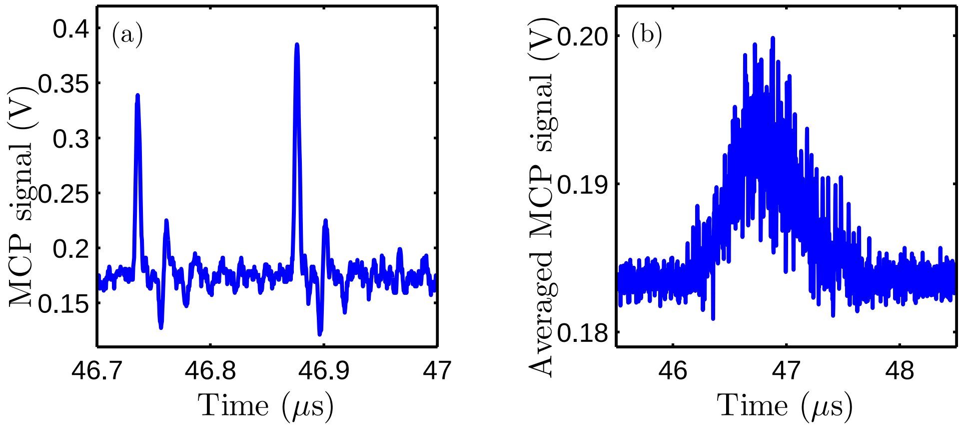

Figure 4.8: Ion signal from the MCP amplified by the first and second stage amplifier circuits, see figures A.1 and A.2. (a) Example of two individual ion pulses. (b) Example of the ion signal averaged over 200 shots.

Characterization of the collection electric fields

To ensure that as many of the created ions were collected as possible the grid voltage and electric field pulse were characterized. For these experiments the Rydberg laser was locked on resonance and the maximum integrated ion signal recorded.

Figure 4.9a shows the collected ion signal with applied grid voltage for the 5s56d $^1D_2$ state. Increasing the applied voltage to the grid, the signal increases before saturating. There are no ion focusing elements in the setup so ions directed toward the MCP by the electric field pulse will be spreading out and some will miss the MCP. Increasing the applied voltage to the grid attracts more of the ions towards the MCP, explaining the increase with voltage magnitude. The saturation of ion signal is probably due to all ions that are being directed toward the MCP being collected by it, so increasing the grid potential no longer increases the signal.

Figure 4.9b shows the ion signal amplitude with applied electric field voltage, taken at an electric field pulse length of 5 μs. The calibration from applied volts to electric field comes from fitting Stark maps, see [46]. A clear peak can be seen at 2.94 V cm^{-1}. The ion signal amplitude with applied electric field pulse length is shown in figure 4.9c, taken at a field strength of 4.2 V cm^{-1}. Again a clear peak can be seen in the data at a pulse length of 5 μs. It is not clear why this combination of electric field pulse amplitude and length should cause such a large peak in collected ion signal. Outside of the split ring electrodes the electric field switches direction. If the ions have reached this electric field reversing region when the field is still on they will be slowed/no longer directed to the MCP. For the rest of the experiments in this thesis electric field pulses had an amplitude of 2.94 V cm^{-1} and a length of 5 μs.

Strong electric fields cause ionization of Rydberg atoms [3]. However, for the 5s56d $^1D_2$ atoms, the field ionization value is 34 V cm^{-1} and therefore cannot be field ionized with the electric field strengths applied in our experiment.

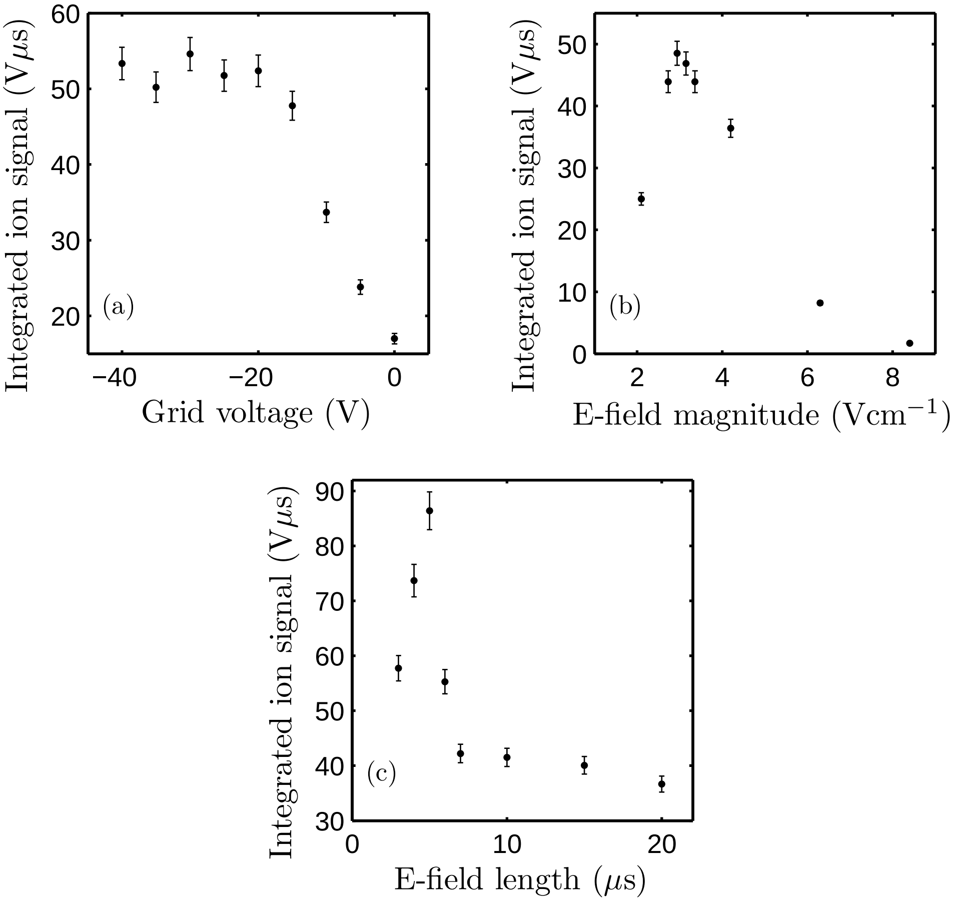

Figure 4.9: The Rydberg signal collected as a function of: (a) voltage applied to the grid covering the MCP; (b) the amplitude of the electric field applied to the split ring electrodes in the direction of E shown in figure 4.2; (c) the applied electric field length.

4.3 Autoionization

To study Rydberg atom dynamics via ionization a method of ionizing the Rydberg atoms at a specific time must be implemented. In most experiments on alkali metals an electric field pulse is used to field-ionize the Rydberg atoms with very high probability [3]. In our experiment however, we use a process called autoionization to ionize the Rydberg atoms.

Strontium is an alkaline-earth element and therefore has two valence electrons. After excitation of one electron to a Rydberg state the other electron is still available to undergo optical excitation. The process of exciting the core electron is called "isolated core excitation" (ICE) [1]. The atomic structure of the ICE atom approximates to the same as that of a singly ionized strontium atom. The presence of the Rydberg atom perturbs the line position and width of the transitions. As the Rydberg state increases in n or l the perturbations decrease and the atom becomes a better approximation to the ion, due to less wavefunction overlap.

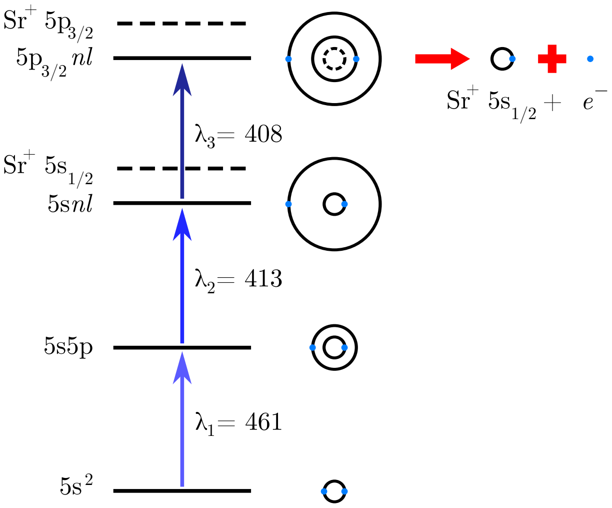

Figure 4.10: Isolated core excitation level scheme for autoionization. A visual representation of the atomic orbitals is also shown. The atoms are resonantly excited at the shown wavelengths. For $5p_{3/2}nl$ states of low l the atom ionizes (autoionization).

Figure 4.10 shows the level scheme for ICE and depicts a cartoon of the atomic orbitals. The doubly excited atom has an energy above the single ionization threshold of strontium. For low l Rydberg states ($l < 3$) the wavefunction overlap of the core electron and the Rydberg electron is large causing the atom to ionize very fast ($\sim$ 10 ps) with very high probability in a process called "autoionization" [1]. The resulting ion can be in any state of lower energy than the excited state, but is most likely to be found in the ionic ground state, Sr^+ $5s_{1/2}$ [128]. The very fast ionization of doubly excited atoms allows temporal information of the population dynamics to be obtained using ICE, e.g lifetimes of Rydberg states [47].

Another advantage to using autoionization over collecting spontaneous ionization, section 4.4, is the large increase in signal. An example trace of autoionization (black line) and spontaneous ionization (blue line) is shown in figure 4.11a.

The large cross-section for excitation means the spectrum is very broad and the ionization is very rapid. The ICE spectrum for the autoionizing transition of the 5s56d $^1D_2$ state is shown in figure 4.11b. The red line is a six channel multi-channel quantum defect theory (MQDT) fit [129]. Details of the fit can be found in [46, 48]. The shape of the autoionizing resonance is caused by the difference in quantum defect between the 5snl state and the 5pnl state [1]. The distinctive double peaked structure for the 5sns $^1D_2$ states is well documented [3].

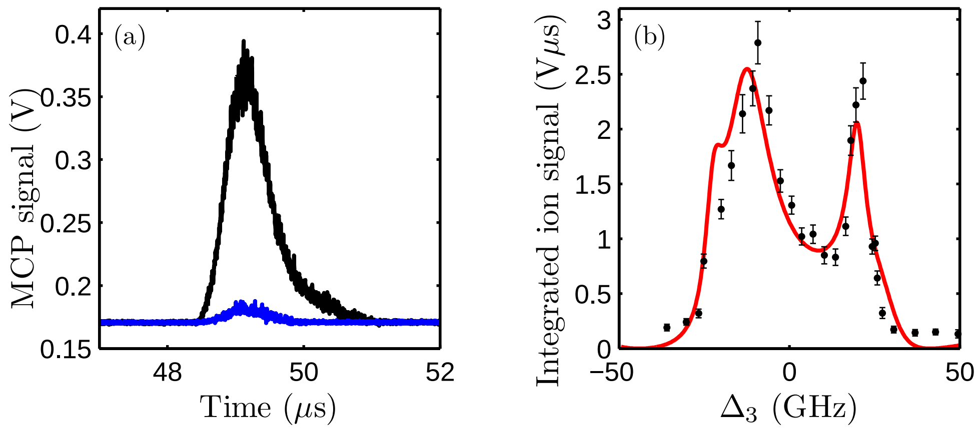

Figure 4.11: (a) The increase in ion signal due to autoionization. The blue line is spontaneous ionization signal and the black line is with the same Rydberg excitation parameters but with the autoionization laser. (b) The spectrum of the 5s56d $^1D_2 \rightarrow$ 5p56d $^1F_3$ autoionizing transition taken by stepping the frequency of the autoionizing laser. The detuning is relative to the bare ion transition. The red, solid line is a six channel multi-channel quantum defect theory fit [46].

For higher l Rydberg states ($3 < l < 9$) the wavefunction overlap between the electrons decreases and hence the autoionization rate decreases. The change in quantum defect with l changes the resonance shape and has been used to study population transfer to nearby states via plasma formation [46, 48]. For Rydberg states with $l > 9$ the spontaneous decay rate of the inner electron dominates over the autoionization process and the doubly excited atom is quasi-stable for the $5\mathrm{p}_{3/2}nl \rightarrow 5\mathrm{s}_{1/2}nl$ transition lifetime [130]. The majority of experiments in this thesis are on $l = 2$ states, the only exception being figure 4.14, which is an $l = 0$ state. Therefore, the rapid autoionization regime is the valid one.

Rydberg atoms can be photoionized relatively easily as they are very close to the ionization continuum. However, because autoionization is a resonant transition the ratio of the probability of excitation to an autoionizing state relative to photoionization is $\sim 10^8$ for states of interest in this thesis [131]. Autoionization therefore requires much lower laser intensity than photoionization, which is easier to achieve in the laboratory.

4.4 Spontaneous ionization of Rydberg atoms

Rydberg atoms are very close to the ionization limit and therefore require only a small amount of energy to become ionized. Uncontrolled ionization is referred to as spontaneous ionization, as opposed to driven ionization, e.g. field ionization [3], or autoionization. Spontaneous ionization has many causes and is seen in virtually every cold Rydberg experiment where ions/electrons are detected.

Rydberg states are closely spaced in energy and therefore transitions between them are at low frequencies which can easily be driven by blackbody radiation (BBR) [132]. Rydberg atoms can be directly ionized by BBR or population can be redistributed to other Rydberg states prior to photoionization [133]. Theoretical calculations of BBR photoionization indicate the ionization due to BBR should occur on time scales of several tens of microseconds, i.e.

slower than our experimental time scales.

Long-range, attractive, van der Waals (vdW) interactions between Rydberg states can cause Rydberg atoms to be accelerated toward each other and ionize via Penning ionization [134]. The time scale involved for the attractive vdW mediated Penning ionization mechanism is ≈ 1 μs [134] and could therefore explain some of the ionization in our experiment. However, the vdW interactions of 5s*n*d $^1\mathrm{D}_2$ Rydberg states are repulsive in strontium [50] meaning the Rydberg atoms would repel each other. 5s*n*d $^1\mathrm{D}_2$ states being transferred to states with attractive potentials (such as 5s*n*s $^1\mathrm{S}_0$ states in strontium [50]) via BBR or l-changing collisions with electrons [135] allow the possibility of ionization [136]. Due to the BBR requirement or the presence of free electrons the rate of ionization is lower, of the order of several microseconds.

Collisions between hot and cold Rydberg atoms are a further cause of ionization [137, 138]. In this scenario the hot (several hundred Kelvin) Rydberg atoms collides with cold ($\sim$ mK) Rydberg atoms and one of the Rydberg atoms ionize. The origin of the hot Rydberg atoms is the thermal atom beam which is constantly traveling through the cold atom ensemble. A small fraction of these hot atoms will be resonant with excitation beams and will be excited to Rydberg states. The time scale for these collisions is of the order of microseconds due to the velocity of the hot atoms and the average inter-particle spacing.

Ground state atoms in the thermal beam can also ionize the cold Rydberg atoms, however, the collision cross section scales as n^2 and therefore the probability of these collision is much lower than for hot Rydberg atoms.

As the Rydberg atoms are cold when they ionize the resultant ion is also cold ($\sim$ mK). Due to the imbalance in mass between the electron and the ion the electron takes most of the liberated binding energy away. If a large amount of spontaneous ionization occurs, the net positive charge of the ions that are left can bind further ionized electrons to form a plasma [137–139]. In these cold plasmas the electrons oscillate through the potential causing l-changing collisions [48, 135]. Electron collisions with Rydberg atoms cause further ionization via field ionization, and rapidly the Rydberg ensemble ionizes.

Spontaneous ionization can be used to study Rydberg physics, but there are several problems with doing so: the ions are not created at a well controlled time; nor are the amount of ions detected necessarily proportional to the number of Rydberg atoms. In our experiment, we have seen spontaneous ionization at different n, from 18-120, and at very different densities. The very different regimes in which spontaneous ionization has been seen indicates that the spontaneous ionization signal measured is almost certainly due to a mixture of all the above mentioned reasons as none of them have dominant time scales/probabilities.

For the experiments in this thesis spontaneous ionization is undesirable, especially when looking at spatial distributions, section 5.5. By having quite low Rydberg excitation probabilities, or by having only few atoms being excited, spontaneous ionization can be kept quite small.

4.5 Coherent excitation of the 5s56d ^{1}D$_2$ state

The methods by which the strontium atoms are cooled and trapped, and the Rydberg atoms detected have been discussed, now the excitation scheme to create the cold Rydberg atoms will be described.

The beam layout for the excitation lasers can be seen in figure 4.2. The probe (λ_1) and coupling (λ_2) lasers are counter-propagating to reduce Doppler broadening of the spectrum due to the temperature of the ensemble [80]. At 5.5 mK the residual Doppler broadening for a co-propagating pair of beams at 461 nm and 413 nm is $\approx$ 9 MHz, whereas for a counter-propagating pair the residual Doppler broadening is $\approx$ 0.5 MHz. The probe laser is delivered to the vacuum chamber via a single mode polarization maintaining fiber (*Thorlabs P1-405PM-FC*), collimated using a fiber collimator (*Schäfter + Kirchhoff 60FC-4-M12-01*). The Gaussian waist of the probe beam after the collimator is 1.07 ± 0.02 mm in both directions. For the experiments in this chapter the coupling beam is straight from the laser and has a Gaussian profile of 1.03 ± 0.02 mm by 0.78 ± 0.02 mm waists, parallel and perpendicular to the bench respectively. In chapter 5 the coupling laser beam is focused. The autoionizing laser (λ_3) beam is orthogonal to the two excitation lasers and is vertically polarized relative to the bench. The laser light for the autoionizing transition is supplied by a home-built Littrow configuration wavelength-selected diode (*Sanyo DL-7146-101S*). For the experiments in this thesis on the 5s56d $^1D_2$ state the autoionizing laser's frequency is set to give the maximum probability of autoionization, i.e. a detuning of -10 GHz on figure 4.11b.

The timing diagram for the MOT loading, excitation pulses and charge extraction and detection is shown in figure 4.12. The MOT is loaded for approximately 50 ms. A photodiode collects fluorescence from the MOT and when the signal reaches a set level the experiment is triggered. Triggering from the MOT fluorescence should reduce some of the shot-to-shot atom number/density fluctuations. The slowing and trapping light is extinguished and the quadrupole magnetic field turned off. A camera image is taken with a 64 μs exposure of MOT light in order to attain the ground state spatial distribution. The excitation beams are pulsed on simultaneously for 1 μs using acousto-optic modulators (AOMs). The excitation pulse transfers population from the ground state to the Rydberg state. The autoionizing laser is pulsed on for 1 μs, 100 ns after the excitation beams are extinguished and ionizes the Rydberg atoms.

In previous experiments with this cold atom setup spectra have been measured using the "step-scan" technique [46–48]. The coupling laser could not

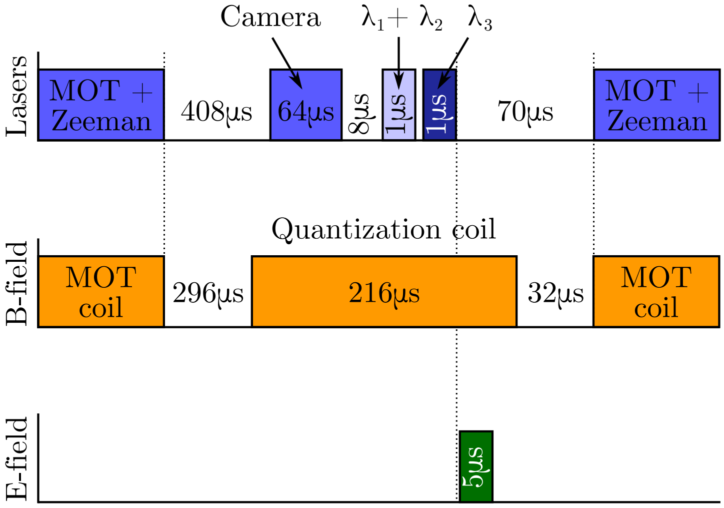

Figure 4.12: Timing diagram for a typical experimental sequence. The delays and pulse lengths are shown in the figure or described in the text if varied. A 64 μs pulse of MOT light is used for fluorescence imaging for obtaining the atom number and density of the ground state. The probe (λ_1) and coupling (λ_2) lasers are pulsed on simultaneously. The autoionizing laser (λ_3) is pulsed on 100 ns after the excitation beams. The electric field to direct the ions towards the MCP is pulsed on 100 ns after the autoionizing laser light is extinguished.

be locked on resonance so instead it was stepped over resonance and its wavelength measured on wavemeter, with the probe frequency held at a constant value. An example of a spectrum taken using "step-scan" method is shown in figure 4.13a. The transition being probed is $5s^2\ {}^1S_0 \rightarrow 5s5p\ {}^1P_1 \rightarrow 5s56d\ {}^1D_2$, shown as the lower two transitions in figure 4.10. The fitted Gaussian full width half maximum (FWHM) is 40.5 ± 0.4 MHz due to power broadening of the $5s^2\ {}^1S_0 \rightarrow 5s5p\ {}^1P_1$ transition.

With the frequency stabilized coupling laser from section 3.4.2 a new method of taking spectra becomes available. The probe laser frequency is stepped and the ion signal (either averaged or counted) is collected at each frequency. The frequency of the probe beam is controlled via a voltage applied to the probe AOM driver. The voltage is set within the *LabVIEW* program. Due to the power variations with the set frequency in the AOM, the power at each frequency is also controlled via *LabVIEW* to be constant across a scan. The statistical frequency error bars are very small as the AOM driver has very accurate frequency control, of the order of 10 kHz. An example spectrum using the probe stepping technique is shown in 4.13b. For comparison with the "step-scan" technique the transition being probed is the $5s^2\ {}^1S_0 \rightarrow 5s5p\ {}^1P_1 \rightarrow 5s56d\ {}^1D_2$ again. The fitted Gaussian FWHM is 3.7 ± 0.2 MHz. The measured width of the transition being narrower than intermediate state linewidth is indicative of coherent population trapping (CPT). Discussion of the width of the spectrum will occur in section 4.6. For the rest of the experiments in this thesis spectra were taken by scanning the probe frequency. Spectra in this thesis are fit with a Gaussian profile to extract amplitude, width, and centre position information. The profile should be Lorentzian though a Gaussian profile has always been found to fit better. The actual profile can be more complex, being a function of excitation powers, as discussed in section 5.3

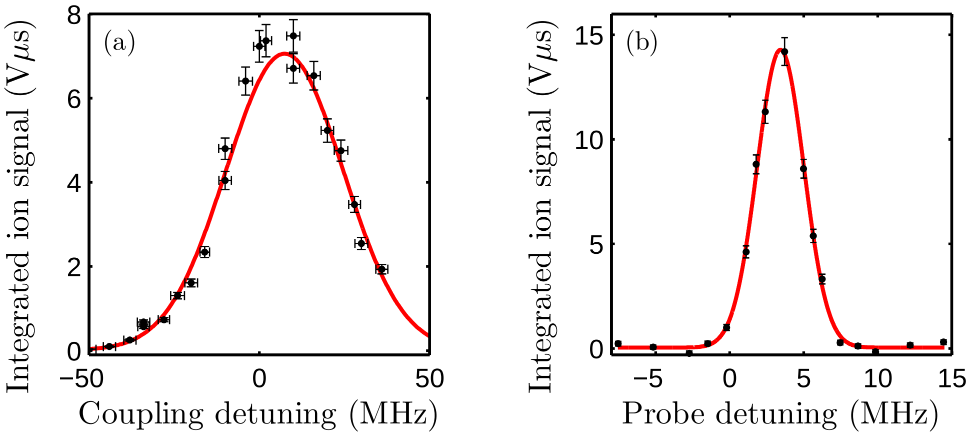

Figure 4.13: (a) Rydberg spectrum taken using the "step-scan" technique [46, 47], by varying the coupling laser frequency. (b) Rydberg spectrum using a locked coupling laser and stepping the frequency of the probe laser. Red, solid lines are Gaussian fits.

4.5.1 5s57s $^1S_0$ state spectroscopy

As discussed in section 2.1.1, the interaction sign for the 5sns $^1S_0$ series is opposite to the 5snd $^1D_2$ series. Different signs of interaction lead to different accessible physics [32].

The closest 5sns $^1S_0$ state to 5s56d $^1D_2$ state is the 5s57s $^1S_0$ state, the cold atom spectrum for which is shown in figure 4.14. The ion counting method is used here and shows that we can measure very small signals with good signal-to-noise. The very small locking signal for 5sns $^1S_0$ states, see figure 3.16, means the lock is less tight so the spectrum is broader. The fitted FWHM is 9 ± 0.3 MHz. For similar laser parameters to the 5s56d $^1D_2$ spectra the signal is much smaller due to the lower coupling strength. The average oscillator strength is lower by a factor of five due to the ratio of the degeneracies of the magnetic sub-levels [108]. To get a larger coupling strength, and therefore a larger, narrower feature a lower n state would have to be used. The C_6 coefficients scale strongly with n, hence, the likelihood of seeing interactions are much reduced compared to the 5snd $^1D_2$ states. For the rest of the experiments in this thesis only 5snd $^1D_2$ states are used.

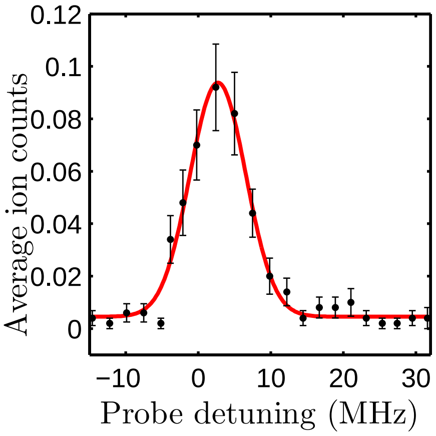

Figure 4.14: Spectrum of the 5s57s $^1S_0$ state. The red, solid line is a Gaussian fit.

4.6 Variation of spectra with excitation laser power

With the ability to coherently excite a cold cloud of strontium atoms to Rydberg states a simulation to model the dynamics is desirable. The simulation, based upon the optical Bloch equations described in section 2.2.1, was written in the *MATLAB* programming environment. The aim is to simulate the observed spectral features (amplitude, width, detuning) using the model. The free parameters are the laser linewidths, and the detuning of the coupling laser. The amplitude has a further free parameter to scale the calculated Rydberg population to the measured signal to account for collector efficiency and ground state atom number. When looking for the dipole blockade the dynamics change from the non-blockaded regime; having a model which fits the non-blockaded regime will aid in identifying when the interactions become prevalent.

4.6.1 Probe laser power

The variation in spectrum amplitude as a function of probe power is shown in figure 4.15a. The data points are the fitted Gaussian amplitudes to the spectra.

The FWHM of the measured and calculated spectra are shown in figure 4.15b. The requirement of the calculated spectra FWHM having to fit the measured FWHM as well as the amplitude trend added another constraint to the simulation.

The error bars on both the amplitude and FWHM come from fitting the spectra with a Gaussian using a weighted least-squares routine to find χ^2_{min} and then increasing one parameter while minimizing the others until $\chi^2 = \chi^2_{\mathrm{min}} + 1$ [140]. The error bars are therefore one standard deviation.

The simulation results clearly fit the data quite well, indicating that the OBE simulation used models the experiment well. The laser linewidths from the simulation are $\gamma_{\rm p} = 1.0$ MHz and $\gamma_{\rm c} = 1.2$ MHz. The free running linewidths of the frequency-doubled lasers (from the manual) are ≈ 1 MHz. The laser locking circuits for the probe and coupling lasers have a feedback bandwidth of ~ 10 kHz and 30 Hz respectively implying that the locked laser linewidth should not be radically different to the free running linewidth, which they are not. The measured FWHM increases with probe power due to power broadening and is well predicted by the simulation. The minimum measured width is almost certainly set by the laser linewidths as the linewidth of the state is $2\,\pi \times 6.4$ kHz and the Doppler broadening is ~ 500 kHz.

The required detuning of the coupling laser from the simulation is 40 MHz ($1.25\Gamma_{\rm e}$). As we believed the probe and coupling lasers were on resonance, the simulated detuning seemed quite large. From the simulation it was discovered that the sign of feedback in the locking circuit was incorrectly set and the coupling laser was therefore locked to the wrong slope, figure 3.13, and hence was ≈ 40 MHz detuned.

4.6.2 Coupling laser power

To check the simulation further, the variation of amplitude, figure 4.16a, and FWHM, figure 4.16b, of spectra with varying coupling laser power was investigated. Again the simulated amplitude values have a free scaling parameter.

The OBE simulation fits the data points quite well with the coupling detuning being 40 MHz as before, due to the lock signal error, and the laser linewidths are $\gamma_{\rm p} = 1.1$ MHz and $\gamma_{\rm c} = 1.35$ MHz, which are very similar to the previous simulation.

As the simulation fits both data sets, varying the probe and coupling laser powers, quite well there is ample evidence that the OBE simulation can

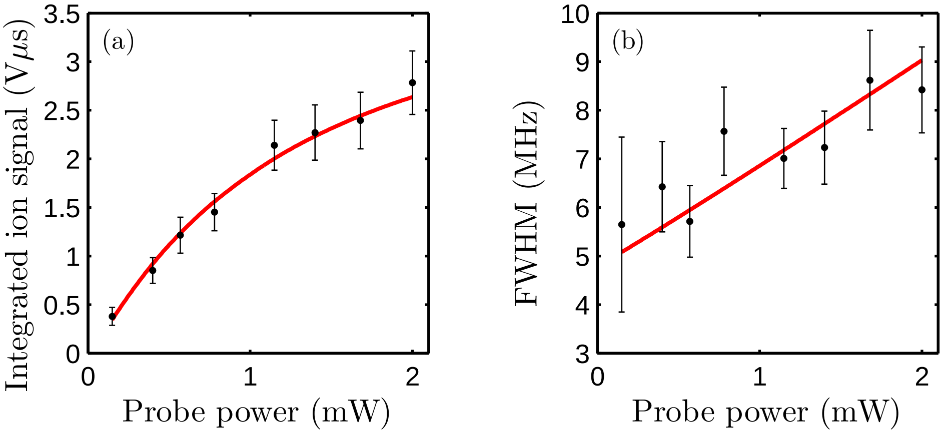

Figure 4.15: (a) The maximum amplitude of the CPT spectrum as a function of probe power. The red, solid line is the OBE simulation described in the text with a free scaling parameter. (b) The FWHM of the CPT spectrum as a function of probe power. The red, solid line is from the OBE simulation. The coupling laser power for these spectra was 5 mW.

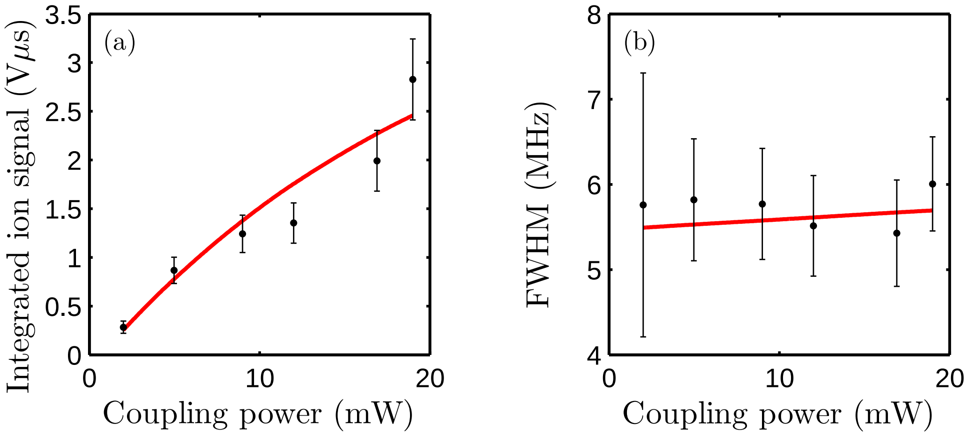

Figure 4.16: (a) The maximum amplitude of the CPT spectrum as a function of coupling power. The red, solid line is an OBE simulation described in the text with a free scaling parameter. (b) The FWHM of the CPT spectrum as a function of coupling power. The red, solid line is from the OBE simulation. The probe power for these spectra was 120 μW.

model our experimental conditions. In chapter 5 the simulation is used to calculate the detector efficiency of our system, section 5.2, and is extended to investigate changes to the spectra due to focusing of the coupling laser, section 5.3.

4.7 Effect of magnetic and electric fields on spectra

Magnetic and electric fields perturb the energy levels of the bare atom. In this section spectra will be taken using the probe scanning technique to show the effect of these external fields.

4.7.1 Zeeman effect

The Zeeman effect shifts the energy levels of an atom by coupling to a magnetic field

$$\mathscr{H} = \mathscr{H}_{\mathrm{A}} + \mathscr{H}_{\mathrm{Zeeman}} \ , \tag{4.2}$$

where $\mathscr{H}$ is the total Hamiltonian of the system, $\mathscr{H}_{\mathrm{A}}$ is the bare atom Hamiltonian, and $\mathscr{H}_{\mathrm{Zeeman}}$ is the perturbation due to the Zeeman effect. The weak-field Zeeman effect [99], where the splitting due to the magnetic field ($\sim$ 10 MHz) is much less than energy difference between nearby states ($\sim$ GHz), is given by

$$\mathscr{H}_{\mathrm{Zeeman}} = -\vec{\mu} \cdot \vec{B} = g_{\mathrm{J}} \mu_{\mathrm{B}} J_z B_z \ , \tag{4.3}$$

where $\vec{\mu}$ is the magnetic moment of the atom, $\vec{B}$ is the magnetic field vector, g_{J} is the Landé g-factor, equal to 1 for singlet transitions, μ_{B} is the Bohr magneton, J_z is the z-component of the total angular momentum, given by $m_{\mathrm{J}}\hbar$, and B_z is the magnetic field in the z-axis. Hence the weak-field Zeeman effect along the magnetic field splits the degenerate m_{J} components of an atomic state from the unperturbed atom according to

$$\Delta \mathrm{E}_{\mathrm{Zeeman}} = -\mathrm{g}_{\mathrm{J}} \mathrm{m}_{\mathrm{J}} \mu_{\mathrm{B}} \mathrm{B}_{\mathrm{z}} \ . \tag{4.4}$$

To resolve the $m_{\mathrm{J}} = +2$ and the $m_{\mathrm{J}} = 0$ states in the spectra, the splitting must be greater than the half width half maximum (HWHM). For incoherently excited spectra, the narrowest possible linewidth is the intermediate state linewidth, 32 MHz, corresponding to a magnetic field of approximately 6 G. Whereas, for a CPT spectrum, like that in figure 4.13b, fields of about 1 G are required. The narrowness of the features makes perturbations to the spectrum much easier to observe.

MOT magnetic field decay

The circuit which controls the MOT trapping magnetic field, figure A.4, is an integrator circuit that measures the voltage drop across a sense resistor in series with the MOT coils. The circuit therefore sets the current through the coils accurately, reducing current fluctuations allowing stable MOT operation. However, the decay time for the current out of the coils (and therefore the magnetic field created) is correspondingly quite slow, $1/e$ lifetime $\sim$ 150 μs. The excitation time period in our experiment is fast (1 μs) relative to the decay time of the field, meaning we can take spectra at specific times during the decay. Figure 4.17 shows spectra taken with different delays between the MOT coil being switched off and the excitation pulses occurring. The red lines are a double Gaussian fit for (a)-(c) and a single Gaussian fit for (d).

The spectrum clearly evolves from doubly peaked to singly peaked in a time comparable to the magnetic field decay time, indicating that with coherent excitation we are sensitive to the MOT field. Previously we could not resolve the Zeeman splitting of the spectrum due to the MOT field, see figure 4.13a.

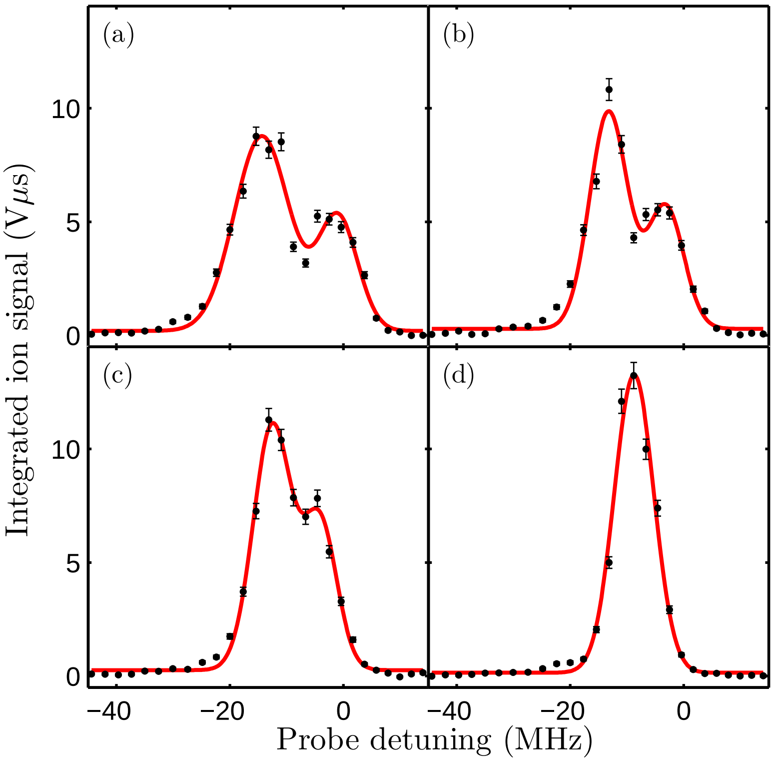

Figure 4.17: The CPT spectrum as a function of time after the magnetic quadrupole field is switched off (a) 88 μs, (b) 144 μs, (c) 184 μs, (d) 400 μs. The solid red line in (a)-(c) is a two Gaussian fit, whereas in (d) only a single Gaussian fit is applied.

Due to the unknown direction of the magnetic field relative to the direction of the excitation beams the polarization is not well defined, therefore the transitions driven ($\sigma^+/\sigma^-/\pi$) are also unknown.

As we wish to control which m_J state we populate we need to wait for the MOT magnetic field to decay before we apply a quantization field along the excitation beams. From figure 4.17 it is clear that the MOT field has decayed to a level below our spectroscopic resolution after 400 μs. The rest of the experiments in this thesis are done with a delay time of 400 μs before the camera image is taken.

Magnetic quantization field

To selectively excite specific m_J states a defined quantization direction is required [60]. To create a quantization axis, a magnetic field along the axis of the excitation beams is used. The magnetic field amplitude needs to be large enough to split the m_J states by approximately the FWHM of the spectroscopic resolution to ensure that as small as possible population is transferred to the incorrect state. A further constraint for our setup is that the field needs to switch on fast enough such that the cold atom cloud does not expand too much. Expansion of the cloud causes the density to decrease which makes investigating the dipole blockade more difficult. The quantization field therefore had to switch on in the time taken for the MOT field to decay and the camera image being taken, i.e. 480 μs.

Due to the shape of the vacuum chamber only a single coil can be placed close enough to the cold atoms to create enough magnetic field and have a short enough switching time. The position of the quantization coil is shown in figure 4.2. The coil generates a magnetic field of 3 ± 0.2 G at the position of the atoms, based on the number of turns, applied current, and uncertainty in distance from atomic ensemble.

To test the switching speed of the quantization field, spectra are taken with and without the quantization field on for several switching times of the field. Figure 4.18a shows two spectra, with (black circles, with red, solid line fit) and without (blue squares, with green, dashed line fit) the quantization field applied. The fits are single Gaussian fits. The quantization field clearly shifts the resonance enough to selectively excite it.

Figure 4.18b shows the difference between the fitted centres of the Gaussian fits with and without the quantization field applied. The field quickly turns on (≈ 50 μs) and stays at a constant value.

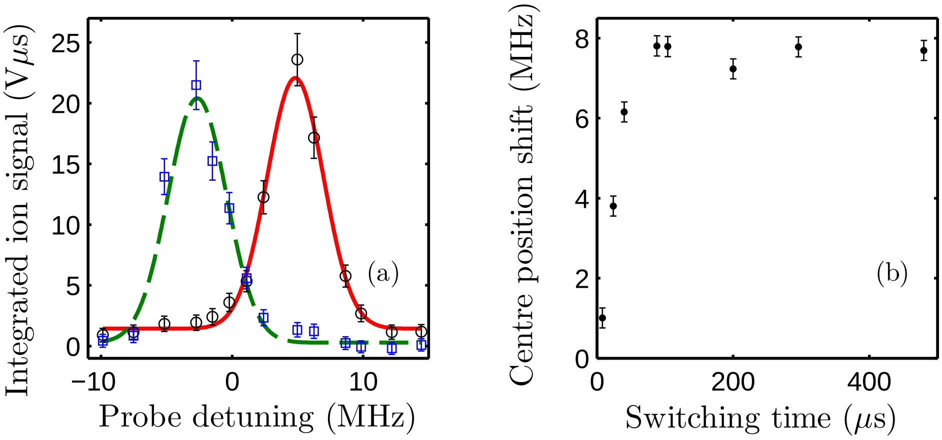

Figure 4.18: (a) The effect of the quantization coil on the CPT spectrum. The blue squares with a green, dashed line are a spectrum without the quantization field applied. The black circles with red, solid line fit are with the quantization field applied. The fits are a Gaussian in both cases. (b) The fitted centre position shift as a function of quantization coil switch on time.

The direction of the magnetic field relative to the excitation beams means only σ^+ or σ^- polarization light is defined. Of the five sub-levels of singlet d states only three can be accessed, the $m_J = 0, \pm 2$, see figure 4.19a. The stretched states $m_J = \pm 2$ have the strongest excitation probability therefore the inability to populate the $m_J = \pm 1$ is not a problem as we do not wish to excite them. Figure 4.19b shows the spectra of the two stretched states. The stretched state splitting is given by equation 4.4. For the applied field the splitting should be 17 ± 1 MHz, in good agreement with the measured, fitted centre-to-centre splitting of 16.2 ± 0.3 MHz. The $m_{\rm J} = 0$ feature is slightly larger than the $m_{\rm J} = +2$ feature, implying there is a small stray magnetic or electric field in the MOT region or a birefringence in one or both of the excitation beams causing the coupling to the $m_{\rm J} = +2$ state to be decreased.

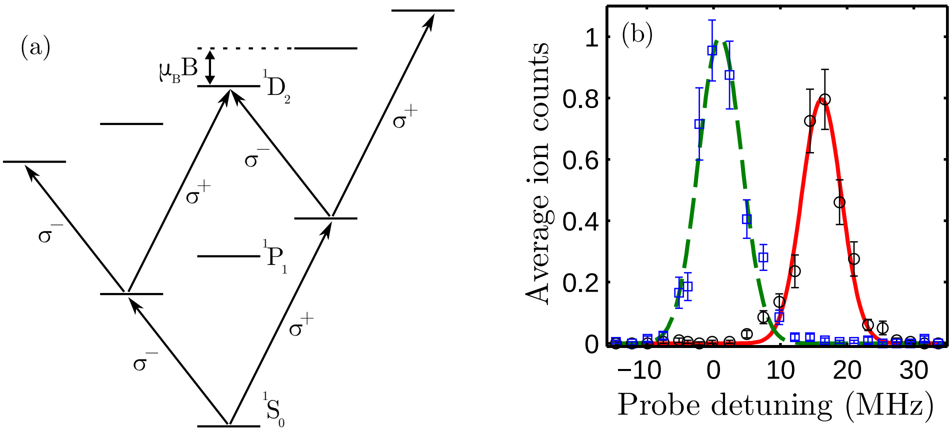

Figure 4.19: (a) The Zeeman splitting of the magnetic sub-levels for a d state. The excitation routes allowed by circularly polarized light show which $m_{\rm J}$ states are accessible. (b) The CPT spectra with the quantization coil on addressing the stretched states. Blue squares with the green, dashed line fit are for $\sigma^-\sigma^-$, and black circles with red, solid line fit are for $\sigma^+\sigma^+$ polarizations of the probe and coupling lasers.

4.7.2 Stark effect

Atoms couple to electric fields in a process called the Stark effect [65].

$$\mathscr{H} = \mathscr{H}_{\rm A} + \mathscr{H}_{\rm Stark} \; . \tag{4.5}$$

The electric field serves to shift the position of spectral lines. In low electric field the shift in state position due to the electric field is $\Delta {\rm E} = -1/2\alpha_0 E^2$, where α_0 is the scalar polarizability of a specific $|nlJm_{\rm J}\rangle$ state, and E^2 is the square of the electric field [65]. Rydberg states couple very strongly to electric fields as the polarizability scales as n^7 [3]. Rydberg states are therefore ideal to study the Stark effect as the energy shift of the states can be large for moderate sized electric fields. The polarizabilities for the m_J components without an applied magnetic field can be calculated using a single electron moving in a model potential approximation [51, 52], see section 2.1. We have previously shown that the single electron model gives very good agreement with measured Stark maps [47] up to electric fields where the higher angular momentum manifold overlaps with the measured spectrum. In these experiments we did not have control over the specific m_J components. With the ability to investigate specific m_J states and narrow resonances we can further certify that the single electron model works at low electric field strengths.

As we have the magnetic quantization field applied the Hamiltonian for the system is now

$$\mathscr{H} = \mathscr{H}_\mathrm{A} + \mathscr{H}_\mathrm{Zeeman} + \mathscr{H}_\mathrm{Stark} \ , \tag{4.6}$$

where we have added the Zeeman and Stark shifts independently to the bare atomic energies. The magnetic and electric fields are orthogonal to each other, however, meaning that the $|J, m_\mathrm{J}\rangle$ basis is not the same between the two fields. For convenience we choose to work in the Zeeman basis, meaning the Zeeman shift is that stated in equation 4.4. To calculate the correct Stark shift we have to decompose the Stark basis into the Zeeman basis. The decomposition can be represented as a rotation of bases, using the Wigner D-matrix [141]

$$\mathfrak{D}^J_{m'm}(\alpha, \beta, \gamma) = e^{-i\alpha m'} d^J_{m'm}(\beta) e^{-i\gamma m} \ , \tag{4.7}$$

where J is total angular momentum of the state, m' is the decomposed projection in the rotated basis, m is the projection in the original basis,

α, β, and γ are the Euler rotation angles [141], and $d^J_{m'm}$ is the reduced rotation matrix

$$\begin{aligned} d^J_{m'm}(\beta) =& \sqrt{(J+m')!(J-m')!(J+m)!(J-m)!} \times \\ & \sum_s \frac{(-1)^{m'-m+s}(\cos\frac{\beta}{2})^{2J+m-m'-2s}(\sin\frac{\beta}{2})^{m'-m+2s}}{s!(J+m-s)!(m'-m+s)!(J-m'-s)!} \ , \end{aligned} \tag{4.8}$$

where the summation s is over all values for which the factorials exist. Equations 4.7 and 4.8 calculate the proportion of state m' in state m when the basis is rotated by angles α, β, and γ. For the setup in our experiment where the magnetic and electric fields are orthogonal, $\alpha = \gamma = 0°$, and $\beta = 90°$. The total Zeeman and Stark shift is therefore given by

$$\Delta_{\mathrm{Total}}(m_{\mathrm{J}}) = -m_{\mathrm{J}}\mu_{\mathrm{B}}B - \frac{1}{2}\sum_{m'_{\mathrm{J}}} d^J_{m'_{\mathrm{J}}m_{\mathrm{J}}}(\beta)\alpha_0(|m'_{\mathrm{J}}|)E^2 \ , \tag{4.9}$$

where the summation over m'_{J} is over all possible magnetic sub-levels. The Stark shift component is the linear sum of the shift of all magnetic sub-levels multiplied by their mixing proportion multiplied by the square of the electric field, E^2.

Figure 4.20a shows the electrode setup for taking a Stark map. Electric field calculations indicate the electric field across the MOT region is constant to better than 2 %. The electrode pairs B and D are grounded except during the excitation beam pulses when they are pulsed low/high. The applied field is controlled by an arbitrary waveform generator (*Tektronix AFG 3022b*). Electrode pair A is pulsed high after the autoionizing beam to direct ions toward the MCP. Electrode pair C is always at ground.

A spectrum taken with 38 mV cm^{-1} applied electric field is shown in figure 4.20b. The solid red line is a three Gaussian fit to account for the three m_{J} components that can be excited. The excitation beams are set to excite the $m_{\mathrm{J}} = +2$ component in zero electric field. However, there are three components seen due to slight birefringence in the viewports causing slight rotation of the polarization.

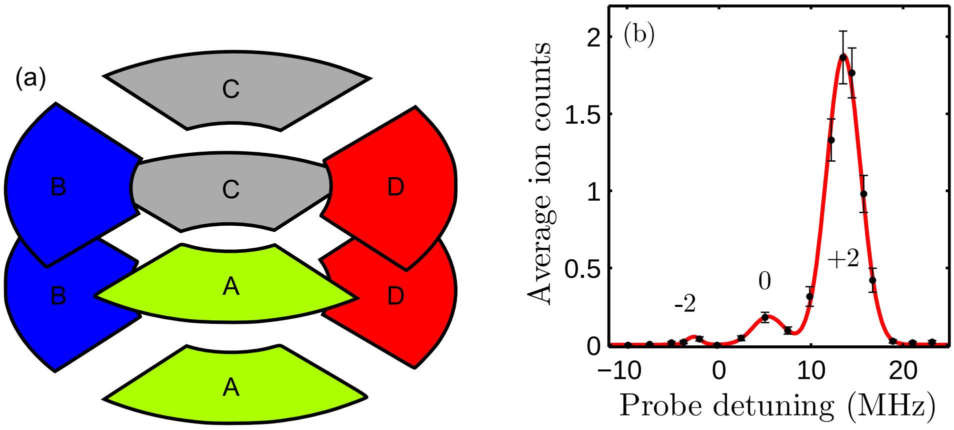

Figure 4.20: (a) The electrode geometry for taking a Stark map. Pairs B and D are used to create the linear electric field. Pairs A and C are used to direct ions towards the MCP. (b) A CPT spectrum with the quantization field applied, a small stray magnetic field component causes the polarization to be not perfectly aligned along the quantization field. The peaks are assigned their zero electric field m_J values. The solid red line is a three Gaussian fit. The centre positions of the $m_\mathrm{J} = +2$ and $m_\mathrm{J} = 0$ states as a function of field are shown in figure 4.21b.

The Stark map for the 5s56d $^1D_2$ state is shown in figure 4.21a. The applied electric field is the electric field created by electrode pair B and D from figure 4.20a. The applied electric field is calibrated from the centre position shifts of figure 4.21b. The shift with electric field is calculated from equation 4.9, the calibration from applied voltage to applied electric field is obtained from fitting the data to these shifts. A stray field and frequency offset are also incorporated. Both shifts are fit with the same calibration factors. The electric field calibration is 0.38 ± 0.01 V cm^{-1} per applied Volt in the MOT region. Previously the calibration factor when fitting the shift to larger applied fields was measured to be 0.42 ± 0.01 V cm^{-1} per applied Volt in the MOT region [47]. The difference between these two calibrations could be due to a different set of electrodes being used. The stray electric field is

33 ± 1 mV cm^{-1}. The stray field is larger than previously measured [46]. The larger stray field is probably due to the pulse generator ground being slightly different to the chamber ground, causing a small electric field.

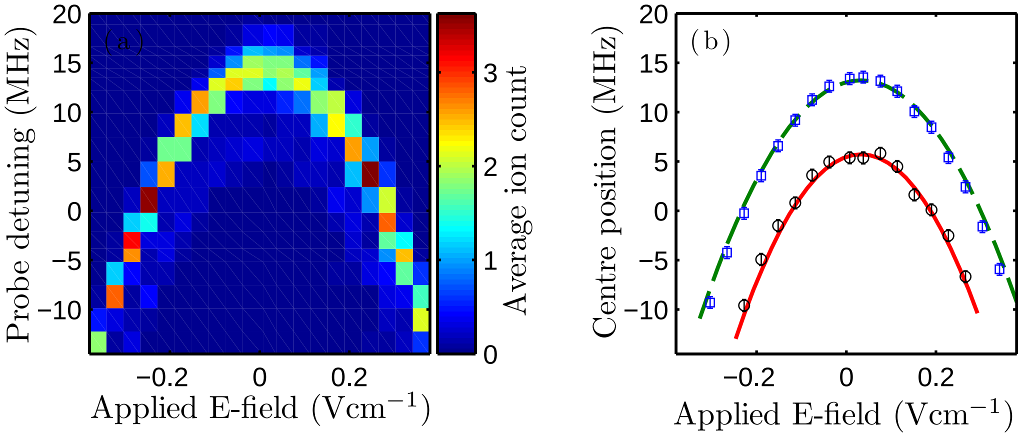

Figure 4.21: (a) A Stark map of the 5s56d $^1D_2$ state with an applied electric and magnetic field. (b) The fitted centre positions of the $m_J = 0$ (black circles) and the $m_J = +2$ (blue squares) states with applied E-field. The red, solid line ($m_J = 0$) and green, dashed line ($m_J = +2$) are the solutions of equation 4.9 with a stray field and frequency offset.

Conclusion

We have a reliable apparatus for creating a few million cold, trapped strontium atoms. A proportion of these atoms can be coherently excited to Rydberg states. The divalent nature of strontium atoms allows access to a resonant ionization mechanism called autoionization, allowing temporal control of the ionization of Rydberg atoms. As we can count individual ions with our experimental setup regimes of very small signal are available to us. In the next chapter we will use this counting ability to look at the statistical distribution of ions.

Using a magnetic quantization field we can excite specific m_J states by controlling the polarization of the light.

A simulation using the optical Bloch equations models the excitation dynamics of our experiment very well, indicating a two-photon excitation FWHM linewidth of 3.7 ± 0.2 MHz for the 5s56d $^1D_2$ state. The OBE simulation will be used in the next chapter to calculate the detection efficiency of Rydberg atoms in our experiment.

Applying a weak orthogonal electric field and fitting the shift positions of two m_J states gives further evidence that a single electron model for calculating wavefunctions [46, 50] is correct.

The measured spectra indicate we can control the applied magnetic and electric fields accurately. In the next chapter the autoionizing beam will be focused down to a small spot and translated across the Rydberg ensemble to extract spatial information of the Rydberg distribution.

Chapter 5

Spatial distributions of Rydberg atoms

In the previous chapter the apparatus required to create a cold atomic sample of strontium was described. The experimental technique and theoretical simulation of coherent population transfer from the trapped ground state to a Rydberg state was also explained, as was the process of autoionization used to ionize the Rydberg atoms. In this chapter, the information obtained by using the autoionization process will be extended to allow data on the Rydberg atoms' spatial distribution to be extracted as well, further details can be found in [142].

Measuring the ground state spatial distribution of a cold atom cloud is relatively straight-forward. Two widely-used techniques are fluorescence imaging, used in chapter 4, and absorption imaging. However, both these techniques require several scattering events of the transition, which cannot be realized for a Rydberg transition as multiple scattering events would change the population dynamics being probed. Absorption imaging has been used to measure the spatial distribution of an ultracold plasma [143]. Other groups have used, or plan to use, absorption imaging of the ground state with coupling lasers to the Rydberg state causing EIT to infer spatial distributions of the Rydberg state [34–37, 144]. Measuring EIT in the absorption image, however, inherently couples the process of Rydberg state preparation and detection, which makes the measurement of dynamical crystallization impossible.

State selective field ionization has been used to measure the Rydberg state spatial distribution directly [41]. Although field ionization decouples state preparation and detection, in order to get a high resolution (< 10 μm), a sharply pointed electrode must be held close to the atomic sample. An electrode close to the Rydberg ensemble creates problems with stray electric field due to the polarizability of Rydberg atoms. These groups obtain a spatial resolution of approximately 6 μm.

Recently, Rydberg crystals have been observed by exciting to the crystal state in a two-dimensional optical lattice, then transferring population back to the ground state and imaging that distribution with a high-numerical aperture imaging system [40].

To use autoionization as a spatial probe of the Rydberg population distribution, the autoionizing laser will be focused to a spot size of less than 10 μm and translated across the Rydberg ensemble. Figure 5.1 shows a simplified diagram of translating the focused autoionizing laser across the Rydberg ensemble. The measured ion signal due to autoionization is thus proportional to the Rydberg population at that spatial position. The proposed technique decouples Rydberg excitation and detection and does not suffer from the stray field issues of using field ionization.

To make spatial measurements a method of accurately moving a tightly focused spatial probing beam is needed. Two methods were proposed for moving the focused beam. One way is to change the angle of the input beam to the lens setup using a beam deflector to create a spatial movement at the focus. The other method is to attach a fiber to the lens setup and mount the lens system to a linear translation stage and translate the entire setup.

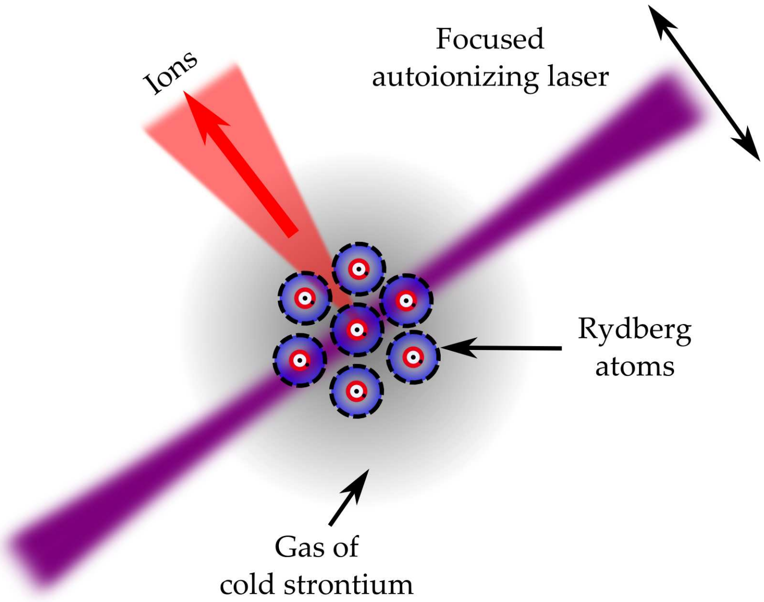

Figure 5.1: Diagram of how the spatial distribution measurement would be implemented. A tightly focused autoionizing laser is translated across the cold Rydberg ensemble and the ions collected.

The advantage of the beam deflection method is that it would be possible to translate the spatial probe across the ensemble very quickly. This would allow possible correlations in a single shot (one Rydberg excitation sequence) to be mapped out. However, to begin with, the beam deflection method may be very difficult to align onto the atoms through a complex lens setup. Furthermore, there may be some power variation with position as well as changes in spot size due to slight changes in the path length and aberrations through the lens setup.

The translation stage method would be easy to align as the lens setup could be attached to a mirror mount. The problems associated with power/spot size variations mentioned above would also be removed. Although, it would not be possible to scan across the ensemble in a single shot to look for correlations due to the translation velocity of the stage.

The translation stage method was chosen because of the ease of setting up and avoiding power fluctuations. As this is the first time the autoionization microscopy technique has been attempted simplicity was desired.

This chapter will:

- Describe the focusing lens system in section 5.1
- Detail the results obtained with a focused autoionizing laser in section 5.2
- Detail the effects of using a focused coupling beam in section 5.3
- Describe the translation stage and its accuracy in section 5.4
- Show the spatial distribution of the Rydberg state in section 5.5
- Describe the measured spatial distribution as a function of laser power in section 5.6

5.1 Lens design for the autoionizing beam

The desire to measure the spatial distribution with the maximum spatial resolution possible meant that the focused spot size had to be as small as possible, i.e. diffraction limited. The diffraction limit is defined by the Airy radius [145]

$$r_{\mathrm{Airy}} = 1.22 f\lambda/D \, , \tag{5.1}$$

where r_{Airy} is the distance from the beam centre to the first minimum, f is the focal length of the lens system, λ is the wavelength of light, and D is the diameter of the aperture of the imaging system. The Airy radius is defined for a uniformly illuminated beam the size of the aperture.

From equation 5.1 it is clear that the lens system needs to have a large aperture and be close to the sample, such that f is as small as possible. There have been several experiments that use either aspheric lenses, microscope objectives or complex multi-element lenses to get very small spot sizes ($\approx$ 1 μm) [38, 146–148]. These all require the lens(es) to be either inside the vacuum chamber or the optical access to the vacuum chamber to be very close to the interrogation sample. As we have a vacuum chamber already and a method of coherently exciting Rydberg atoms within it, these solutions were discarded.

The distance from the vacuum chamber viewport to the MOT is 158 mm; this distance sets the minimum f. The viewports have a clear aperture of approximately 30 mm due to the anti-reflection coating, hence setting the maximum diameter. Thus, the smallest possible r_{Airy} we can achieve is 2.6 μm.

Another consideration is the weight of the lens system; the lens system must be light enough to be accurately moved with a high precision translation stage. To limit the weight, optics with a diameter of 25.4 mm (1”) or less were used, further limiting D. It was also desirable to keep the lens system as short as possible as the system will only be supported at one end. Using high numerical aperture, custom lenses was also rejected due to cost.

For the setup described below a Gaussian intensity distribution is used, not a uniformly illuminated top hat function as described above, where the power, P through an aperture of radius $r = D/2$ is

$$P = P_0(1 - e^{-2r^2/w^2}) \ , \tag{5.2}$$

where P_0 is the total power and w is the $1/e^2$ width of the beam. For example, if the radius is equal to the width there is 86.5 % transmission due to truncation of the intensity distribution. Transmission is required to be as large as possible without impinging upon minimum waist size. To this end the maximum width of the Gaussian is set to be approximately half the aperture radius to allow $>$ 99 % transmission [149].

Given these constraints the optics design software *Zemax* was used to simulate the best possible multi-element lens setup. Unfortunately *Zemax* calculates the diffraction limit using a hard edged intensity distribution, whereas experimentally we measure the $1/e^2$ width of a smoothly varying intensity beam. At the focus the Airy radius and the Gaussian waist are related by $w = 0.75 r_{\mathrm{Airy}}$ [149] for a given aperture, hence the Airy radius is useful for simulations.

The chosen lens setup to create the smallest spot size is shown in figure 5.2a, with the elements described in table 5.1. The output of a FC-APC single mode polarization-maintaining optical fiber (*Thorlabs P3-405PM-FC-2*), collimated using a fiber collimator (*Thorlabs CFC-11X-A*) (element 1 in figure 5.2a), was used to create a Gaussian beam ideal for focusing to the diffraction limit and to reduce astigmatic effects of the laser beam straight from the diode. The focal length of this collimator is $f = +11$ mm leading to an output waist of 0.9 mm. Two $f = -30$ mm lenses (elements 2 and 3) are then used to increase the spot size in as short a distance as possible. A single $f = -15$ mm lens could not be used as they are highly aberrant at 408 nm. The aberrations are due to the higher refractive index glass normally used to make the shorter focal length lenses (E-BAF11/N-SF11) which also absorb a significant proportion of light at 408 nm. Glass types that have low aberrations/absorption at 408 nm, such as BK7/F2/N-FK5, were used instead. An achromatic doublet of $f = +75$ mm (element 4) is used to slightly focus the beam before an $f = +250$ mm lens (element 5) is used to do the majority of the focusing. All lenses are broadband anti-reflection coated from 400 - 700 nm. The final element shown (element 6) is the vacuum chamber viewport. The overall focal length from the final lens is calculated to be 197 mm.

Zemax simulations of the beam through its focus are shown in figure 5.2b. The calculated Airy radius comes from having a beam of 6.8 mm radius at

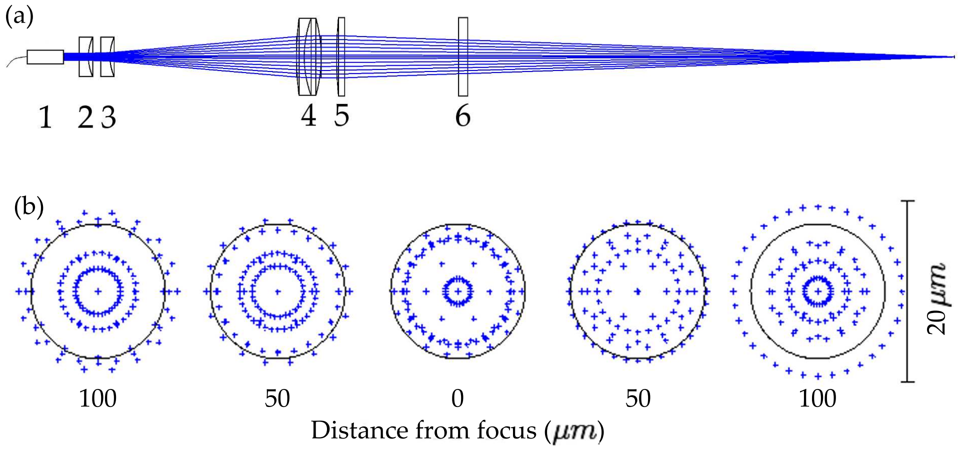

Figure 5.2: (a) Lens setup and ray tracing for the focusing of the autoionizing laser beam. Element descriptions can be found in table 5.1. Lengths are to scale. (b) Slices through the focus of the setup in (a) as calculated by *Zemax*. The black circle indicates the Airy radius of 7.5 μm. At the focus the rays are all inside the Airy radius, which indicates the focus is diffraction limited. Both figures were exported from *Zemax*.

the achromatic doublet, leading to a power transmission from equation 5.2 of > 99.9 %. At the focus of the beam, *Zemax* calculated the RMS radius to be 5.3 μm, and the geometric radius to be 7.1 μm. With both these values being smaller than the Airy radius means the setup can be considered diffraction limited.

The sensitivity of the lens setup to tilt and decentration of the optical elements in *Zemax* was investigated. For a reasonable error budget of tilt/decentration (a few degrees/tenths of a millimeter) there is no appreciable change to the waist size. To attain these constraints, the lenses are held inside an internally threaded one inch (*Thorlabs SM1*) lens tubing, limiting the allowable alignment error. The fiber collimator is attached via a fiber collimator adapter (*Thorlabs AD9.5F*). The half inch optics are held in mounting adapters (*Thorlabs SM1A6T*), which align the centre of the lenses with the lens tubing. The one inch optics are held in place by retaining rings. The threading of the lens tubing allows accurate separation of the optical elements.

Element	**Part number**	**Focal length (mm)**	**Material**	**Separation (mm)**
1	CFC-11X	11	BK7	0.0
2	LC1060-A	-30	BK7	3.0
3	LC1060-A	-30	BK7	4.0
4	NT65-978	75	F2/N-FK5	60.6
5	LA1461-A	250	BK7	5.0
6	Viewport	∞	Kodial	37.0

Table 5.1: Details of the lenses and their separations. Element 1 is an adjustable focus fiber collimator to provide a collimated Gaussian beam. All lenses are from *Thorlabs* except for the achromatic doublet (element 4), which is from *Edmund Optics*. Separation refers to the distance between the front face (furthest left in figure 5.2a) of that element and the back face (furthest right) of the previous element. The distance from the back face of the viewport to the focus is 158 mm, which is set by the vacuum chamber. Including the width of the lenses, the lens setup fits into four inch long lens tubing.

5.1.1 Width measurements

The width of the laser beam sent through the constructed lens setup was measured using a knife-edge technique. To take these knife-edge measurements the very accurate automatic translation stage described in section 5.4 was used. The results are shown in figure 5.3a. The error bars are the standard error from five repeat measurements and are $\approx 2-3$ %. The error on the position is set by the resolution of the manual translation stage which is 1 μm. The focal sizes/positions are fit using the Gaussian propagation

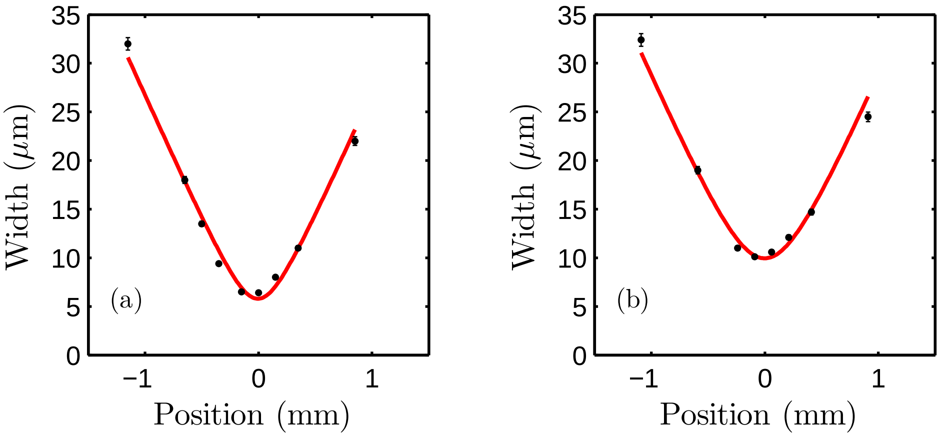

Figure 5.3: Beam width measurements of the focused 408 nm laser using the described lens system. The black dots are data points with the standard error from five repeats. The red, solid line is a fit using equation 5.3. (a) is without the viewport included. (b) is with the viewport. The width profiles are centred to have the waist at 0 mm.

formula

$$w(z) = w_0 \left(1 + \left[\frac{\lambda M^2 (z - z_0)}{\pi {w_0}^2}\right]^2\right)^{1/2} , \tag{5.3}$$

where $w(z)$ is the width at a position z along the laser beam, w_0 is the waist, λ is the wavelength, M^2 is the laser beam quality factor (indicative of the amount of higher order TEM modes mixed into the beam [150] - increasing minimum beam size), and z_0 is the position of the focus. The fit uses a weighted least-squares fitting routine.

The effect of including the vacuum chamber viewport (*LewVac DN40CF*, anti-reflection coated 400-700 nm) is shown in figure 5.3b. The fit parameters are detailed in table 5.2.

Without the viewport, the waist of 6.3 ± 0.1 μm is narrower than the Airy radius predicted due to the $1/e^2$ waist of a beam is measured using the knife-edge technique; this is three quarters the size of the Airy radius [149], which indicates a $1/e^2$ waist of 5.6 μm. The measured waist is slightly larger than

Viewport	**Waist (μm)**	$\boldsymbol{M^2}$	**Focal position (mm)**	**Relative position (mm)**
Absent	6.3	1.23	196.0	0.0
Present	9.8	2.08	198.9	2.9

Table 5.2: The beam propagation parameters for a laser at 408 nm with and without a viewport in the beam. Focal position is the position of the focus from the back of the final lens (element 5). Relative position is set so that the focused beam position without the viewport is zero.

three quarters the Airy radius most likely due to some aberrations introduced by the lenses. The M^2 value of 1.23 means the beam is quite Gaussian (an M^2 of exactly 1 indicates a perfect Gaussian beam), but not perfect, most likely due to the lenses introducing some aberrations. The M^2 value increases the waist of a purely TEM_{00} beam by M^2, suggesting a minimum beam waist of 5.2 μm, which is in quite close agreement with the diffraction limit mentioned above. The M^2 of low power, single mode diode lasers is typically between 1.1 and 1.7 [151], whereas the M^2 of a single mode optical fiber is 1.0 as only the TEM_{00} mode is allowed to propagate [151]. The measured M^2 value also lends evidence to the supposition that the waist is slightly larger than it should be due to aberrations. *Zemax* simulations suggest that the majority of the aberrations are caused by the achromatic doublet as this is the lens working at the highest numerical aperture. The *Zemax* simulation predicted the focal position to be at 197 mm. The difference in simulated and measured focal position is most likely due to small positioning errors, ~ 0.1 mm, of the lenses which shifts the focal position slightly but has a negligible effect on the waist size.

Including the viewport changes the beam shape/quality by a significant margin. The waist increases to 9.8 μm, the focal position is shifted by 2.9 mm, and the M^2 increases to 2.08. A shift in focal position is expected due to focusing through the viewport which has a higher index of refraction than air. *Zemax* simulations suggest the focal position should be increased by 1 mm, and the viewport should not introduce significant aberrations as it is modeled as a perfect optical surface. The waist, focal position and aberration increase can be explained by the nature of the viewport glass. The viewport glass in this experiment is made of Kodial which is not optical quality glass as it has to maintain a large pressure differential without cracking and can be heated to ≈ 350 °C for bakeout for vacuum apparatus [152]. It is therefore unsurprising that quite significant aberrations are introduced because of it. To reduce these aberrations a high quality optical viewport, as described in [153] could be used. These aberrations are also likely to cause the increased focal position shift. A resolution of 10 μm is still good enough for measuring blockaded spatial distributions and dynamical crystals. However, the blockade radius for the states of interest is, calculated using the method described in section 2.1.1, to be ≈ 6 μm which means obtaining the spatial distribution of a single blockade sphere would not be possible with the designed lens system.

Now that we have a lens setup to focus the autoionizing laser beam, exciting the entire MOT to a Rydberg state would result in a non-constant autoionization probability over the ensemble. This is due to the MOT being wider than the Rayleigh range of the focused autoionizing laser beam. The Rayleigh range z_R of a Gaussian beam is the distance from the focus to where the width increases by a factor of $\sqrt{2}$ from the waist, and is dependent only on the waist and the wavelength $z_\mathrm{R} = \pi w_0^2/\lambda$. For a waist of 9.8 μm, at 408 nm, the Rayleigh range is ≈ 740 μm. The $1/e^2$ width of the MOT is ≈ 1 mm. At the edge of the MOT the probability of autoionizing would be lower by a factor of 2.8, due to lower autoionizing laser beam intensity. Controlling the excitation beam radius to be much narrower than the MOT, for example by focusing the coupling beam, solves the problem of the varying autoionization probability, see section 5.3.1.

The performance of the lens system was tested at several wavelengths (408 nm, 420 nm, and 461 nm) and showed similar propagation and aberration characteristics at all wavelengths, shown in table 5.3. The M^2 were approximately 1.2 in all cases with the waist size and focal position scaled by wavelength as indicated by equation 5.3.

Wavelength (nm)	**Waist (μm)**	M^2	**Focal position (mm)**	**Relative position (mm)**
407.77	6.3 ± 0.1	1.23	196.0	0.00
419.3	6.3 ± 0.1	1.24	196.46	0.46
460.7	7.1 ± 0.1	1.22	198.25	2.25

Table 5.3: The beam propagation parameters for the three different wavelengths. Actual position is the position of the focus from the back of the final lens. Relative position is set so that the 408 nm position is zero. No viewport is used in these tests.

Due to the relative simplicity and small focus achieved other groups have used the lens design described here. For example, a lens design based upon the one presented here was incorporated into another experiment for use as an optical dipole trapping beam, at a wavelength of 915 nm, to measure single photons created by the dipole-dipole blockade [154].

5.2 Autoionization using a tightly focused beam

Focusing the autoionizing beam allows the spatial distribution of Rydberg atoms to be measured, and has the added benefit of increasing the autoionizing probability within the beam. On resonance, at high intensities, the

$5s_{1/2}nl \rightarrow 5p_{3/2}nl$ transition probability saturates [155, 156] to become

$$P_{\mathrm{de}} = 1 - e^{-\sigma_{\mathrm{de}}\Phi} \ , \tag{5.4}$$

where P_{de} is the probability of being excited to the doubly excited state, σ_{de} is the absorption cross-section of excitation, and Φ is the photon fluence. For low l Rydberg states (such as those measured in this thesis), when the second valence electron is excited the doubly excited atom ionizes very quickly, with very high probability, leading to saturation behaviour.

The transition to the doubly excited state can be thought of as a perturbation to the bare ion transition, section 4.3. The transition strength to the doubly excited state is therefore proportional to the transition strength of the bare ion transition [3], as the integral over frequency ω of the absorption profiles must be equal,

$$\int_{-\infty}^{\infty} \sigma_{\mathrm{de}}(\omega)\mathrm{d}\omega \approx \int_{-\infty}^{\infty} \sigma_{\mathrm{ion}}(\omega)\mathrm{d}\omega \ . \tag{5.5}$$

Here σ_{ion} is the absorption cross-section of the bare ion transition, $\mathrm{Sr}^{+}5s \rightarrow \mathrm{Sr}^{+}5p_{3/2}$. The absorption cross-section for excitation to the doubly excited state can therefore be approximated by

$$\sigma_{\mathrm{de}} = \sigma_{\mathrm{ion}} \frac{\Gamma_{\mathrm{ion}}}{\Gamma_{\mathrm{de}}} \ , \tag{5.6}$$

where Γ_{ion} is the linewidth of the bare ion transition, and Γ_{de} is the linewidth of the doubly excited state transition, i.e. as the doubly excited state linewidth increases, the absorption cross-section decreases. The absorption cross-section of the ion transition at the centre of the transition can be calculated from the transition wavelength, $\sigma_{\mathrm{ion}} = 3\lambda^2/2\pi$ [60], to be 7.9×10^{-14} m^2, as it is a closed two-level system. The bare ion transition linewidth has been measured in previous experiments to be 24 MHz [157]. The linewidth of the doubly excited state is obtained from its spectrum, figure 4.11b, to be

≈ 40 GHz. Substituting these values into equation 5.6 gives an estimate for the absorption cross-section of the doubly excited state to be 5.2×10^{-17} m^2.

For the autoionization laser parameters used for the experiments in chapter 4, the photon fluence was 8×10^{14} photons/m^2. Using equation 5.4, the autoionization probability with this fluence was ≈ 0.1. Focusing the autoionizing laser increases the photon fluence to $\approx 4 \times 10^{18}$ photons/m^2, leading to a probability of excitation to the doubly excited state of approximately unity.

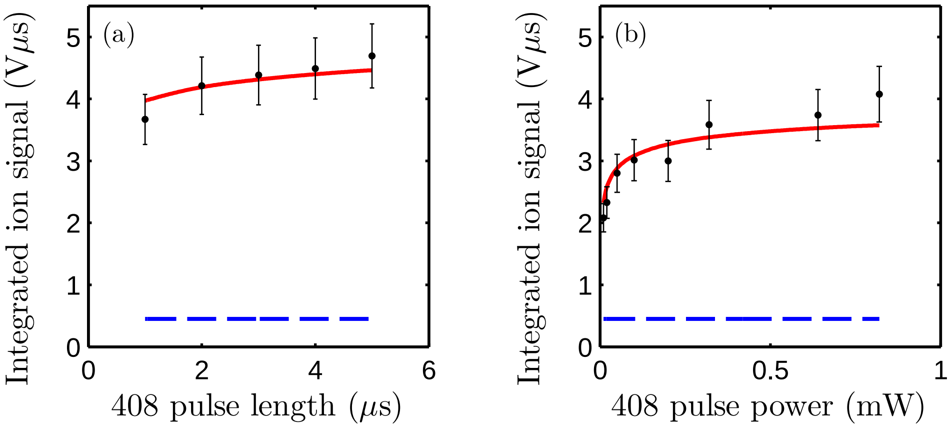

Figure 5.4: (a) Effect of varying the pulse length of the focused autoionizing laser at constant power on ion signal amplitude. (b) Effect of varying the power of the focused autoionizing laser with constant pulse length on ion signal amplitude. The red, solid line is a scaled simulation where the scaling accounts for the conversion to experimentally measured values Vμs, the blue, dashed line shows the average spontaneous ionization level of 0.45 Vμs.

To check that the autoionization probability does saturate with photon fluence, spectra in the cold atoms were taken. Two experiments to vary the photon fluence were undertaken. Firstly, the pulse length of the autoionizing laser was varied with constant power, shown in figure 5.4a. The integrated ion signal is at a near constant level, indicating the probability has saturated. The reason for the increase in autoionization-created ions at longer pulse lengths is the increase in autoionization probability in the wings of beam, with the centre saturated. This leads to an effective width increase with more Rydberg atoms in the autoionizing beam.

A second test, in which the power of the laser was varied with constant pulse length, was conducted with the results shown in figure 5.4b. The pulse length was 4 μs. A clear saturation is seen in figure 5.4b compared to figure 5.4a as the photon fluence was measured over a larger range. From these tests the autoionization parameters were set to be 1 μs pulse duration and ≈ 700 μW power for the following experiments, unless otherwise noted, to achieve a compromise of near unit probability without increasing the beam size.

Autoionizing with near unit probability in a well defined volume of the Rydberg ensemble and being able to simulate the excitation probability using the OBE, section 4.6, means it is possible to measure the collection/detection efficiency of ions in our experiment. The collection efficiency refers to the efficiency with which the created ions are directed to the MCP due to the electric field pulse and grid voltage of the MCP. The detection efficiency is the efficiency with which the ions are converted to measured signal in the MCP. The relation of ion signal to experimental parameters is

$$\text{Ion signal} = n_{\text{g}} P_{\text{de}} V \rho_{33} C \epsilon \ , \tag{5.7}$$

where n_{g} is the density of ground state atoms, P_{de} is the probability of being excited to the doubly excited state as above and is set to unity, $V = 2 w_{\text{MOT}} \pi w_{\text{auto}}^2$ and is the volume of atoms that intersects the autoionizing laser, ρ_{33} is the probability of being in the Rydberg state, C is the conversion from one ion to measured signal, and ϵ is the combined collection and detection efficiency.

The ground state density and the MOT $1/e^2$ width, w_{MOT}, can be obtained from fluorescence images. The waist of the autoionizing laser w_{auto} is measured in section 5.1.1. C is calculated from integrating single ion events. From the amplitude scaling of ρ_{33} to the measured signal (see figure 5.5a) the collection/detection efficiency of 0.21 ± 0.04 is obtained by incorporating the above constants. The error on the collection efficiency is propagated from errors on the measurements of the atom density, waist sizes, and fits to the amplitudes. The atom density and amplitude fits were found to dominate the error.

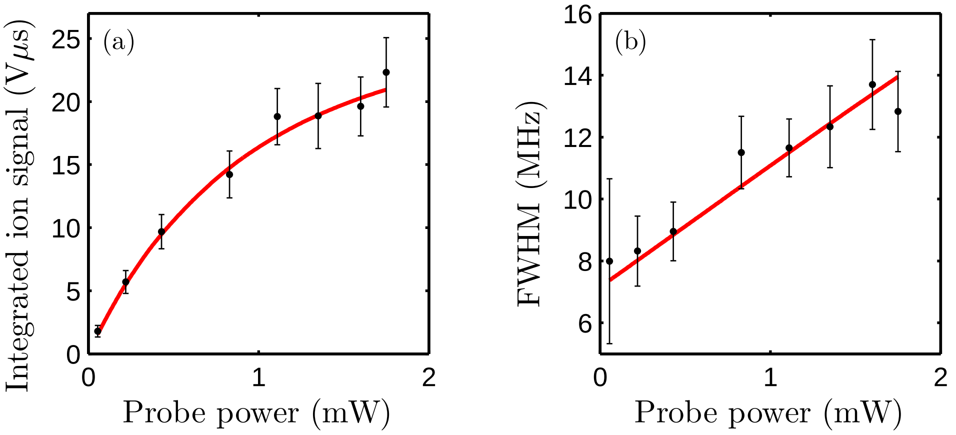

Figure 5.5: (a) The maximum integrated ion signal of spectra as a function of probe power taken with a focused autoionizing laser. (b) The FWHM of spectra as a function of probe power taken with a focused autoionizing laser. The red, solid lines are the OBE simulation. The amplitude scaling factor applied to the simulation for (a) allows calculation of the collection/detection efficiency of the experiment.

Figure 5.5a shows the Gaussian fitted amplitude of spectra as a function of probe power with scaled simulation results. Figure 5.5b shows the fitted FWHM as a function of probe power. Very good agreement between the simulation results and experimental data can be seen for both the amplitude and width, giving strong evidence that the model used to calculate the collection efficient is correct.

The grid covering the MCP has an open area of 37 %. The conversion efficiency of the MCP is approximately 0.6 in a potential of 2 keV (applied MCP front face electrode potential) [158]. Comparing the calculated collection efficiency with these values indicates that the electric fields used to direct the created ions to the MCP are very effective.

5.3 Spectra with a focused coupling laser

5.3.1 Focusing of the coupling beam

In the experiments of chapter 4 the excitation beams and the autoionizing beam all had waists of a similar size to the MOT enabling excitation and ionization of the entire cloud. Since the aim of the experiments in this thesis is to investigate the Rydberg spatial distributions the autoionizing beam was focused. Therefore, in the wings of the excitation beam there are Rydberg atoms which are not being addressed by the autoionizing laser. These Rydberg atoms can spontaneously ionize and will add background ion signal to the spatial data, lowering the signal-to-noise. A further problem caused by a large coupling laser is that the autoionizing laser ionizes a column of Rydberg atoms, therefore, looking for the blockade would be more difficult as only the central, densest part of the ensemble would be blockaded while the wings would not be. The visibility of the blockade would be reduced as the spatial signal would be averaged over blockaded and non-blockaded regions.

To get around these problems the coupling laser was also focused. The probe beam was kept at the same size as it was in the experiments carried out in chapter 4 so that the probe Rabi frequency was approximately constant across the coupling laser. Another benefit of restricting the width of the excitation volume is that the dynamics become more one-dimensional, as described in section 2.1.1.

Width measurements of the focused coupling beam

To focus the coupling laser a similar lens to the one described in section 5.1 was used. The only difference was that the final lens was a $f = +400$ mm lens, due to experimental considerations. The coupling laser had to share an axis with a MOT beam and, to get enough angular separation, a longer focal length was required. The lens setup was attached to a mirror mount for alignment and a manual translation stage to overlap the focus with the ensemble. A knife-edge measurement for the focused coupling beam is shown in figure 5.6. The Rayleigh range of the focused coupling beam, using the measured waist, is 1.15 mm.

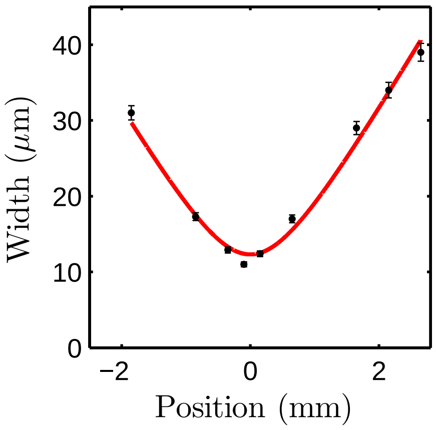

Figure 5.6: Width measurement of the focused coupling laser. The red, solid line is a fit using equation 5.3. This gives a waist of 12.3 μm, with an M^2 of 1.37.

Effect of focused coupling beam on spectra

With a tightly focused coupling laser the maximum Rabi frequency that can be reached increases significantly. A large Rabi frequency for the coupling laser should split the resonance via the Autler-Townes effect [73]. The evolution of the resonance with power was discussed in section 2.2.3.

In the Autler-Townes regime a single resonance is first broadened and then splits into two as the Rabi frequency increases, as depicted in figure 5.7a. However, the measured spectra do not exhibit this behaviour. An example is shown in figure 5.7b. The OBE model (blue, dashed line in figure 5.7b) introduced in section 2.2.1 overestimates the FWHM of the resonance such that it is not possible to overlap the OBE theory with the experimentally measured spectrum.

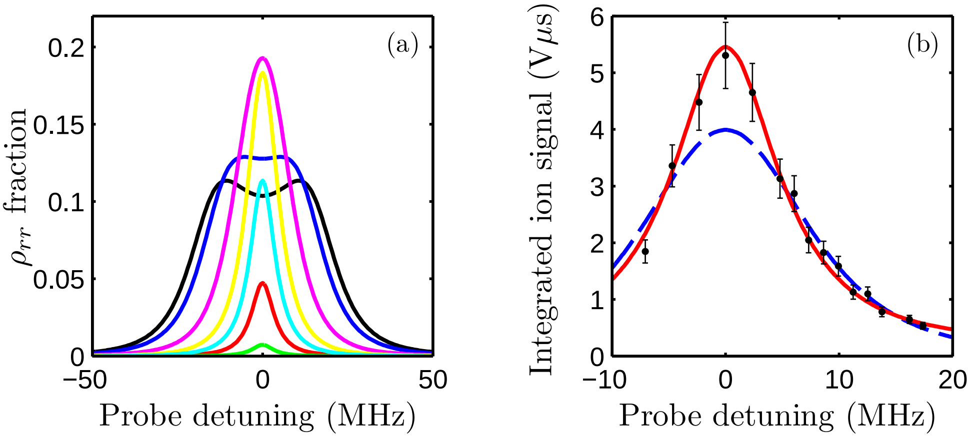

Figure 5.7: (a) Several solutions of the OBE as a function of probe detuning at different coupling laser powers. In order of increasing power the lines are green, red, cyan, yellow, magenta, blue, black. At low power the Rydberg population fraction increases linearly before becoming Autler-Townes split at higher powers. (b) A spectrum of the two-photon resonance from the saturated part of figure 5.8a. The blue, dashed line is the OBE solution without averaging. The red, solid line includes the Gaussian intensity averaging described in the text. Both models have an amplitude scaling factor.

The variation of the maximum amplitude and FWHM of spectra with coupling laser power are plotted in figure 5.8.

The behaviour of the maximum amplitude of the spectrum as a function of power is a sharp increase at low powers followed by a much slower increase at higher powers. The simple OBE solutions fit the low power results quite well but the decrease in amplitude associated with Autler-Townes splitting mean at higher powers the agreement is very poor.

The FWHM of the spectra are quite noisy at low power but the overall trend appears to be independent of power. The FWHM here are quite a bit wider compared to the spectra in section 4.6 which is most likely due to the higher probe power in these spectra. Again it is clear that the simple OBE

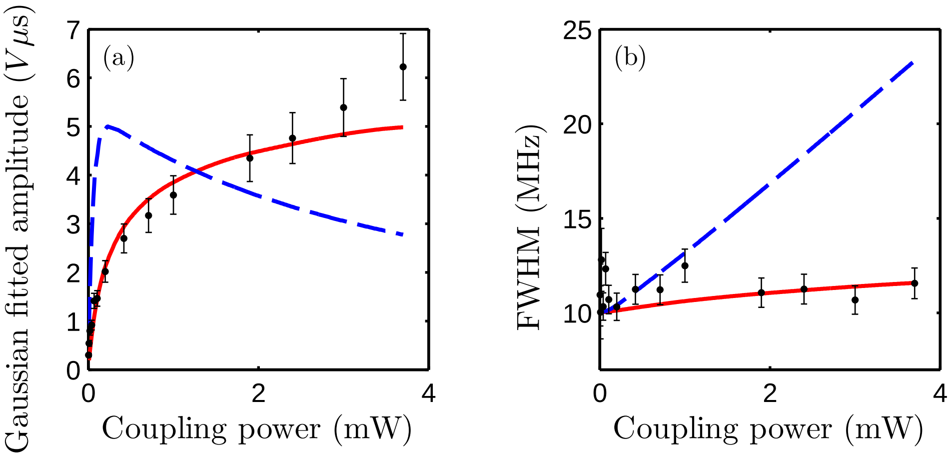

Figure 5.8: The amplitude (a) and FWHM (b) extracted from Gaussian fits to the spectrum as a function of coupling laser power. A marked saturation of the amplitude is apparent. The blue, dashed lines are the solution of the OBE without averaging. The red, solid lines are the solution of the OBE with averaging included. The spectra for this data were taken with an unfocused autoionizing laser.

simulations fail to match the data with the simulated FWHM increasing due to the Autler-Townes splitting.

To understand why the model, which worked for the previous spectra, should fail to model the spectra with a focused coupling laser the finite spatial extent of the beam must be considered.

The Gaussian ground state distribution of the MOT does not need to be included as the variation over the coupling laser is negligible due to its width, as $w_{\mathrm{MOT}} \gg w_{413}$. The probe power is constant in the simulation as well due to the negligible variation in power over the coupling laser distribution, as $w_{\mathrm{probe}} \gg w_{413}$.

In the centre of the coupling laser the Rabi frequency is much higher than in the wings, causing Autler-Townes splitting in the centre only. To calculate the spectrum in this regime the OBE model needs to be averaged over the Gaussian intensity distribution of the coupling laser.

To average over the Gaussian intensity distribution, the coupling laser is modeled as a circularly symmetric two-dimensional Gaussian split into 21 rings of equal width. The area of each ring is $\approx 2\pi r\delta r$, where r is the radius of the ring and δr the width. The final ring has a radius of $r = 2\omega_{413}$. Using more than 21 rings linearly increased the computation time while only marginally increasing the accuracy of the results. The Rabi frequency for each ring is calculated from its amplitude. The linewidths used in the simulation are the same as for the simulation without the averaging since the linewidths are set by the laser locking parameters, which have not changed.

The simulation calculated the Rydberg fraction ρ_{rr}, for each ring for a probe detuning of -50 to +50 MHz in steps of 1 MHz. For each probe detuning the results are averaged using a weighted average that takes into account the circular symmetry of the beam. The rings are given a linear weighting with r due to the area of the rings scaling. The results of the Gaussian averaging on the OBE fit (figure 5.7b), is clearly in better agreement than with the simple OBE model.

The OBE simulations with averaging included fit the data quite well at both high and low power. There is a slight divergence at the highest power with the data trending upward still and the simulations tending to a constant value. The additional increase in signal at the highest powers may be due to the other m_{J} excitations being weakly allowed as the quantization is not perfect, therefore increasing the Rydberg fraction in those states. There would be a linear increase in signal of the other states as the excitation probability is low. The results of the simulation for the amplitude behaviour have an amplitude scaling parameter; this takes into account the conversion from Rydberg excitation probability to detected ion signal.

The averaged OBE simulations have a much more gradual increase in FWHM with power and fit the data quite well.

The reason why the averaging was unimportant for fitting the spectra in section 4.6 is that the Autler-Townes regime was never reached, therefore the Rydberg fraction was approximately linear with laser power.

5.4 Translation stage

The effects of having focused excitation and coupling lasers on the spectra have been discussed, now the mechanism by which the autoionizing laser is translated across the ensemble will be described and characterized. The translation stage used in the rest of the experiments in this thesis is the *New Focus* miniature steel motorized linear stage (*MFA-PP*). This stage was chosen as it has a travel range of 25 mm, a minimum incremental step size of 0.1 μm, and can carry several kilograms of mass (i.e. much heavier than the lens setup). The stage can be controlled via computer and can be interfaced with *LabVIEW*, allowing spatial distribution measurements to be automated.

The setup for the translation stage and lens system is shown in figure 5.9. The manual translation stage (*Comar 110 XT 65*) allows axial overlap of the beam focus with the atomic ensemble.

The lens system is attached to the translation stage via a kinematic mirror mount (*Thorlabs KM100T*) to allow for fine alignment onto the atomic sample.

If the manual translation stage is attached to the bench and the automatic stage attached to the manual translation stage, then horizontal translation is possible. To translate along the vertical axis the automatic stage can be attached to the manual stage with a right angle bracket (*Thorlabs AP90*).

5.4.1 Accuracy of the translation stage

The manual for the translation stage [159] quotes the stage to have a positioning repeatability of 2.5 μm. As the translation stage is such an important

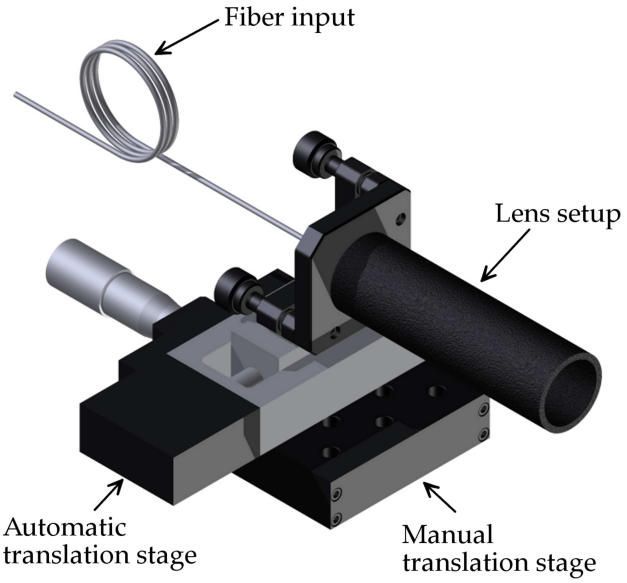

Figure 5.9: The lens system attached to the automatic translation stage. The manual translation stage is used to overlap the focus of the beam with the atomic sample. The mirror mount is for fine alignment.

part of the experiment thorough testing of its accuracy was carried out. The linearity of movement with set position was measured, as was the repeatability of positioning and the overall accuracy.

Dial indicator

The first test of linearity and repeatability was to use a mechanical dial indicator. The setup for this is shown in figure 5.10a. The translation stage pushes against the dial indicator and the position can be measured. The dial indicator has a resolution of 1 μm. The stage was moved a total of 1 mm in 20 μm steps and repeated five times with the stage homed between each set of measurements. The result is shown in figure 5.10b. The standard error on the data points from the five repeats is 0.5 μm; this is limited by the precision of the dial indicator. These errors are too small to be shown in figure 5.10b. The motion of the translation stage is close to linear. Analysis of the residuals shows a small deviation from linear at the few micron level, with an RMS

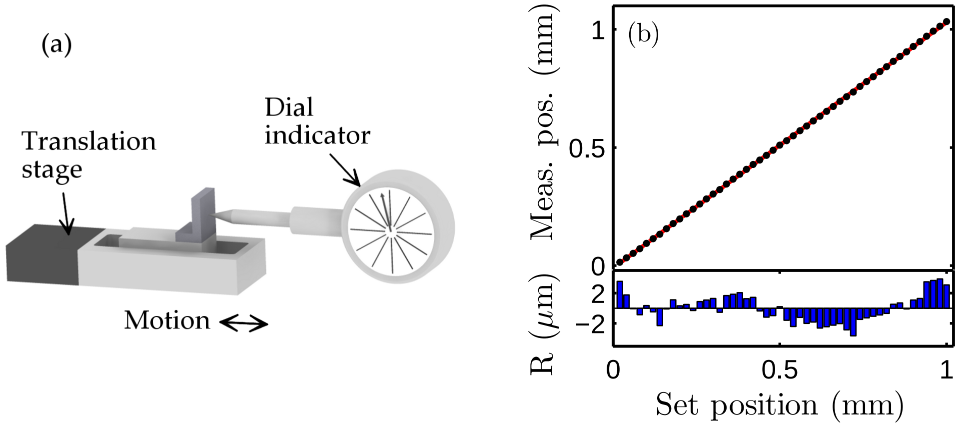

Figure 5.10: (a) The setup for testing the linearity and repeatability of the stage using a dial indicator. (b) Upper panel: The position measured on the dial indicator as a function of the set position of the stage. The black dots are the data, with the errors being smaller than the data points. The red, solid line is a linear fit, with a gradient of 1.040 ± 0.005 measured position/set position. Lower panel: The residuals, R, between the data and the linear fit.

deviation of 1.8 μm. The repeatability is also excellent indicated by the error on each point. However, the gradient is 1.040 ± 0.005 measured position/set position, indicating the translation stage moves an extra 40 ± 5 μm over a set millimeter of travel. The deviation from a 1:1 gradient could be due to a calibration error in the dial indicator.

Camera image

A second, independent, test of the linearity and repeatability was done using the CCD camera. The lens system described above was imaged onto the camera using a $2f$ imaging setup. The lens setup was translated by 6.5 mm in 0.5 mm steps with a camera image taken at each point. The image is fit with a Gaussian profile and the fitted centre point is taken as the measured position. The pixel size of the camera is 6.45 μm, but the Gaussian fit means an accuracy of better than half of the pixel size. The measured positions along the direction of travel are shown in figure 5.11a. The data are fit with a linear trendline of gradient 0.95 measured position/set position. This indicates that the imaging system of the camera has a slight magnification error, i.e. the imaging lens is axially misplaced by a small distance. Again the stage shows close to linear behaviour. Analysis of the residuals shows a small quadratic dependence at the few micron level which is possible due to spherical aberrations in the imaging lens of the camera. The RMS deviation of the residuals is 1.7 μm. The position of the peak in the direction orthogonal to travel is shown in figure 5.11b. The gradient here is - 2.3 μm/mm. The non-zero displacement could be due to the camera being at a slight angle to the translation stage (≈ 0.15 °). The residuals show no obvious trend, with an RMS deviation of 0.3 μm.

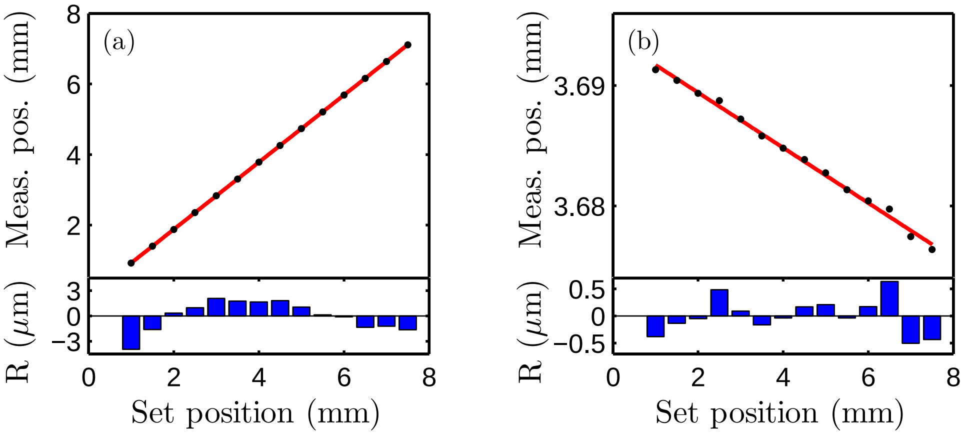

Figure 5.11: The linearity of the stage as measured on the camera. (a) Upper panel: The measured position of the focused beam along the direction of travel. The black dots are data with the red, solid line a linear fit. Lower panel: Residuals, R, between the data and the linear fit. (b) Upper panel: The measured position of the focused beam orthogonal to the direction of travel. Lower panel: Residuals,R , between the data and the linear fit.

Michelson interferometer

From the previous two subsections the translation stage has a linear, repeatable response to set position. However, the absolute accuracy of the stage could not be measured due to calibration issues in the experiments. To get around the calibration problems a Michelson interferometer [160] was assembled, see figure 5.12a. The translation stage was moved over a distance of 1 mm at a constant velocity and the interference pattern measured on a photodiode. The wavelength of light is 419.3 nm, meaning the fringe spacing should be 209.65 nm apart and therefore 4770 fringes should occur over 1 mm. The fringes were counted in a *MATLAB* program. Four repeats were taken with the average number of measured fringes being 4460 ± 7, relating to an accuracy of 2 ± 1 μm over a 1 mm travel range. The measured accuracy is within the tolerances quoted by the manufacturer. An example of the interference fringes measured are shown in figure 5.12b. Shown are some fringes from the start of the translation and some from near the end of the translation. The fringe visibility is just under 90 % meaning the chance of missing fringes is very small. The fringes should form a sine squared wave, however, it is clear they do not. The deviation from the expected profile is attributed to vibrations of the translation stage during motion and small non-uniformities in the velocity of the stage. The stage is designed to be accurate to position, but less accurate to constant velocity.

Conclusion

The preceding tests show the translation stage repeatably moves to the same position with 2 μm resolution. The waist of the autoionizing beam being just under 10 μm means the translation stage accuracy is not limiting the resolution of our experiments.

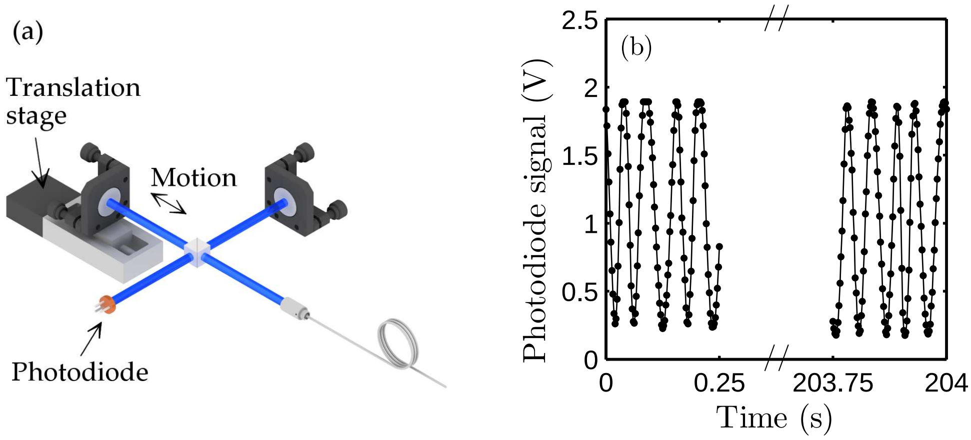

Figure 5.12: (a) The setup used to measure the interference fringes from a Michelson interferometer. (b) An example of the fringes measured on the photodiode. Some fringes are shown from the start of the translation and some from near the end of the translation, showing very good fringe contrast throughout the translation. The black dots are the result of binning the raw signal over three positions. The black, solid line joins the data points to guide the eye.

5.5 Excited state spatial distribution

To measure the spatial distribution of the Rydberg atoms a similar experimental sequence to the one used in section 4.3 is applied. The spatial position of the autoionizing laser is stepped, instead of the frequency of the probe, and the ion signal collected. The frequency of the probe laser is set to be at the centre of the measured two-photon resonance (i.e. maximum transition probability). Changes in the coupling laser power and ground state absorption (caused by changes in the atomic flux in the locking cell) mean the lock point of the coupling laser can vary by several MHz day-to-day. To account for lock point drift a spectrum is taken to measure the two-photon excitation lineshape before translation experiments. The sequence is repeated 250 times. The translation stage is then stepped to the next position and another 250 averages are repeated. One camera image is taken at each spatial position.

The experimental layout is shown in figure 5.13. The probe and coupling lasers are counter-propagating and are aligned along the axis of the quantization field. The polarizations are set to drive $\sigma^+\sigma^+$ transitions, corresponding to the $m_J = +2$ Rydberg state. The autoionizing laser is translated either parallel (along the z-axis) or orthogonal (along the y-axis) to the direction of propagation of the coupling beam.

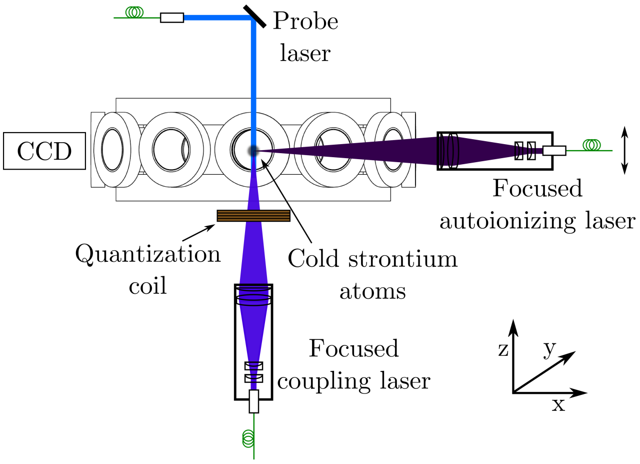

Figure 5.13: The beam geometry used for taking Rydberg state spatial distribution measurements. The probe and coupling lasers are counter propagating along the quantization field axis (z-axis). The autoionizing laser enters the vacuum chamber from an orthogonal axis to the excitation beams (x-axis). The arrow shows the direction of translation longitudinally along the excitation beams. To measure the width of the coupling laser the autoionizing laser is translated in the plane of the page (y-axis). The autoionizing laser is imaged onto the camera to obtain the position for the ground state distribution corresponding to the Rydberg distribution.

An example of a Rydberg state spatial distribution with an unfocused coupling laser is shown in figure 5.14. In this experiment the translation step size was 25 μm with 100 steps in total along the z-axis. The coupling laser was not focused for this measurement. The non-zero ion signal in the wings is due to spontaneous ionization of the Rydberg atoms outside the autoionizing beam. Spontaneous ionization is present at all spatial positions as it is independent of the autoionizing laser. It should be approximately constant since the amount and position of the Rydberg atoms being created should not vary between experimental shots.

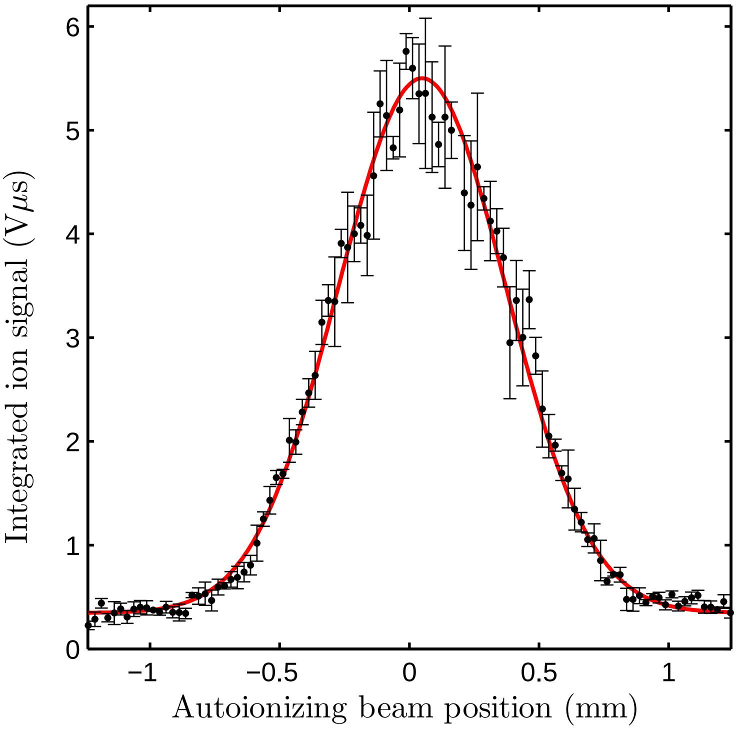

Figure 5.14: Spatial distribution of the 5s56d $^1D_2$ state. The error bars are the standard error based upon several repeat measurements. The red, solid line is a Gaussian fit.

The signal-to-noise is very good with the average signal-to-noise ratio being 9. The maximum autoionization signal to spontaneous ionization signal ratio is ≈ 13. This is the maximum ion signal value divided by the average signal in the wings. The spontaneous ionization signal could, depending on the mechanism, come from anywhere in the Rydberg ensemble, i.e. approximately the size of the MOT, which is $\approx 4\ \text{mm}^3$. The autoionization signal can only come from the autoionization beam; this can be thought of as a cylinder with a radius of that of the autoionizing laser beam waist and a length equal to that of the diameter of the MOT. This gives a volume of $\approx 0.001\ \text{mm}^3$. The signal-to-background ratio being so high with the volume ratio being so unfavourable is remarkable; this gives us confidence that the autoionization microscopy technique could be used to study any spatial effects which arise due to interactions.

Spatial distributions with the coupling laser focused

As discussed in section 5.1.1 the coupling laser should be focused. The excitation volume is now described by the coupling laser waist in two dimensions and the atomic ground state distribution in the other. In essence the Rydberg state distribution becomes cigar shaped.

The focus of the coupling laser needs to be overlapped with the MOT and with the focus of the autoionizing laser. Overlapping the focus of two tightly focused beams in a vacuum chamber is a challenge if the beams cannot be imaged on a camera. To overlap the focus of the coupling laser with the ensemble the spatial profile across the coupling beam was measured by translating the autoionizing laser across it (y-axis). The measured width is then the convolution of the coupling and the autoionizing beams. The smallest measured waist was 32 μm, this is shown in figure 5.15a. The spatial profile along the coupling laser (z-axis) with the data from figure 5.15a are shown in figure 5.15b. The aspect ratio is $\approx$ 30. The narrowest measured waist is larger than the convolution of the two beams, which gives a waist of $\approx$ 16 μm. Some of the possible reasons for this are described in section 5.6.

Alignment of the coupling laser

The alignment of the coupling laser is another important factor. Due to the narrowness of the coupling and autoionizing lasers the coupling laser needs to be very close to vertical. If the coupling laser is off-axis then the autoionizing laser will no longer overlap with it along the full ensemble length during a translation experiment. This will cause asymmetry and/or an amplitude

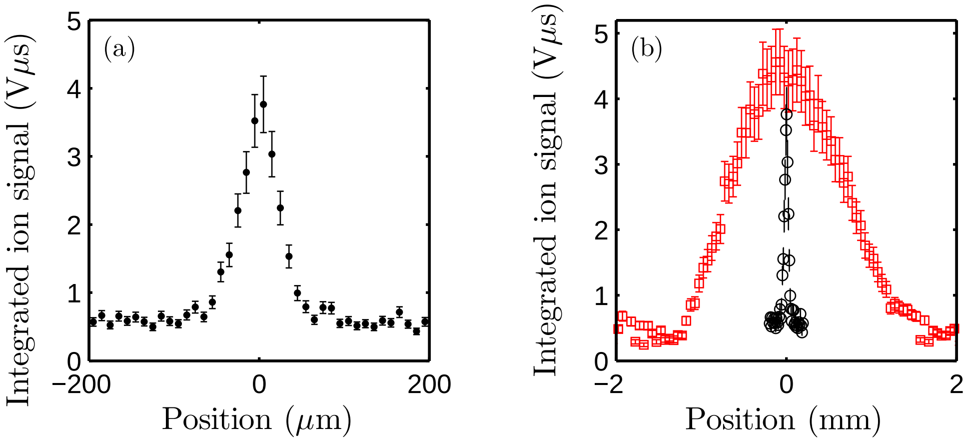

Figure 5.15: (a) Spatial distribution of the Rydberg state across the waist of the focused coupling beam (y-axis). (b) Red squares are the spatial distribution along (z-axis), and black circles are across (y-axis) the focused coupling laser. The black circles are the same data from (a).

modulation in the measured Rydberg distribution.

To measure the alignment of the coupling laser, spatial measurements were taken across the focused coupling laser (y-axis in figure 5.13) at different longitudinal positions along the coupling laser (z-axis). The autoionizing laser beam's focal position was adjusted to probe the different longitudinal positions using the mirror mount that is attached to the lens tubing. The vertical position of the autoionizing laser was measured on the CCD camera.

Five spatial distributions at different longitudinal positions are shown in figure 5.16a. The different signal amplitudes are caused by the Gaussian profile of the ground state distribution in the longitudinal direction. These distributions are fit with a Gaussian profile and the centre positions are extracted. These centre positions are shown in figure 5.16b. The error bars on these positions are 700 nm and are the standard error based upon several repeat measurements of the same spatial position. Based on the width of the MOT and measured waists of the focused lasers the angle from vertical is small enough to be considered acceptable.

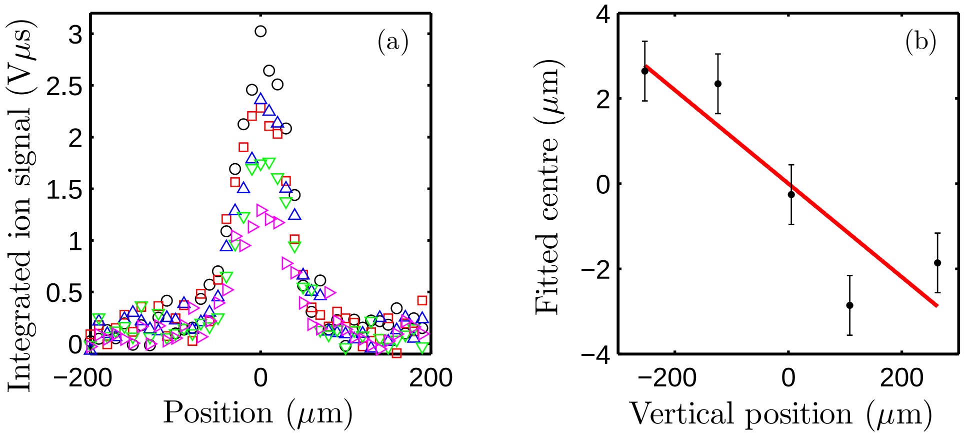

Figure 5.16: (a) Several spatial distributions across the waist of the focused coupling laser at different vertical positions. (b) The fitted centre positions of the data in (a). The red, solid line is a linear fit to the positions, giving a gradient of 11 ± 2 transverse μm/longitudinal mm, or an angle of $0.6 \pm 0.1°$ from vertical.

5.5.1 Two-dimensional Rydberg spatial distribution

By measuring the Rydberg spatial distribution vertically along the coupling laser (z-axis) then moving the autoionizing beam a small amount along the y-axis and taking another vertical distribution, the two-dimensional Rydberg spatial distribution can be built up. The two-dimensional Rydberg spatial distribution is shown in figure 5.17. A ground state fluorescence image is also shown for comparison. The spatial distribution is made of 12 vertical slices of 50 steps with a resolution of 80 μm. To get the horizontal position of the autoionizing beam the focus is imaged on to the same CCD camera as used for the fluorescence image. The resolution in the horizontal plane is then set by the CCD pixel size of 6.45 μm. As the coupling laser beam is being focused the Rydberg distribution is much narrower than the ground state distribution. The Rabi frequencies used for the probe and coupling lasers are such that the Rydberg distribution is in the low power linear regime of figure 5.8a. The ion counting method of data collection is thus used to make the two-dimensional map.

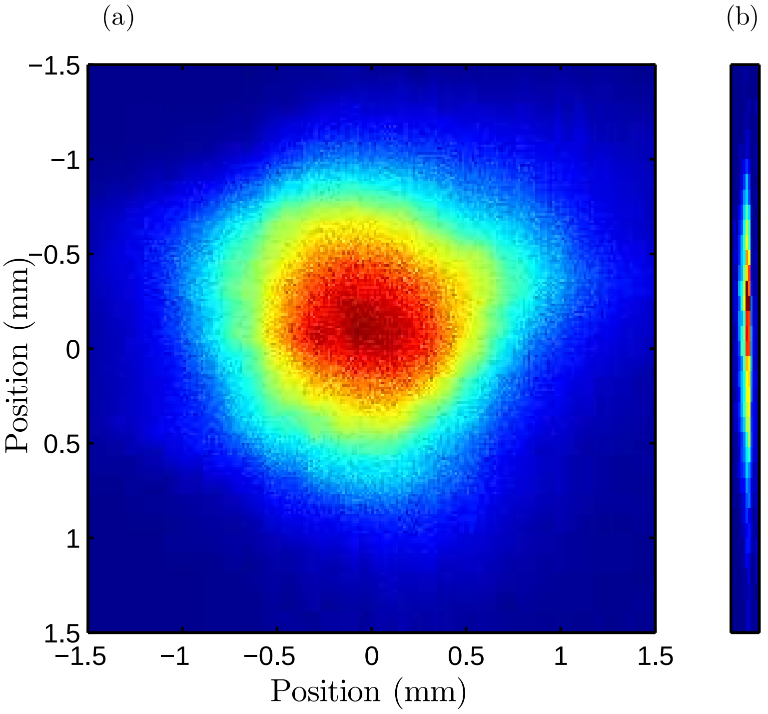

Figure 5.17: (a) A false colour fluorescence image of the MOT taken with the CCD camera used for atom number/density measurements, corresponding to the spatial distribution of the ground state. (b) A false colour image of the Rydberg state spatial distribution made up of 12 vertical translation measurements. The spatial proportions are the same for both images.

With the position of the autoionizing beam on the camera being known the fluorescence of the ground state at the same position can be extracted. Figure 5.18a shows a Rydberg state spatial distribution with its associated fluorescence slice. The ion signal is one of the slices used to create the two-dimensional spatial distribution. The amplitudes are scaled to give best overlap between the two distributions. There is qualitatively good agreement between the fluorescence and the ion signal spatial distributions. At the densities and Rydberg state used in this experiment no interactions are expected so the Rydberg state distribution should follow the ground state distribution. The agreement between the excited and ground state distributions gives further evidence that the autoionizing microscopy technique could be used to study modifications to the spatial distribution caused by interactions.

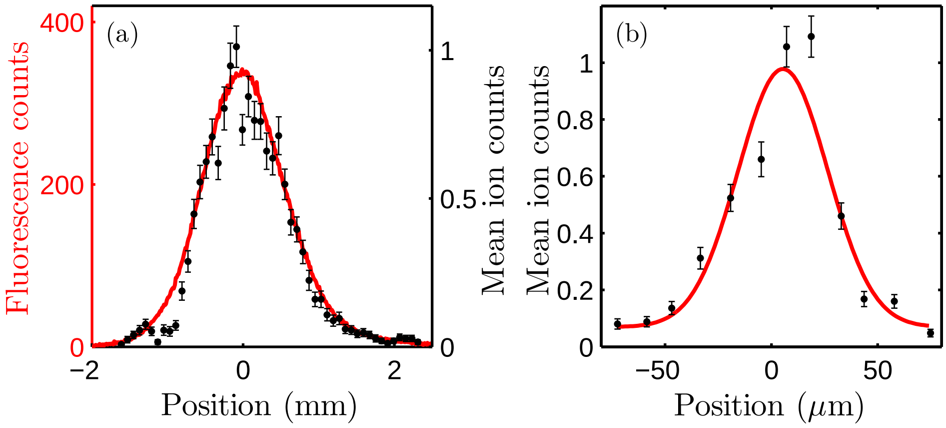

Figure 5.18: (a) An example slice along excited state spatial distribution (ion counts - black dots) with ground state distribution (fluorescence counts - red, solid line) overlaid. This is one of the slices from figure 5.17b along the direction of propagation of the coupling laser. (b) Excited state spatial distribution orthogonal to the direction of propagation of the coupling laser. The red, solid line is a weighted, least-squares Gaussian fit with a $1/e^2$ width of 42 ± 6 μm.

A slice across the two-dimensional Rydberg spatial distribution is shown in figure 5.18b. The measured width is wider than the narrowest measured width - measured when taking translation measurements across the waist - but this may be due to the fairly small number of points. The larger fluctuations compared to the previous widths are probably due to the time between experiments causing small changes in Rabi frequency and atom number.

Fluctuations in the spatial distributions

The Rydberg spatial distribution and the fluorescence image can be fit with a Gaussian distribution (red, solid line), figure 5.19. In the linear excitation probability, non-interacting Rydberg regime, and non-heavily saturated autoionizing laser, the Rydberg state distribution should be Gaussian. Studying the normalised residuals should make departure from Gaussian distributions more apparent, i.e. other spatial structure.

The normalised residuals of the Rydberg signal show a clear pattern. However, the fluorescence shows a similar pattern with normalised residuals of similar size. As the patterns in the residuals are similar, this would indicate that the departure from Gaussian of the Rydberg state distribution is caused by a departure from Gaussian of the ground state distribution. The non-Gaussian ground state distribution could be caused by a small misalignment of the MOT beams or because we are in the density-limited regime [110].

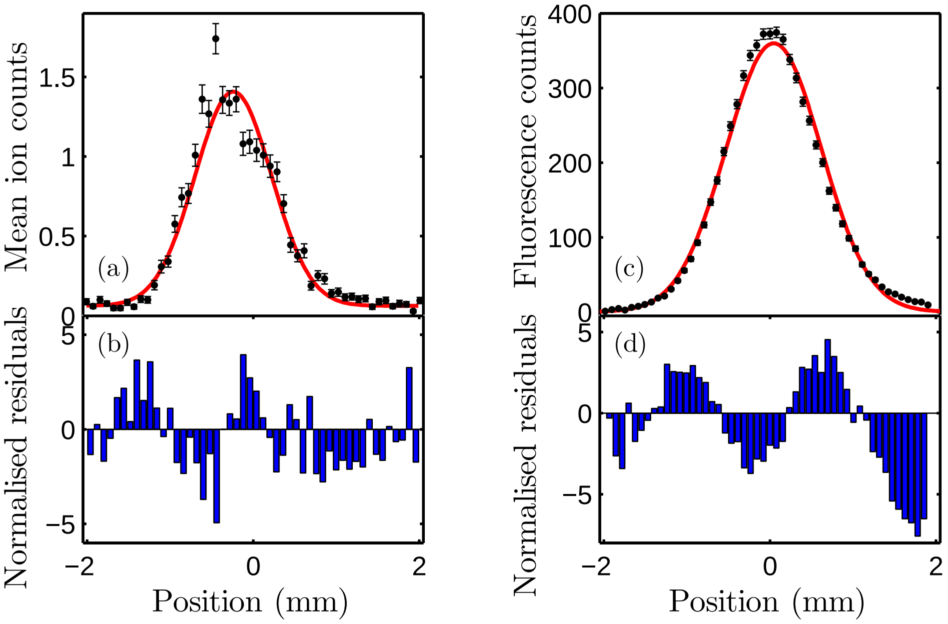

Figure 5.19: (a) A single slice of the Rydberg state spatial distributions from figure 5.17 with a weighted, least-squares Gaussian fit overlaid (red, solid line). (b) The normalised residuals of the measured data and the Gaussian fit. (c) A slice of the fluorescence image related to the intersection point of the autoionizing laser beam with the MOT. The error bars come from shot noise, i.e. are the square root of the counts. For clarity 50 points of the fluorescence slice were sampled. The red, solid line is a weighted, least-squares Gaussian fit to the fluorescence. (d) The normalised residuals of the Gaussian fit to the fluorescence.

5.5.2 Counting statistics

Using the ion counting technique, see section 4.2.1, allows access to the count statistics of the spatial distributions. The usefulness of the autoionization microscopy technique is enhanced because of the statistics available, not just the mean signal. An example of the occurrences of each amount of counts as a function of spatial position are shown in figure 5.20. The ordinate is the cumulative amount of occurrences of each count. There are 250 averages at each spatial position, hence the sum at each position is 250. The dark blue corresponds to the amount of occurrences of zero counts, lighter blue the amount of occurrences of one count, etc. The mean ion counts as a function of position are shown in the lower panel.

Looking at the count distribution at a specific spatial position gives an indication of the statistical distribution it follows. An example of the count distribution at the position indicated by a line on figure 5.20 is shown in figure 5.21. A low count rate with a constant mean should follow a Poissonian distribution [161], hence the expected Poissonian distribution with that mean is also displayed in figure 5.21. The degree to which the data are fitted by a Poissonian can be quantified using the reduced χ^2 [140].

The reduced χ^2 as a function of position for the same spatial distribution in figure 5.20 is shown in figure 5.22a. For the 250 total occurrences the fit to a Poissonian distribution should be rejected if the reduced χ^2 is greater than 1.3 [140]. In the wings, where only spontaneous ionization causes ion signal, the data are well described by the Poissonian. However, in the centre of the spatial distribution, where the ion signal is due to autoionization sampling the local Rydberg population, large fluctuations in the reduced χ^2 are seen. Unfortunately the reduced χ^2 can only indicate whether the statistical distribution can be well described by a Poissonian distribution or not. To obtain further information about the statistics the Mandel Q-parameter should be implemented.

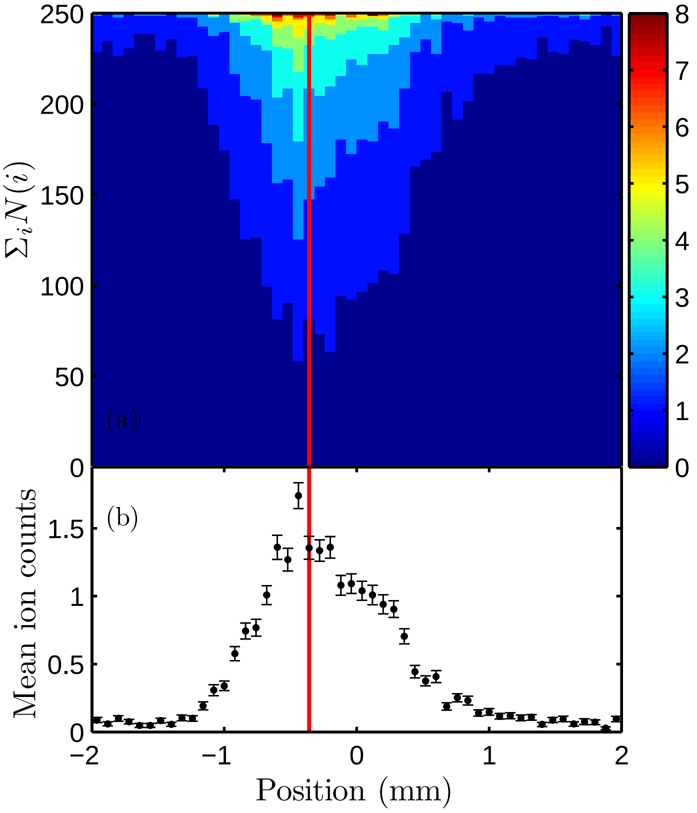

Figure 5.20: (a) The cumulative amount of occurrences of each count. The dark blue is the amount of zero counts, the lighter blue is the amount of one counts and so on at each spatial position. At each position there are 250 averages. (b) The mean ion counts at each spatial position along the coupling laser through the maximum of figure 5.17b. The red, vertical line shows the position of figure 5.21.

5.5.3 Mandel Q-parameter

The Mandel Q-parameter [162] tests whether the fluctuations of a distribution are super- or sub-Poissonian. The Mandel Q-parameter is calculated by

$$\mathrm{Q} = \frac{\langle(\Delta \mathrm{n})^2\rangle}{\langle \mathrm{n}\rangle} - 1\ , \tag{5.8}$$

where $\langle(\Delta n)^2\rangle$ is the variance of the statistical distribution $\langle(\Delta n)^2\rangle = \langle n^2\rangle - \langle n\rangle^2$, and $\langle n\rangle$ is the mean of the statistical distribution. For a Poissonian

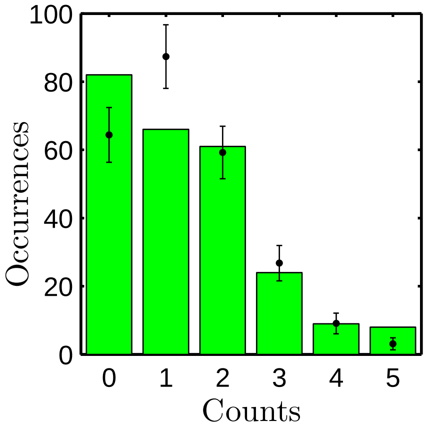

Figure 5.21: An example of the measured counts (green bars) at a specific spatial position, indicated by the red, vertical line on figure 5.20. The black dots represent the expected Poissonian distribution of the same mean. The error bars are the square root of the expected value.

distribution the variance is equal to the mean, hence Q = 0. For super-Poissonian fluctuations $Q > 0$, and for sub-Poissonian fluctuations $Q < 0$. The minimum value Q can take is -1 for an infinitely narrow distribution (a variance of zero) and the maximum value Q can take is unbounded. An example of super-Poissonian statistics is the detected photon stream obtained from a thermal light source [163]. An example of sub-Poissonian statistics is achieved for photon anti-bunching from resonance fluorescence of a single atom [164].

In a blockaded sample the fluctuations should be sub-Poissonian [17] because the variance is narrowed, compared to the mean as higher number excitations are suppressed. Measuring the Q-parameter will give another indication of having reached the blockade.

The Q-parameter as a function of position for the same spatial distribution in figure 5.20 is shown in figure 5.22b. Although the Q-value is quite noisy in the wings, with the value fluctuating between -0.1 and +0.1, in the centre of the distribution, where the mean signal is larger the Q-value is always positive. The statistics of the distribution are therefore super-Poissonian.

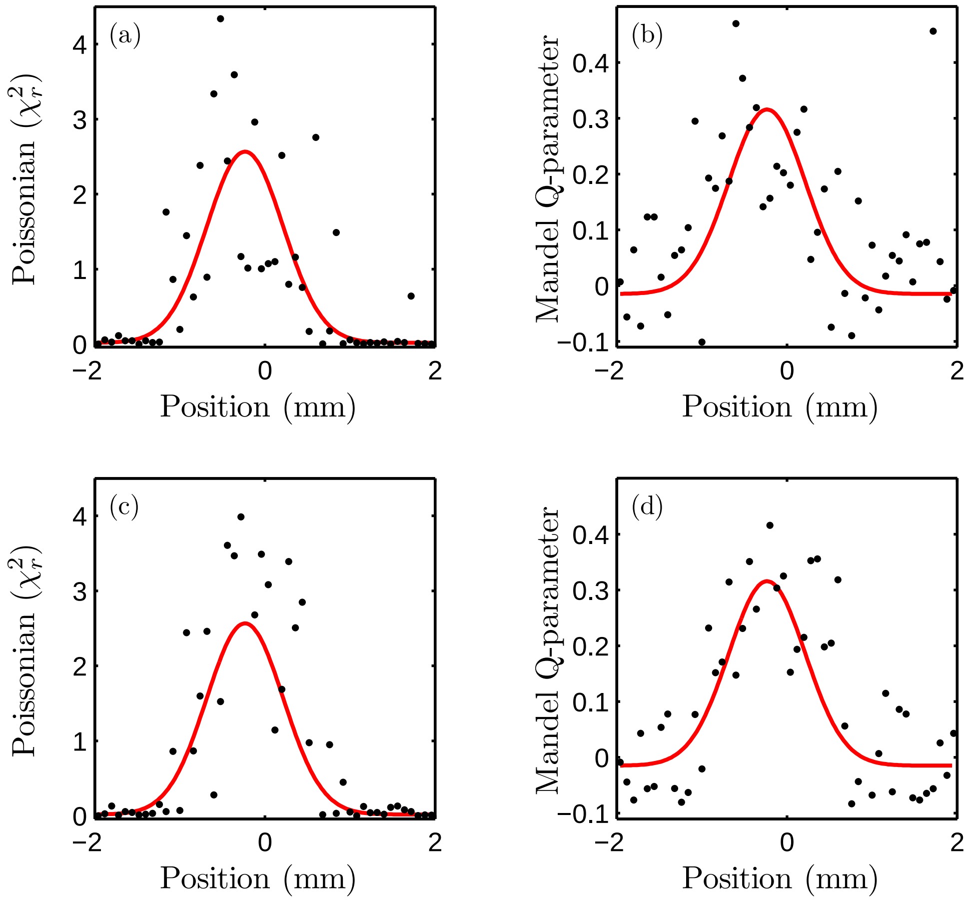

Figure 5.22: The reduced χ^2 (χ_r^2) of a Poissonian fit to the number of counts as a function of spatial position (a) for the data from figure 5.20 and (c) for the Monte Carlo simulation. The Mandel Q-parameter (b) for the same spatial data, and (d) for the Monte Carlo simulation. The red, solid lines are the Gaussian fit from figure 5.19a, scaled to indicate the mean signal.

To model the super-Poissonian statistics a Monte Carlo simulation incorporating the Poissonian nature of low mean count rate sampling and Gaussian fluctuations to the Rydberg atom number was used. At each spatial position the simulation is executed 250 times to get the same amount of statistics as was collected in the experiment. The Gaussian fit to the ion signal from figure 5.19a is used as the mean at each spatial position. For each run of the simulation the mean value is given a Gaussian fluctuation to account for fluctuations in the excitation laser powers and detuning, and ground state atom number. The Gaussian fluctuations are created using the Box-Muller transform [165]. The mean is then used as a seed for a Poissonian Monte Carlo algorithm to create counts. The reduced χ^2 fit to a Poisson distribution and the associated Q-parameter are then calculated from the 250 occurrences at each spatial position. The results of the simulation are shown in figure 5.22.

Super-Poissonian statistics cannot be caused by missed counts at the detector, as this does not alter the counting statistics. Missing counts merely reduces the value of Q by the detector efficiency [166]. If the reference level for the ion counting is too low then "ringing" events, i.e. double counts for a single ion event can occur, see section 4.2.1. These ringing events can create a super-Poissonian distribution. However, the Monte Carlo simulations show that at the amount of ringing events expected for the reference level used (< 1 %) the increase in Q is negligable.

For the simulation the only variable is the standard deviation of the Gaussian fluctuations applied to the mean. To get qualitative agreement between the data and the simulation the Gaussian fluctuations had a standard deviation of $\approx 0.5 \times \langle n \rangle$. These fluctuations are quite large indicating large shot-to-shot changes in the Rydberg atom number, most likely due to atom number variations and laser power and detuning fluctuations.

When the blockaded limit is reached the Q-parameter should reduce but will not necessarily become sub-Poissonian [167–169].

5.6 Spatial distribution variation with laser power

5.6.1 Spatial distributions with coupling laser power

Varying the power with a focused coupling laser changed the spectra due to the large variation in coupling Rabi frequency across the beam. Using a focused autoionizing laser we can probe the shape of the excitation volume to see if the Autler-Townes splitting affects the spatial distribution.

The results of varying the coupling laser power are shown in figure 5.23. The amplitude of the spatial distributions are shown in figure 5.23a and the associated width shown in figure 5.23b. The amplitude follows a similar saturation type behaviour as the spectra did. The width shows a slight increase with coupling laser power. The reason for these behaviours is again Autler-Townes splitting. The effect of the Gaussian intensity distribution is to again Autler-Townes split the resonance at the centre of the beam and therefore have a reduced Rydberg fraction compared to the wings. As the autoionizing laser takes a column integral over the two-dimensional Rydberg fraction this serves to flatten the centre of the distribution and thus create a slightly wider distribution.

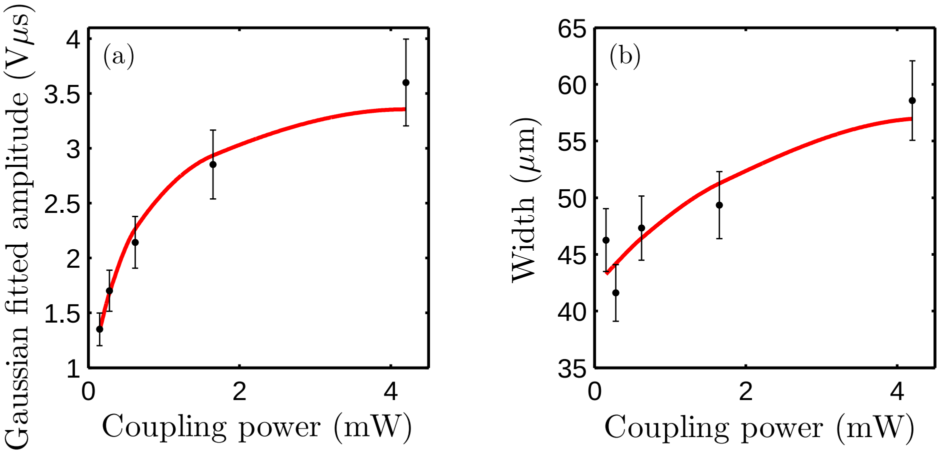

Figure 5.23: (a) The Gaussian fitted amplitude of the spatial distribution across the waist of the focused coupling laser with coupling laser power. (b) The Gaussian fitted $1/e^2$ width of the spatial distribution of the focused coupling laser with coupling laser power. The red, solid lines are the solution to the model described in the text.

To model this data a numerical convolution method is employed. The convolution is between the Rydberg population and the autoionizing probability distributions. The result of the convolution is proportional to the measured ion signal. Due to the cylindrical symmetry of the beams only a two-dimensional grid is required. The simulation grid is on a plane orthogonal to the coupling laser and parallel to the autoionizing laser. A two-dimensional Gaussian distribution pertaining to the coupling laser intensity is created within a square grid, see figure 5.24a. At each point the OBE is solved and the Rydberg fraction calculated. The probe power and ground state distribution are again kept constant across the grid due to the sizes of the beams. The autoionizing laser is modeled as a one-dimensional Gaussian distribution constant along one axis, see figure 5.24b. The simulation is then calculated at several coupling powers.

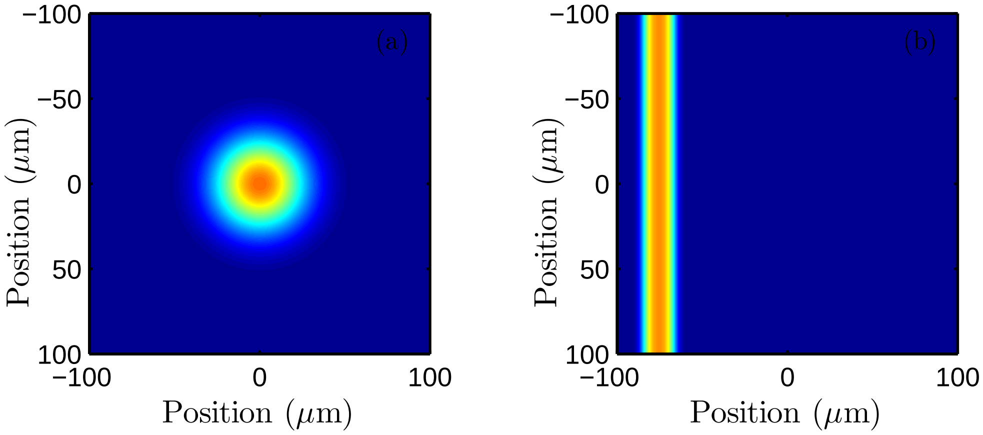

Figure 5.24: Examples of the grid used to simulate the spatial distribution variation with coupling laser power and autoionizing laser power. (a) The intensity distribution of the coupling laser. (b) The intensity distribution of the autoionizing laser. Red is higher probability in both cases.

The maximum amplitude given by the simulation is fit to the amplitude of the spatial distribution shown in figure 5.23a using a free scaling parameter as before. The width simulation results have no scaling parameters. Both the amplitude and width simulations agree well with the data.

The distortion in the shape of the Rydberg state spatial distribution could easily mask any correlation effects that we may wish to study. Having the atoms in the peak of the coupling laser Autler-Townes split could also lead to a smearing in the correlations. Thus, it is important when looking for the blockade that coupling laser powers which correspond to the linear regime in figure 5.8a are used. However, this corresponds to quite low Rydberg excitation probability ≈ 10 %. The excitation probability combined with the small overlap region of the two focused lasers $\approx 20{,}000\ \mu\text{m}^3$, and the relatively low density of the atoms $\approx 2 \times 10^9$ atoms cm^{-3}, means fewer than ten Rydberg atoms on average are in the autoionization beam in an experimental shot. The detection efficiency of the MCP further reduces the signal. However, the ion counting mechanism mentioned in section 4.2.1 means that signal-to-noise is not an issue for these small signal sizes.

5.6.2 Spatial distribution with autoionizing laser power

The saturation of the autoionization transition, mentioned in section 5.2, can also cause a distortion to the measured excited state spatial distribution using the autoionization microscopy technique. With low power in the autoionizing laser $\Phi\sigma_{\text{auto}} \ll 1$, the excitation probability to the doubly excited state is linear with power, equation 5.4. With low coupling laser power as well, the measured spatial distribution should be a convolution of the two Gaussians. In the saturated autoionization regime, $\Phi\sigma_{\text{auto}} \gg 1$, the autoionization probability reaches unity at the peak intensity but in the wings it is still increasing linearly. This causes a flat top distribution of the autoionization probability as the probability of autoionizing cannot exceed unity. As the power of the autoionizing laser increases the width of this flat feature increases also, lowering the resolution of the autoionization microscopy technique.

The effect of the autoionizing laser power on the amplitude and width of the spatial distribution are shown in figure 5.25. The fitted amplitude saturates quickly with the autoionizing laser power since the autoionizing laser width becomes equal to, and then exceeds, the width of the coupling laser. At this

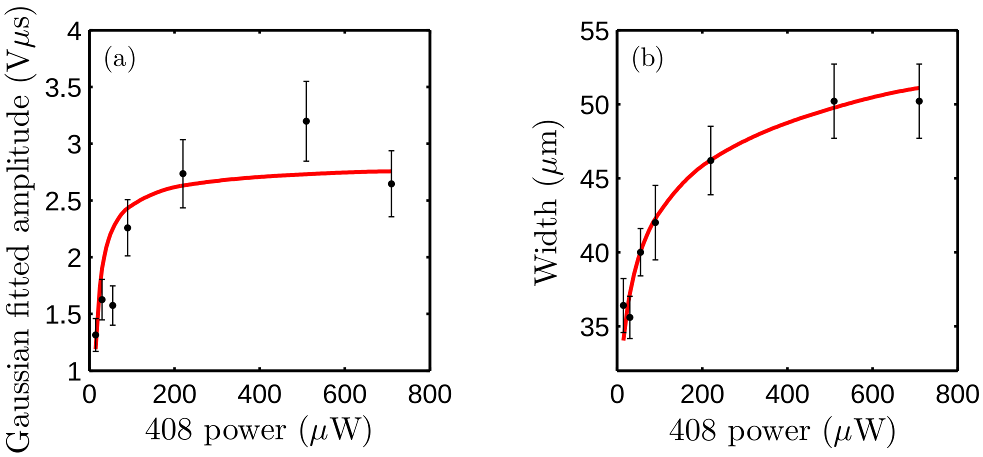

Figure 5.25: (a) The Gaussian fitted amplitude of the spatial distribution of the focused coupling laser with autoionizing laser power. (b) The Gaussian fitted $1/e^2$ width of the spatial distribution of the focused coupling laser as a function of autoionizing laser power. The red, solid lines are the solution to the model described in the text.

point all the Rydberg atoms are being ionized so the signal cannot increase further.

To model the amplitude and width data a simulation similar to the one used to model the spatial width variation as a function of coupling laser power was used. The simulation was simplified as the OBE was not calculated and the Rydberg spatial distribution was assumed to be a two-dimensional Gaussian, i.e. in the low coupling power/linear excitation regime. The autoionization probability, which was a simple Gaussian in the previous simulation, is multiplied by equation 5.4 to create the flat topped probability distribution described above. The absorption cross-section is the same as in section 5.2. The photon fluence is calculated in the same way as well. The clear increase in width with autoionizing power indicates that to get the best resolution with the autoionization microscopy technique the peak intensity of the autoionizing beam should be below the saturated limit.

Conclusion

In this chapter the lens design for creating a diffraction limited spot of waist size 6.3 ± 0.1 μm at a distance of 196 mm has been described. The lens design was used to focus an autoionizing laser to obtain spatial resolution measurements of a Rydberg ensemble. The high intensity of the autoionizing laser reached unit probability of excitation to the doubly excited state allowing characterization of our ion collection/detection apparatus.

A similar lens design also focused the Rydberg coupling laser allowing the high coupling Rabi frequency regime to be studied. The effect on the spectrum of the two-photon resonance was pronounced and a modification to the OBE simulation had to be incorporated. The Gaussian intensity distribution of the coupling laser had to be taken into account in the modified OBE simulation.

The spatial distribution of the Rydberg atoms was measured using the autoionizing scanning microscopy technique. The technique exhibited very good signal-to-noise and signal-to-spontaneous ionization ratios. The width of the measured Rydberg spatial distribution was shown to depend on the Rabi frequency of the coupling laser and the intensity of the autoionizing laser.

Counting the individual ion events in each experimental sequence means the statistics can be studied. The fluctuations seen are super-Poissonian indicating fairly large shot to shot fluctuations in Rydberg atom number, caused by fluctuations in ground state atom number, laser power fluctuations, and laser detuning fluctuations. Access to the count statistics will allow observation of the reduction of the Mandel Q-parameter when the blockade is achieved.

Autoionization is state selective, therefore the spatial position of states created by collisions/interactions could be measured using the autoionization microscopy technique. Temporal dynamics could also be studied due to the rapidity with which the states autoionize.

Chapter 6

Experiments on the 5s75d ^{1}D$_2$ state

In the previous chapter the spatial distribution of the 5s56d ^{1}D$_2$ state was measured using autoionizing microscopy. In this chapter we will increase the principal quantum number, n, to attempt to reach the dipole blockade regime. With a larger n the polarizability of the state also escalates. We will use the large polarizability to shape the excitation volume of the Rydberg ensemble using the Stark effect.

The highest 5snd ^{1}D$_2$ state we can access with a stable locking signal is the $n = 75$ state, see section 3.4.4. To do experiments on the 5s75d ^{1}D$_2$ using the autoionizing transition, the autoionizing spectrum first needs to be measured as no data for such high-lying states has been found in the literature. The spectrum is important as we need to know the detuning of the autoionizing laser to maximize the ion yield.

To take the spectrum the coupling laser is locked on resonance and 1000 averages of the experiment are taken using the same timing sequence as in figure 4.12. The probe and coupling laser powers are kept low, 98 μW and 40 μW respectively, to stay in the linear excitation regime. For all experiments in this chapter the coupling laser is focused to the same spot size described in section 5.3. The autoionizing laser is not focused for this experiment. The wavelength of the autoionizing laser is changed between experiments, using a combination of the grating, current and temperature, and is measured on the wavemeter. The spectrum is shown in figure 6.1a with the average ion signal normalised by autoionizing laser beam power. The width of the spectrum is $\approx$ 20 GHz, compared to $\approx$ 50 GHz for the spectrum of the 5s56d ^{1}D$_2$ state shown in figure 4.11b. The change in width is in line with the n^{-3} scaling predicted and seen in previous experiments [170] when $n \gg l$. For the rest of the experiments in this chapter a detuning of -6 GHz with respect to the unperturbed $5s^+_{1/2} \rightarrow 5p^+_{3/2}$ ion transition is used, giving a maximum ion yield.

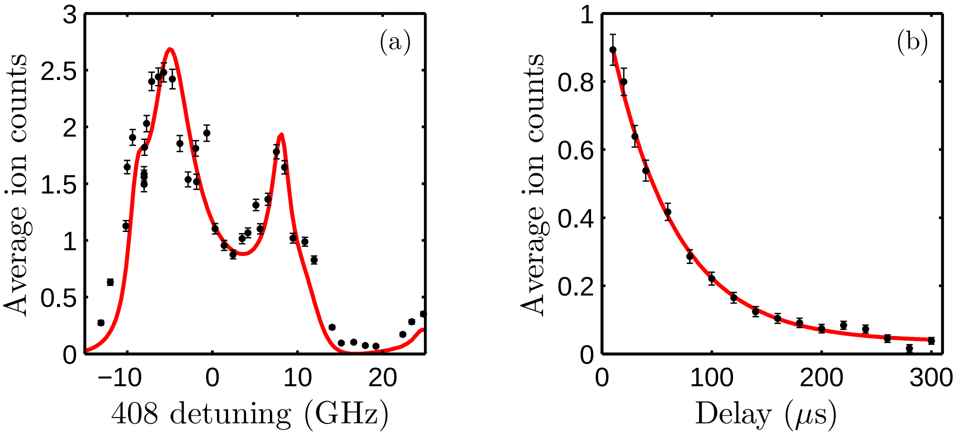

Figure 6.1: (a) Autoionizing spectrum of the 5s75d ^{1}D$_2$ state. Detuning is from the unperturbed $5s^+_{1/2} \rightarrow 5p^+_{3/2}$ ion transition. The red, solid line is a six channel MQDT fit by J. Millen [46]. (b) Ion signal as a function of delay time between excitation laser pulse and the autoionizing laser pulse. The red, solid line is an exponential fit.

To make sure that the 5s75d ^{1}D$_2$ state was being populated instead of another, close lying Rydberg state, the lifetime was measured to check whether it follows the n^3 scaling for Rydberg state lifetimes [3]. The lifetime of the 5s75d ^{1}D$_2$ state was measured by fixing the detuning of the autoionizing laser and delaying when the autoionizing pulse occurred relative to the excitation pulses. The electric field pulse used to direct the ions towards the MCP always happened 100 ns after the autoionizing laser pulse. The autoionizing laser beam was not focused to measure the lifetime to avoid the problem of the atoms moving out of the laser beam during the delay time.

The average ion signal with delay time between the excitation pulse and the autoionizing pulse is shown in figure 6.1b. The exponential fit gives a lifetime of (59 ± 3) μs. We previously measured the lifetime of the 5s56d $^1D_2$ state to be (24.0 ± 1.1) μs [48]. The lifetime of the 5s75d $^1D_2$ state agrees within error with the scaling law applied to the 5s56d $^1D_2$ state.

6.1 Trying to reach the dipole blockade

To test for the dipole blockade the average Rydberg signal as a function of ground state density was measured. The autoionizing laser is once again focused to the waist described in section 5.1, with the focus overlapped with the coupling laser at the centre of the Gaussian MOT cloud, i.e. at the highest ground state density. The coupling laser is locked on resonance and 1000 averages are taken at each density with the timing sequence shown in figure 4.12. The ground state density is varied by changing the power of the Zeeman slowing beam. Five camera images are taken to calculate the density and provide the standard error. The repump lasers are used for this experiment. Again, the probe and coupling laser powers are kept weak to avoid Autler-Townes splitting, with powers of 100 μW and 22 μW respectively. The result is shown in figure 6.2.

The Rydberg signal clearly follows a linear trend with ground state density indicating a non-interacting Rydberg cloud. If there were interactions present then the Rydberg signal should saturate with ground state density [24] as more atoms are in the blockade radius which cannot be excited. Fitting a

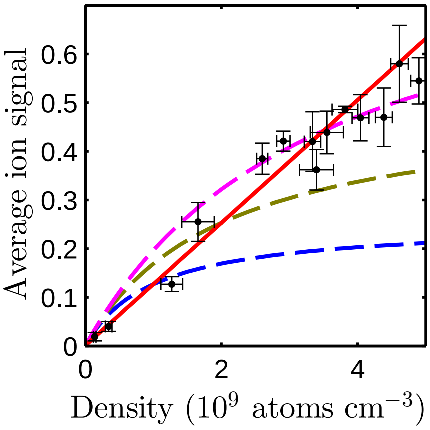

Figure 6.2: The ion signal of the 5s75d ^{1}D$_2$ state as a function of ground state density. The red, solid line is a linear fit to the data. The blue, dashed line is a saturation function plotted using the calculated C_6 and the spectrum fitted linewidth, based upon the model in [24]. The green, dashed and magenta, dashed lines are also saturation fits using a blockade density 2 and 3.5 times the one based upon the calculated C_6.

saturation curve to the data gives a reduced χ^2 slightly worse than the linear case, 1.97 compared to 1.87, indicating the purely linear fit is slightly a better model. The saturation fit gives a saturation density of 5×10^{10} atoms cm^{-3}, much higher than the density available in the current setup of the experiment. However, as no saturation of the data is seen, the error on the fitted saturation value is quite large.

The blockade density, as calculated from the angular average of the C_6, and the laser linewidth of approximately 8 MHz, is 1×10^9 atoms cm^{-3}. The saturation function shown in figure 6.2 is based upon this density. The amplitude of the saturation plot is normalised to have the same amplitude as the measured Rydberg signal at the calculated blockade density, since this is the density where there is one atom on average per blockade radius.

The discrepancy between the measured data and the Rydberg signal saturation curve based upon the calculated C_6 value could be caused by several factors. The most likely problem is that the ground state atomic density measurement is incorrect. The density measurement is based upon a camera image for two of the axes, however, the third axis is a geometric mean of these two measurements. Therefore, the quoted density could quite easily be wrong. The green and magenta dashed lines in figure 6.2 show saturation curves with different blockade densities. These are equivalent to having the measured density being wrong by the same factor. The magenta, dashed line fit the data quite well, however the reduced χ^2 is worse than the linear fit. Measurements of the exact atomic density are difficult due to systematic errors in CCD camera/imaging system calibration, imaging light intensity, and reabsorption of photons in dense MOTs [110], therefore, errors of a factor of two or three in the measured density are possible.

The calculated Rydberg C_6 values for strontium have never been experimentally verified and could therefore be incorrect. However, the computer programs used to calculate C_6 values for strontium have been used to calculate C_6 values for rubidium and agree with other calculations and experimental results, so are unlikely to be far from the correct value.

There is also a slight ambiguity as to the actual densities being compared. The formula for the blockade radius, equation 2.5, assumes a hard-edged blockade sphere, whereas in practice the broadening mechanisms, γ_b, all have Gaussian/Lorentzian lineshapes. These lineshapes therefore have to be cut off somewhere to calculate a blockade radius and depending upon the choice of where to cut the blockade radius can change.

The small difference between measured density and the blockade density mean we are very close to the blockaded regime. Using the maximum measured density and the calculated C_6, there should be 1.8 atoms on average within a blockade radius. Clearly the strongly interacting regime, with many atoms within a blockade radius, cannot be reached in the current setup.

Outlook for studying dipole-dipole interactions

Neglecting the discrepancy between the measured density and the blockade density as calculated from the C_6 coefficient, there are several reasons why the dipole blockade could not be seen. The main problem is that the ground state density could not be made high enough. For the cooling transition used we are limited by the Doppler temperature and the reabsorption of photons emitted by cooled atoms creating an effective outward radiation pressure [110].

The second most important problem is that of the linewidth of the coupling laser being quite broad due to the small locking signal. The laser linewidth is then the limiting factor for the blockade radius, equation 2.5, decreasing the blockade radius/increasing the required ground state density. Though due to the scaling with linewidth, halving the linewidth would only increase the blockade radius by 12 %, therefore a large narrowing of the linewidth would be necessary.

The angular average is also a problem, with the contribution of the Förster zero, $|+2,-2\rangle$ state, to the C_6 decreasing the interaction strength. The angular average only reduces the interaction strength by approximately a factor of two so this is only a minor problem.

Although dipole-dipole interactions were not seen in the current experimental setup, the issues that inhibited the observation of the interactions can all be addressed, though not for results in this thesis. The density of the ground state is limited by the linewidth of the cooling transition. There is a second cooling transition available in strontium, that of the 5s^2 ^{1}S$_0$ $\rightarrow$ 5s5p ^{3}P$_1$, see figure 4.4. The linewidth of this transition is 7.5 kHz, leading to a much lower temperature, ≈ 1 μK, and much higher density, $\approx 10^{12}$ atoms cm^{-3}. To use the intercombination cooling transition, the atoms have to be initially cooled and trapped in the 461 nm cooling transition otherwise the thermal velocity of the atoms is too high to be captured. The two-stage cooling scheme is used in several cold strontium experiments [116, 117, 171].

As mentioned in section 3.4 the setup used to generate the locking signal for the coupling laser means there is not enough bandwidth to have sufficient feedback to narrow the frequency of the laser. To narrow the laser a transfer cavity lock could be implemented [172], allowing high bandwidth feedback via Pound-Drever-Hall locking [103].

To bypass the problem of the angular dependence of the Rydberg state causing a reduction of the interaction strength, the spatially isotropic 5sns ^{1}S$_0$ states could be used. This series has an attractive interaction. The nearly spatially isotropic 5sns ^{3}S$_1$ states, however, have a repulsive interaction [46, 50]. The 5sns ^{3}S$_1$ states could be populated using a probe beam derived from the laser used to create the narrow linewidth MOT, and a coupling beam based on sum frequency generation of two infra-red lasers, with the output frequency doubled to reach the required wavelength [173].

6.2 Excitation region shaping using the Stark effect

The gargantuan polarizability of Rydberg states means they are ideal for sensitive electrometry measurements [35, 174] as the electric field shifts the Rydberg state out of resonance with the laser fields. The autoionization microscopy technique developed in this thesis can be applied to measure electric field inhomogeneities. To illustrate the suitability of the autoionization microscopy technique as a spatial electrometry technique we applied an electric field gradient over the Rydberg ensemble. The split ring electrode pair described in chapter 4 is used to generate the electric field gradient. The electrode setup is shown in figure 6.3a. The electric field this electrode geometry creates is shown in figure 6.3b. The electric field gradient is very close to linear over the centre of the chamber where the MOT forms. The electric field at ± 500 μm, i.e. approximately the MOT width, is ± 50 mV cm^{-1}. Using the single electron model to calculate the polarizability of the individual m_J components and the decomposition described in section 4.7.2, the shift of the 5s75d ^{1}D$_2$ state is 4.3 MHz.

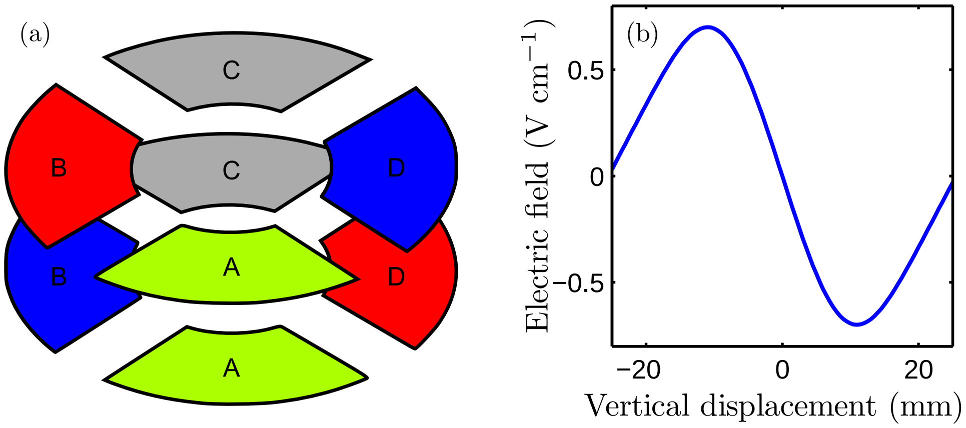

Figure 6.3: (a) Electrode geometry for the generation of a gradient electric field. On electrode pair B and D, red electrodes correspond to positive voltage and blue electrodes equal but opposite voltage. Pair A and C are grounded during Rydberg excitation pulse and are then used to direct charge towards the MCP. (b) The electric field pointing from D to B as a function of vertical position created by geometry shown in (a).

The effect on the Rydberg spatial distribution upon applying an electric field gradient during Rydberg excitation are shown in figure 6.4, where the average ion signals have been normalised for easy comparison. The FWHM of the Gaussian profile fitted to the Rydberg spatial distributions with and without an applied electric field gradient are (780 ± 70) μm and (1010 ± 140) μm respectively, consistent with the shift calculated from the electric field and polarizability. There is a clear reduction in the width when the electric field is applied, indicating that the autoionization microscopy technique is applicable to measuring small spatially varying electric fields. The profile of the Rydberg distribution with an electric field applied is not exactly Gaussian as the frequency shift is proportional to the electric field squared. However, fitting

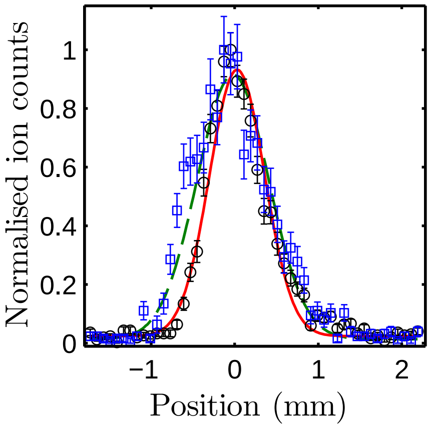

Figure 6.4: Spatial distribution of the Rydberg atoms, without (blue squares with a green, dashed line) and with (black circles with a red, solid line) an electric field gradient applied. The power of both the probe and coupling beams was 100 μW. The experimental sequence is the same as for the spatial distribution measurements described in chapter 5, except that the electric field is applied during the Rydberg excitation in the same manner as the Stark map measurement of section 4.7.2. The lines are Gaussian fits to the data.

a Gaussian is an acceptable method of acquiring a width to the distribution for comparison purposes. As with the dipole interaction measurements a narrower laser would allow higher resolution for mapping the electric field.

Conclusion

Van der Waals interactions were not seen in our system even with an increase in n up to 75. There are several reasons for this: a relatively low ground state density; a relatively broad laser linewidth decreasing the blockade radius and limiting the highest n state we could access to $n = 75$; and angular effects between the Rydberg atoms reducing the interaction strength. Solutions to these problems are currently under investigation.

By applying an inhomogeneous electric field to the Rydberg ensemble we can alter the Rydberg distribution relative to the ground state distribution.

Being able to detect small changes in electric field shows the autoionizing microscopy technique would be a sensitive spatial electrometry tool.

Chapter 7

Discussion and outlook

In this thesis the first measurements of the spatial distributions of Rydberg atoms in a cold, dilute gas of strontium atoms using autoionizing microscopy were presented.

To facilitate these measurements a reliable, flexible source of cold strontium atoms was used. A magneto-optical trap (MOT) loaded from a Zeeman slowed atomic beam creates a confined gas of 3×10^7 strontium atoms at a maximum density of 6×10^9 atoms cm^{-3} and a temperature of 5 mK, when repumped out of the meta-stable 5s5p $^3P_2$ state. The MOT forms the base for all our cold atoms experiments.

For the creation of the MOT a laser system that is frequency stabilized to an atomic resonance was required. Several methods of frequency stabilization of the ground state to first excited state, 5s^2 $^1S_0 \rightarrow$ 5s5p $^1P_1$, transition have been investigated and characterized: two modulation-free techniques, those of polarization spectroscopy and sub-Doppler dichroic atomic vapour laser locking (SDDAVLL) [92]; and two modulation based techniques, frequency modulation spectroscopy and modulation transfer spectroscopy. Due to experimental considerations FM spectroscopy was used to frequency stabilize the laser addressing this transition for the results in this thesis. The stability of FM was better than 1 MHz per hour drift, measured using the cold atoms, easily good enough for MOT creation, day-to-day.

To excite ground state atoms to high lying Rydberg states a resonant, two-photon, three-level, ladder scheme is used as this allows use of visible wavelength lasers. The first photon is resonant with the transition described above. To frequency stabilize the laser addressing the upper transition a novel, electromagnetically-induced transparency based scheme is implemented [83]. Both frequency modulation of the probe (demodulated using an electronic mixer) and amplitude modulation of the coupling laser (demodulated using a lock-in amplifier) are required to generate an error signal large enough to lock. To our knowledge this is the first time this scheme has been used in a non-alkali element. Unfortunately the use of the lock-in amplifier restricts the available bandwidth of the feedback electronics meaning no frequency narrowing can be implemented, leaving a relatively broad laser linewidth. The probe and coupling lasers used to excite atoms from the ground state to Rydberg states are therefore phase stable, enabling coherent excitation.

Both frequency stabilization schemes occur simultaneously in the same novel, dispenser-based vapour cell [90]. Both lasers remain locked for several hours, even when addressing the 5s75d $^1D_2$ state.

Coherent excitation of Rydberg atoms in the cold atoms means we can achieve CPT spectra with FWHM of 3.7 ± 0.2 MHz for the 5s56d $^1D_2$ state, compared to an intermediate state linewidth of 32 MHz. Similar setups with rubidium have measured linewidths down to a couple of hundred kiloHertz [83], though the intermediate state linewidth in that system is only 6 MHz, therefore our setup compares favourably, even without frequency narrowing. The coherent excitation represents a significant improvement to the spectral resolution we can attain compared to the “step-scan” technique previously used [46].

Simulation of the population dynamics using an optical Bloch equation model gave very good agreement with measured spectra. The OBE model indicated the measured spectral width was due to finite laser linewidth. Unfortunately the relative linewidth of the two lasers used to excite to Rydberg states is too broad and the ground state density too low to observe dipole-dipole interaction effects.

The OBE model and knowledge of experimental parameters allows us to calibrate our detection apparatus, giving a detection efficiency of 0.21 ± 0.04. This detection efficiency is entirely reasonable due to the inherent efficiency of the MCP and mesh grid surrounding the MCP.

Building upon previous work, where we have used an autoionizing transition in strontium to measure temporal [47] and spectral [48] dynamics of Rydberg states, we can now probe the spatial distributions.

The autoionizing laser beam was focused to a 10 μm waist and translated across the Rydberg excitation volume to obtain Rydberg spatial distributions with very good signal-to-noise and signal-to-background ratios. This is a new method of measuring the spatial distribution of Rydberg atoms, which we have called autoionization microscopy. The achieved resolution is comparable to other Rydberg spatial measurements [41, 144]. Measured variations from the ground state distribution were simulated and explained using the OBE model.

The counting of ions at each spatial position for each repetition of the experiment allows access to the count statistics of the distributions. Analysis of these statistics shows that the distributions have super-Poissonian nature, implying that there are significant Rydberg atom number fluctuations. These fluctuations are problematic as they are causing the majority of the error on our measurements. The fluctuations are most likely caused by variations in the power and detuning of the excitation lasers, indicating better laser locks would reduce them.

The large polarizability associated with high n states was employed to shape the Rydberg state spatial distribution. A gradient electric field was applied across the ensemble with the wings of the ensemble Stark shifted out of resonance. Autoionization microscopy was used to observe the modification to the Rydberg state spatial distribution. The spatial resolution and frequency shift resolution available in the autoionization microscopy technique are comparable to other atomic systems used to measure spatial electrometry [35].

Outlook

The autoionization microscopy technique developed in this thesis can be extended to look at dipole-dipole interactions by increasing the density of the ground state atoms using a second stage of cooling on the intercombination transition. The increase in density should be approximately two orders of magnitude, putting the experiment in the strongly interacting regime. By controlling the excitation beam parameters carefully, exotic states, such as dynamical crystals, could be generated and measured.

The limit of resolution for the autoionization microscopy technique was the requirement of the lens system to be external to the vacuum chamber. Situating high numerical aperture aspheric lenses inside the vacuum chamber, close to the atoms would increase the resolution. Tests carried out on available lenses indicate that resolutions down to 1 μm are feasible.

Combining the spatial resolution developed in this thesis with the spectral and temporal measurements previously made could allow us to study state transfer reactions spatially within the Rydberg ensemble.

The simple improvements to the cold atom setup and the spatial resolution indicate that the autoionization microscopy technique is a good candidate for measuring interaction-based spatial correlations. The main drawbacks of the technique are the time taken to measure a Rydberg spatial distribution and the inability to measure the correlations in a single experimental shot.

Appendix A

Circuit diagrams

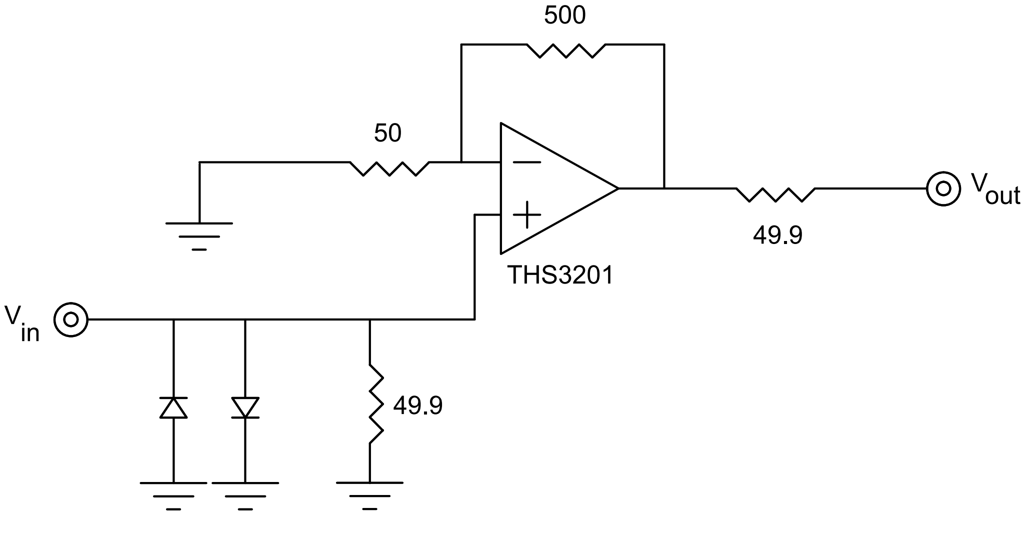

Figure A.1: MCP first stage amplifier.

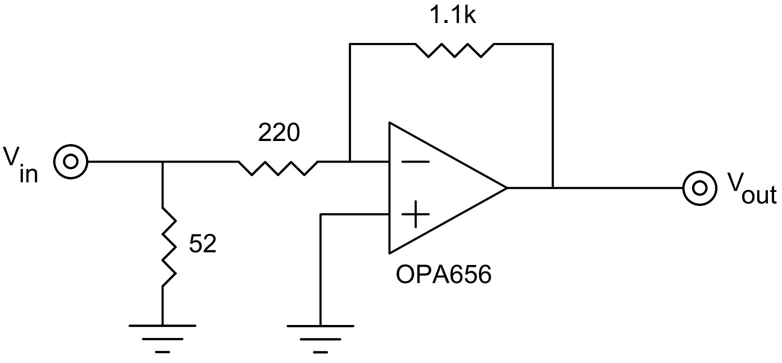

Figure A.2: MCP second stage amplifier.

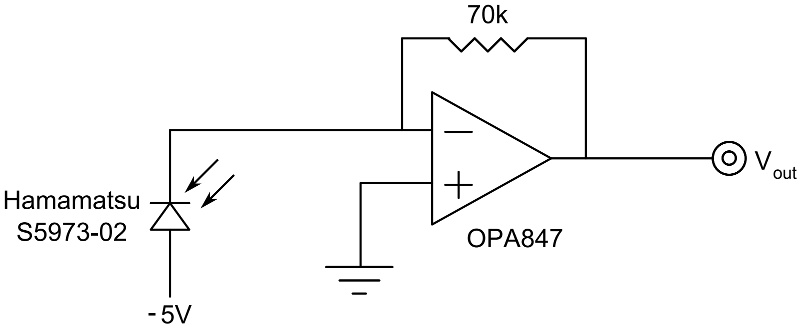

Figure A.3: Transimpedance photodiode.

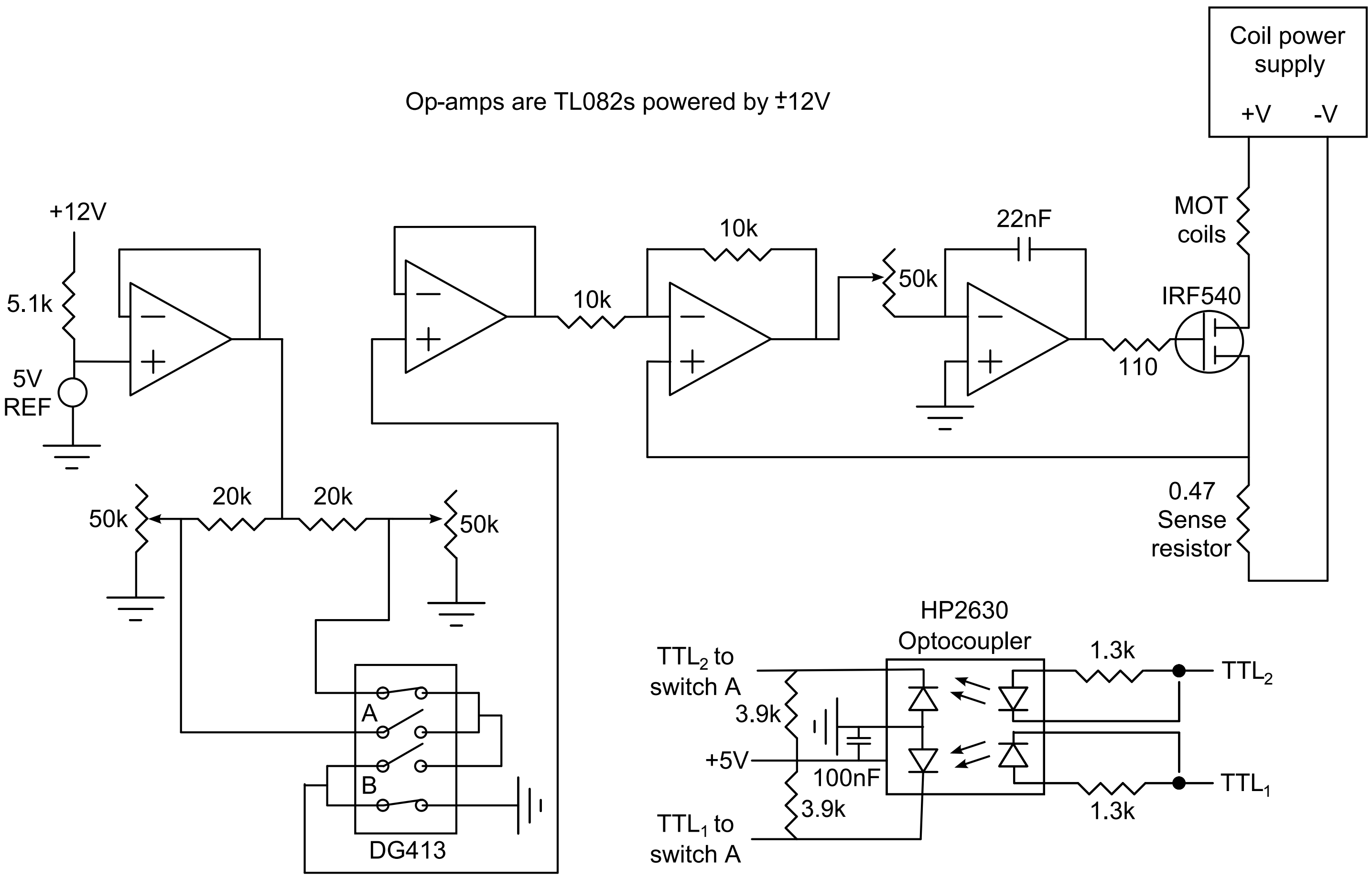

Figure A.4: MOT coil switch.

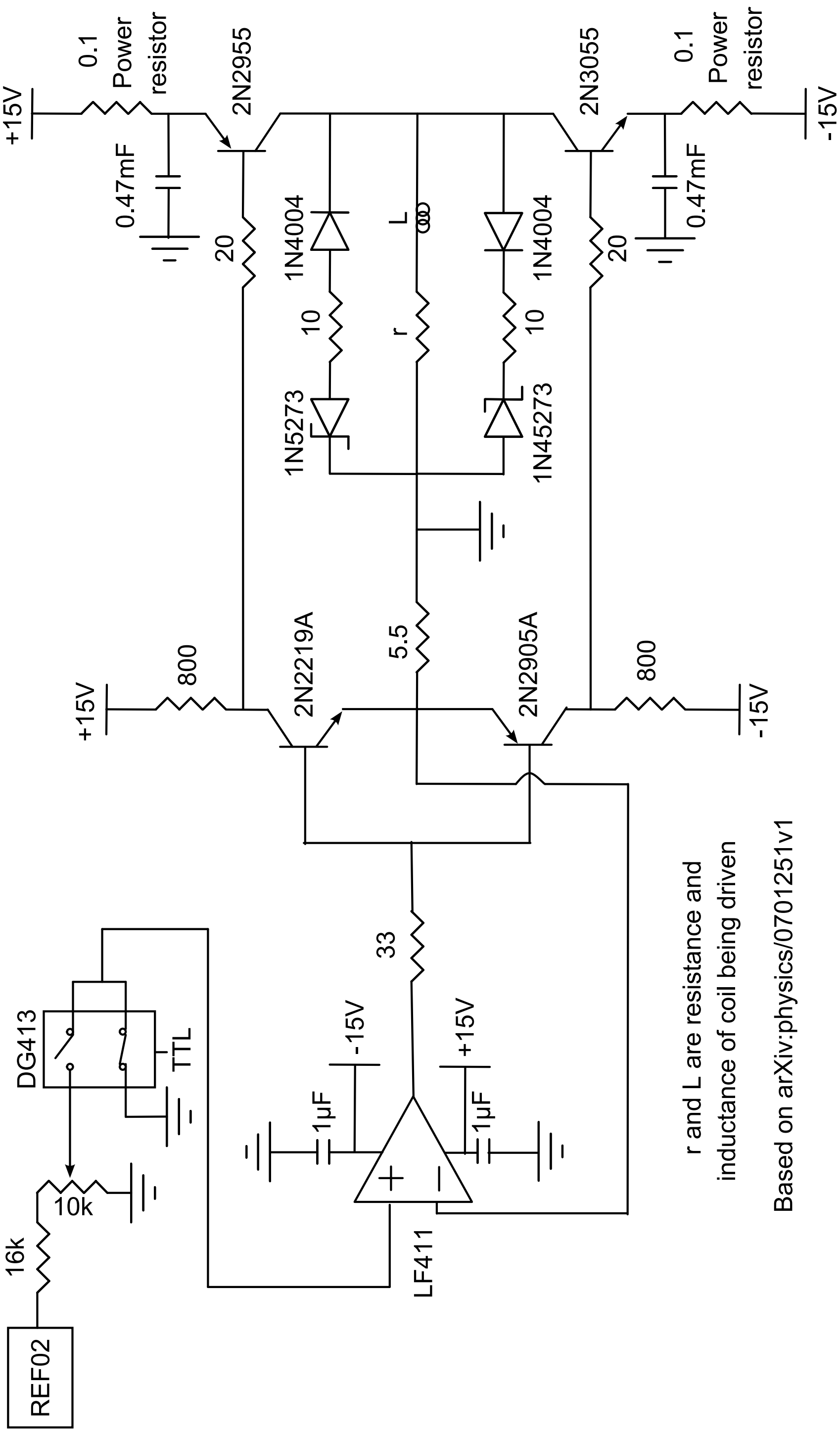

r and L are resistance and inductance of coil being driven

Based on arXiv:physics/0701251v1

Figure A.5: Bipolar coil driver based on design from [175].

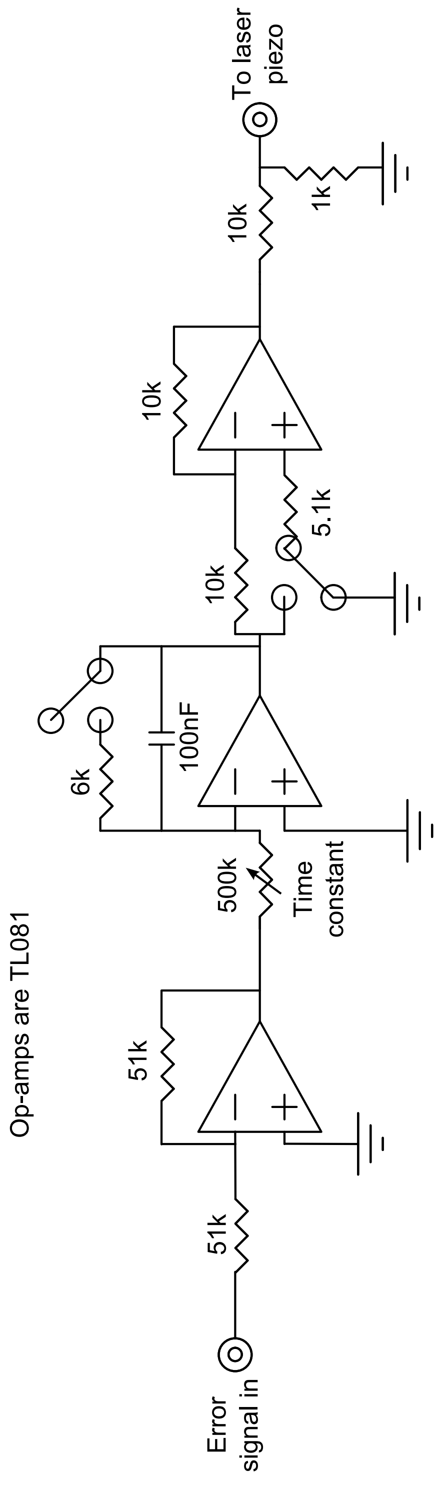

Figure A.6: Laser locking circuit.

Bibliography

[1] W. E. Cooke, T. F. Gallagher, S. A. Edelstein, and R. M. Hill, *Doubly Excited Autoionizing Rydberg States of Sr*, Phys. Rev. Lett. **40**, 178 (1978).

[2] J. Rydberg, *On the structure of the line-spectra of the chemical elements*, Philosophical Magazine Series 5 **29**, 331 (1890).

[3] T. Gallagher, *Rydberg Atoms*, First ed. (Cambridge University Press, 1995).

[4] A. L. Schawlow and C. H. Townes, *Infrared and Optical Masers*, Phys. Rev. **112**, 1940 (1958).

[5] D. Meschede, H. Walther, and G. Müller, *One-Atom Maser*, Phys. Rev. Lett. **54**, 551 (1985).

[6] M. Brune, J. M. Raimond, P. Goy, L. Davidovich, and S. Haroche, *Realization of a two-photon maser oscillator*, Phys. Rev. Lett. **59**, 1899 (1987).

[7] S. Chu, *Nobel Lecture: The manipulation of neutral particles*, Rev. Mod. Phys. **70**, 685 (1998).

[8] C. N. Cohen-Tannoudji, *Nobel Lecture: Manipulating atoms with photons*, Rev. Mod. Phys. **70**, 707 (1998).

[9] W. D. Phillips, *Nobel Lecture: Laser cooling and trapping of neutral atoms*, Rev. Mod. Phys. **70**, 721 (1998).

[10] T. Killian, T. Pattard, T. Pohl, and J. Rost, *Ultracold Neutral Plasmas*, Physics Reports **449**, 77 (2007).

[11] A. Mohapatra, M. Bason, B. Butscher, K. Weatherill, and C. Adams, *A giant electro-optic effect using polarizable dark states*, Nature Physics **4**, 890 (2008).

[12] V. Bendkowsky *et al.*, *Observation of ultralong-range Rydberg molecules*, Nature **458**, 1005 (2009).

[13] J. J. Mestayer *et al.*, *Realization of Localized Bohr-Like Wave Packets*, Phys. Rev. Lett. **100**, 243004 (2008).

[14] D. Jaksch *et al.*, *Fast Quantum Gates for Neutral Atoms*, Phys. Rev. Lett. **85**, 2208 (2000).

[15] M. Saffman, T. G. Walker, and K. Mølmer, *Quantum information with Rydberg atoms*, Rev. Mod. Phys. **82**, 2313 (2010).

[16] M. D. Lukin *et al.*, *Dipole Blockade and Quantum Information Processing in Mesoscopic Atomic Ensembles*, Phys. Rev. Lett. **87**, 037901 (2001).

[17] F. Robicheaux and J. V. Hernández, *Many-body wave function in a dipole blockade configuration*, Phys. Rev. A **72**, 063403 (2005).

[18] A. Gaëtan *et al.*, *Observation of collective excitation of two individual atoms in the Rydberg blockade regime*, Nature Physics **5**, 115 (2009).

[19] E. Urban *et al.*, *Observation of Rydberg blockade between two atoms*, Nature Physics **5**, 110 (2009).

[20] T. Wilk *et al.*, *Entanglement of Two Individual Neutral Atoms Using Rydberg Blockade*, Phys. Rev. Lett. **104**, 010502 (2010).

[21] L. Isenhower *et al.*, *Demonstration of a Neutral Atom Controlled-NOT Quantum Gate*, Phys. Rev. Lett. **104**, 010503 (2010).

[22] D. Tong *et al.*, *Local Blockade of Rydberg Excitation in an Ultracold Gas*, Phys. Rev. Lett. **93**, 063001 (2004).

[23] U. Raitzsch *et al.*, *Echo Experiments in a Strongly Interacting Rydberg Gas*, Phys. Rev. Lett. **100**, 013002 (2008).

[24] H. Schempp *et al.*, *Coherent Population Trapping with Controlled Interparticle Interactions*, Phys. Rev. Lett. **104**, 173602 (2010).

[25] J. D. Pritchard *et al.*, *Cooperative Atom-Light Interaction in a Blockaded Rydberg Ensemble*, Phys. Rev. Lett. **105**, 193603 (2010).

[26] M. Saffman and T. G. Walker, *Creating single-atom and single-photon sources from entangled atomic ensembles*, Phys. Rev. A **66**, 065403 (2002).

[27] A. V. Gorshkov, J. Otterbach, M. Fleischhauer, T. Pohl, and M. D. Lukin, *Photon-Photon Interactions via Rydberg Blockade*, Phys. Rev. Lett. **107**, 133602 (2011).

[28] Y. Dudin and A. Kuzmich, *Strongly Interacting Rydberg Excitations of a Cold Atomic Gas*, Science **336**, 887 (2012).

[29] D. Maxwell *et al.*, *Coherent control of strongly interacting Rydberg polaritons*, **arXiv:1207.6007v1** (2012).

[30] T. Pohl, E. Demler, and M. D. Lukin, *Dynamical Crystallization in the Dipole Blockade of Ultracold Atoms*, Phys. Rev. Lett. **104**, 043002 (2010).

[31] R. M. W. van Bijnen, S. Smit, K. A. H. van Leeuwen, E. J. D. Vredenbregt, and S. J. J. M. F. Kokkelmans, *Adiabatic formation of Rydberg*

crystals with chirped laser pulses, Journal of Physics B: Atomic, Molecular and Optical Physics **44**, 184008 (2011).

[32] R. Mukherjee, J. Millen, R. Nath, M. P. A. Jones, and T. Pohl, *Many-body physics with alkaline-earth Rydberg lattices*, Journal of Physics B: Atomic, Molecular and Optical Physics **44**, 184010 (2011).

[33] D. Greenberger, M. Horne, and A. Zeilinger, *Bell's Theorem, Quantum Theory, and Conceptions of the Universe*, First ed. (Kluwer, 1989).

[34] A. Tauschinsky, C. S. E. van Ditzhuijzen, L. D. Noordam, and H. B. v. L. van den Heuvell, *Radio-frequency-driven dipole-dipole interactions in spatially separated volumes*, Phys. Rev. A **78**, 063409 (2008).

[35] A. Tauschinsky, R. M. T. Thijssen, S. Whitlock, H. B. van Linden van den Heuvell, and R. J. C. Spreeuw, *Spatially resolved excitation of Rydberg atoms and surface effects on an atom chip*, Phys. Rev. A **81**, 063411 (2010).

[36] M. Piotrowicz *et al.*, *Measurement of the electric dipole moments for transitions to rubidium Rydberg states via Autler–Townes splitting*, New Journal of Physics **13**, 093012 (2011).

[37] G. Günter *et al.*, *Interaction Enhanced Imaging of Individual Rydberg Atoms in Dense Gases*, Phys. Rev. Lett. **108**, 013002 (2012).

[38] J. Sherson *et al.*, *Single-atom-resolved fluorescence imaging of an atomic Mott insulator*, Nature **467**, 68–72 (2010).

[39] W. Bakr, J. Gillen, A. Peng, S. Fölling, and M. Greiner, *A quantum gas microscope for detecting single atoms in a Hubbard-regime optical lattice*, Nature **462**, 74–77 (2009).

[40] P. Schauß *et al.*, *Observation of mesoscopic crystalline structures in a two-dimensional Rydberg gas*, **arXiv:1209.0944v1** (2012).

[41] A. Schwarzkopf, R. E. Sapiro, and G. Raithel, *Imaging Spatial Correlations of Rydberg Excitations in Cold Atom Clouds*, Phys. Rev. Lett. **107**, 103001 (2011).

[42] S. Sevinçli, N. Henkel, C. Ates, and T. Pohl, *Nonlocal Nonlinear Optics in Cold Rydberg Gases*, Phys. Rev. Lett. **107**, 153001 (2011).

[43] F. Maucher *et al.*, *Rydberg-Induced Solitons: Three-Dimensional Self-Trapping of Matter Waves*, Phys. Rev. Lett. **106**, 170401 (2011).

[44] G. Pupillo, A. Micheli, M. Boninsegni, I. Lesanovsky, and P. Zoller, *Strongly Correlated Gases of Rydberg-Dressed Atoms: Quantum and Classical Dynamics*, Phys. Rev. Lett. **104**, 223002 (2010).

[45] H. Weimer, M. Müller, I. Lesanovsky, P. Zoller, and H. Büchler, *A Rydberg quantum simulator*, Nature Physics **6**, 382 (2010).

[46] J. Millen, *A cold strontium Rydberg gas*, PhD thesis, Durham University, 2011.

[47] J. Millen, G. Lochead, G. R. Corbett, R. M. Potvliege, and M. P. A. Jones, *Spectroscopy of a cold strontium Rydberg gas*, Journal of Physics B: Atomic, Molecular and Optical Physics **44**, 184001 (2011).

[48] J. Millen, G. Lochead, and M. P. A. Jones, *Two-Electron Excitation of an Interacting Cold Rydberg Gas*, Phys. Rev. Lett. **105**, 213004 (2010).

[49] P. Esherick, *Bound, even-parity $J = 0$ and $J = 2$ spectra of Sr*, Phys. Rev. A **15**, 1920 (1977).

[50] C. Vaillant, M. Jones, and R. Potvliege, *Long-range Rydberg–Rydberg interactions in calcium, strontium and ytterbium*, Journal of Physics B: Atomic, Molecular and Optical Physics **45**, 135004 (2012).

[51] M. Zhi, C. Dai, and S. Li, *Stark structure of the Rydberg states of alkaline-earth atoms*, Chinese Physics **10**, 929 (2001).

[52] C. Theodosiou, *Lifetimes of alkali-metal-atom Rydberg states*, Phys. Rev. A **30**, 2881 (1984).

[53] K. Sakimoto, *Multichannel quantum-defect theory of the Stark effect*, Journal of Physics B: Atomic and Molecular Physics **19**, 3011 (1986).

[54] K. Singer, J. Stanojevic, M. Weidemüller, and R. Côté, *Long-range interactions between alkali Rydberg atom pairs correlated to the ns–ns, np–np and nd–nd asymptotes*, Journal of Physics B: Atomic, Molecular and Optical Physics **38**, S295 (2005).

[55] T. G. Walker and M. Saffman, *Consequences of Zeeman degeneracy for the van der Waals blockade between Rydberg atoms*, Phys. Rev. A **77**, 032723 (2008).

[56] A. Schwettmann, K. R. Overstreet, J. Tallant, and J. P. Shaffer, *Analysis of long-range Cs Rydberg potential wells*, Journal of Modern Optics **54**, 2551 (2007).

[57] A. Dalgarno and W. Davison, *The Calculation of Van Der Waals Interactions*, **2**, 1 (1966).

[58] T. G. Walker and M. Saffman, *Zeros of Rydberg–Rydberg Föster interactions*, Journal of Physics B: Atomic, Molecular and Optical Physics **38**, S309 (2005).

[59] D. Tong *et al.*, *Local Blockade of Rydberg Excitation in an Ultracold Gas*, Phys. Rev. Lett. **93**, 063001 (2004).

[60] C. Foot, *Atomic Physics*, First ed. (Oxford University Press, 2005).

[61] C. Cohen-Tannoudji, J. Dupont-Roc, and G. Grynberg, *Atom-Photon Interactions*, Fourth ed. (Wiley-VCH, 2004).

[62] K. Blum, *Density Matrix Theory and Applications*, Second ed. (Plenum, 1996).

[63] G. Lindblad, *On the generators of quantum dynamical semigroups*, Comm. Math. Phys. **48**, 119 (1976).

[64] J. Gea-Banacloche, Y.-q. Li, S.-z. Jin, and M. Xiao, *Electromagnetically induced transparency in ladder-type inhomogeneously broadened media: Theory and experiment*, Phys. Rev. A **51**, 576 (1995).

[65] B. Bransden and C. Joachain, *Physics of Atoms and Molecules*, Second ed. (Prentice Hall, 2003).

[66] R. C. Hilborn, *Einstein coefficients, cross sections, f values, dipole moments, and all that*, American Journal of Physics **50**, 982 (1982).

[67] S.-U. Haq *et al.*, *Photoionization cross section and oscillator strength distribution in the near-threshold region of strontium*, Eur. Phys. J. D **44**, 439 (2007).

[68] H. G. C. Werij, C. H. Greene, C. E. Theodosiou, and A. Gallagher, *Oscillator strengths and radiative branching ratios in atomic Sr*, Phys. Rev. A **46**, 1248 (1992).

[69] D. Suter, *The Physics of Laser-Atom Interactions*, First ed. (Cambridge University Press, 1997).

[70] M. Fleischhauer, A. Imamoglu, and J. P. Marangos, *Electromagnetically induced transparency: Optics in coherent media*, Rev. Mod. Phys. **77**, 633 (2005).

[71] K.-J. Boller, Imamolu, A., and S. E. Harris, *Observation of electromagnetically induced transparency*, Phys. Rev. Lett. **66**, 2593 (1991).

[72] U. Fano, *Effects of Configuration Interaction on Intensities and Phase Shifts*, Phys. Rev. **124**, 1866 (1961).

[73] S. H. Autler and C. H. Townes, *Stark Effect in Rapidly Varying Fields*, Phys. Rev. **100**, 703 (1955).

[74] P. M. Anisimov, J. P. Dowling, and B. C. Sanders, *Objectively Discerning Autler-Townes Splitting from Electromagnetically Induced Transparency*, Phys. Rev. Lett. **107**, 163604 (2011).

[75] T. Y. Abi-Salloum, *Electromagnetically induced transparency and Autler-Townes splitting: Two similar but distinct phenomena in two categories of three-level atomic systems*, Phys. Rev. A **81**, 053836 (2010).

[76] A. Kocharovskaya and Y. Khanin, *Population trapping and coherent bleaching of a three-level medium by a periodic train of ultrashort pulses*, Sov. Phys. J.E.T.P. **63**, 945 (1986).

[77] E. Arimondo, *Coherent Population Trapping in Laser Spectroscopy*, Progress in Optics **35**, 257 (1996).

[78] J. R. Kuklinski, U. Gaubatz, F. T. Hioe, and K. Bergmann, *Adiabatic population transfer in a three-level system driven by delayed laser pulses*, Phys. Rev. A **40**, 6741 (1989).

[79] K. Winkler *et al.*, *Coherent Optical Transfer of Feshbach Molecules to a Lower Vibrational State*, Phys. Rev. Lett. **98**, 043201 (2007).

[80] W. Demtröder, *Laser Spectroscopy*, Second ed. (Springer, 1998).

[81] E. Black, *An introduction to Pound-Drever-Hall laser frequency stabilization*, American journal of physics **69**, 79 (2001).

[82] P. J. Slevin and W. W. Harrison, *The Hollow Cathode Discharge as a Spectrochemical Emission Source*, Applied Spectroscopy Reviews **10**, 201 (1975).

[83] R. Abel *et al.*, *Laser frequency stabilization to excited state transitions using electromagnetically induced transparency in a cascade system*, Appl. Phys. Lett. **94**, 071107 (2009).

[84] M. Asano and K. Kubo, *Vapor pressure of strontium below 660 K*, Journal of Nuclear Science and Technology **15**, 765 (1978).

[85] G. D. Maria and V. Piacente, *Vapor pressures of calcium and strontium by transpiration method*, The Journal of Chemical Thermodynamics **6**, 1 (1974).

[86] J. Neuman, P. Wang, and A. Gallagher, *Robust high-temperature sapphire cell for metal vapors*, Rev. Sci. Instrum. **66**, 3021 (1995).

[87] C. R. Vidal and J. Cooper, *Heat-Pipe Oven: A New, Well-Defined Metal Vapor Device for Spectroscopic Measurements*, Journal of Applied Physics **40**, 3370 (1969).

[88] G. Philip, *An atomic jet in a heat pipe for multiphoton spectroscopy*, Rev. Sci. Instrum. **78**, 113101 (2007).

[89] Y. Li, T. Ido, T. Eichler, and H. Katori, *Narrow-line diode laser system for laser cooling of strontium atoms on the intercombination transition*, Applied Physics B: Lasers and Optics **78**, 315 (2004), 10.1007/s00340-004-1405-x.

[90] E. Bridge, J. Millen, C. Adams, and M. Jones, *A vapor cell based on dispensers for laser spectroscopy*, Rev. Sci. Instrum. **80** (2009).

[91] E. R. Eliel, W. Hogervorst, T. Olsson, and L. R. Pendrill, *High resolution laser spectroscopy of low-lying p-states in Sr I and Ba I*, Zeitschrift für Physik A Hadrons and Nuclei **311**, 1 (1983), 10.1007/BF01411600.

[92] C. Javaux, I. Hughes, G. Lochead, J. Millen, and M. Jones, *Modulation-free pump-probe spectroscopy of strontium atoms*, Eur. Phys. J. D **57**, 151 (2010).

[93] M. Harris *et al.*, *Polarization spectroscopy in rubidium and cesium*, Phys. Rev. A **73**, 062509 (2006).

[94] M. Harris, S. Cornish, A. Tripathi, and I. Hughes, *Optimization of sub-Doppler DAVLL on the rubidium D2 line*, Journal of Physics B: Atomic, Molecular and Optical Physics **41**, 085401 (2008).

[95] C. Wieman and T. W. Hänsch, *Doppler-Free Laser Polarization Spectroscopy*, Phys. Rev. Lett. **36**, 1170 (1976).

[96] C. Pearman *et al.*, *Polarization spectroscopy of a closed atomic transition: applications to laser frequency locking*, Journal of Physics B: Atomic, Molecular and Optical Physics **35**, 5141 (2002).

[97] B. Chéron, H. Gilles, J. Hamel, O. Moreau, and H. Sorel, *Laser frequency stabilization using Zeeman effect*, Journal of Physics III **4**, 401 (1994).

[98] K. L. Corwin, Z.-T. Lu, C. F. Hand, R. J. Epstein, and C. E. Wieman, *Frequency-Stabilized Diode Laser with the Zeeman Shift in an Atomic Vapor*, Appl. Opt. **37**, 3295 (1998).

[99] R. Eisberg and R. Resnick, *Quantum Physics of Atoms, Molecules, Solids, Nuclei, and Particles*, Second ed. (John Wiley and Sons, 1985).

[100] G. C. Bjorklund, *Frequency-modulation spectroscopy: a new method for measuring weak absorptions and dispersions*, Opt. Lett. **5**, 15 (1980).

[101] J. H. Shirley, *Modulation transfer processes in optical heterodyne saturation spectroscopy*, Opt. Lett. **7**, 537 (1982).

[102] R. V. Pound, *Electronic Frequency Stabilization of Microwave Oscillators*, Rev. Sci. Instrum. **17**, 490 (1946).

[103] R. Drever *et al.*, *Laser phase and frequency stabilization using an optical resonator*, Applied physics B: Lasers and optics **31**, 97 (1983).

[104] G. Camy, C. Bordé, and M. Ducloy, *Heterodyne saturation spectroscopy through frequency modulation of the saturating beam*, Optics Communications **41**, 325 (1982).

[105] R. K. Raj, D. Bloch, J. J. Snyder, G. Camy, and M. Ducloy, *High-Frequency Optically Heterodyned Saturation Spectroscopy Via Resonant Degenerate Four-Wave Mixing*, Phys. Rev. Lett. **44**, 1251 (1980).

[106] D. McCarron, S. King, and S. Cornish, *Modulation transfer spectroscopy in atomic rubidium*, Measurement science and technology **19**, 105601 (2008).

[107] S. Mauger, J. Millen, and M. Jones, *Spectroscopy of strontium Rydberg states using electromagnetically induced transparency*, Journal of Physics B: Atomic, Molecular and Optical Physics **40**, F319 (2007).

[108] H. Bethe and E. Salpeter, *Quantum Mechanics of One and Two Electron Atoms*, First ed. (Academic Press, New York, 1957).

[109] W. R. Anderson, J. R. Veale, and T. F. Gallagher, *Resonant Dipole-Dipole Energy Transfer in a Nearly Frozen Rydberg Gas*, Phys. Rev. Lett. **80**, 249 (1998).

[110] H. Metclaf and P. van der Straten, *Laser Cooling and Trapping*, First ed. (Springer, 1999).

[111] I. Courtillot *et al.*, *Efficient cooling and trapping of strontium atoms*, Opt. Lett. **28**, 468 (2003).

[112] C. Dedman *et al.*, *Optimum design and construction of a Zeeman slower for use with a magneto-optic trap*, Rev. Sci. Instrum. **75**, 5136 (2004).

[113] E. Raab, M. Prentiss, A. Cable, S. Chu, and D. Pritchard, *Trapping of neutral sodium atoms with radiation pressure*, Phys. Rev. Lett. **59**, 2631 (1987).

[114] X. Xu, T. H. Loftus, J. L. Hall, A. Gallagher, and J. Ye, *Cooling and trapping of atomic strontium*, J. Opt. Soc. Am. B **20**, 968 (2003).

[115] W. Shao-Kai *et al.*, *Cooling and Trapping 88 Sr Atoms with 461 nm Laser*, Chinese Physics Letters **26**, 093202 (2009).

[116] N. Poli *et al.*, *Cooling and trapping of ultracold strontium isotopic mixtures*, Phys. Rev. A **71**, 061403 (2005).

[117] H. Katori, T. Ido, Y. Isoya, and M. Kuwata-Gonokami, *Magneto-Optical Trapping and Cooling of Strontium Atoms down to the Photon Recoil Temperature*, Phys. Rev. Lett. **82**, 1116 (1999).

[118] P. D. Lett *et al.*, *Observation of Atoms Laser Cooled below the Doppler Limit*, Phys. Rev. Lett. **61**, 169 (1988).

[119] K. M. aes *et al.*, *The Escape Velocity in a Magneto-Optical Trap and Its Importance to Trap Loss Investigation*, Laser Physics **12**, 145 (2002).

[120] A. Ludlow, *The Strontium Optical Lattice Clock: Optical Spectroscopy with Sub-Hertz Accuracy*, PhD thesis, University of Colorado, 2008.

[121] M. Yasuda and H. Katori, *Lifetime measurement of the* $^3P_2$ *metastable state of strontium atoms*, Phys. Rev. Lett. **92**, 153004 (2004).

[122] P. G. Mickelson *et al.*, *Repumping and spectroscopy of laser-cooled Sr atoms using the (5s5p) 3 P 2 –(5s4d) 3 D 2 transition*, Journal of Physics B: Atomic, Molecular and Optical Physics **42**, 235001 (2009).

[123] N. Poli *et al.*, *Cooling and trapping of ultracold strontium isotopic mixtures*, Phys. Rev. A **71**, 061403 (2005).

[124] S. B. Nagel *et al.*, *Magnetic trapping of metastable* $^3P_2$ *atomic strontium*, Phys. Rev. A **67**, 011401 (2003).

[125] M. Fleming and A. Mooradian, *Spectral characteristics of external-cavity controlled semiconductor lasers*, Quantum electronics **17**, 44 (1981).

[126] D. Main, *Development and testing of a software-based, wavemeter referenced laser frequency stabilisation system*, Master's thesis, University of Durham, 2011.

[127] R. Löw *et al.*, *Apparatus for excitation and detection of Rydberg atoms in quantum gases*, **arXiv:0706.2639v1** (2007).

[128] M. Poirier, *Autoionization of Rydberg states with large angular momentum: Application to alkaline-earth atoms*, Phys. Rev. A **38**, 3484 (1988).

[129] E. Y. Xu, Y. Zhu, O. C. Mullins, and T. F. Gallagher, *Sr 5pnd J=3 autoionizing series and interference of excitation due to bound-state perturbation*, Phys. Rev. A **35**, 1138 (1987).

[130] R. R. Jones, C. J. Dai, and T. F. Gallagher, *Ba* $6p_j\mathrm{nf}_{j'}$ *autoionizing series*, Phys. Rev. A **41**, 316 (1990).

[131] N. H. Tran, P. Pillet, R. Kachru, and T. F. Gallagher, *Multistep excitation of autoionizing Rydberg states*, Phys. Rev. A **29**, 2640 (1984).

[132] T. F. Gallagher and W. E. Cooke, *Interactions of Blackbody Radiation with Atoms*, Phys. Rev. Lett. **42**, 835 (1979).

[133] I. I. Beterov, D. B. Tretyakov, I. I. Ryabtsev, A. Ekers, and N. N. Bezuglov, *Ionization of sodium and rubidium* nS*,* nP*, and* nD *Rydberg atoms by blackbody radiation*, Phys. Rev. A **75**, 052720 (2007).

[134] T. Amthor, M. Reetz-Lamour, S. Westermann, J. Denskat, and M. Weidemüller, *Mechanical Effect of van der Waals Interactions Observed in Real Time in an Ultracold Rydberg Gas*, Phys. Rev. Lett. **98**, 023004 (2007).

[135] A. Walz-Flannigan, J. R. Guest, J.-H. Choi, and G. Raithel, *Cold-Rydberg-gas dynamics*, Phys. Rev. A **69**, 063405 (2004).

[136] T. Amthor, M. Reetz-Lamour, C. Giese, and M. Weidemüller, *Modeling many-particle mechanical effects of an interacting Rydberg gas*, Phys. Rev. A **76**, 054702 (2007).

[137] M. P. Robinson, B. L. Tolra, M. W. Noel, T. F. Gallagher, and P. Pillet, *Spontaneous Evolution of Rydberg Atoms into an Ultracold Plasma*, Phys. Rev. Lett. **85**, 4466 (2000).

[138] W. Li *et al.*, *Evolution dynamics of a dense frozen Rydberg gas to plasma*, Phys. Rev. A **70**, 042713 (2004).

[139] T. C. Killian *et al.*, *Creation of an Ultracold Neutral Plasma*, Phys. Rev. Lett. **83**, 4776 (1999).

[140] I. Hughes and T. Hase, *Measurements and their Uncertainties*, First ed. (Oxford University Press, 2010).

[141] D. Brink and G. Satchler, *Angular momentum*, Third ed. (Oxford Science Publications, 1993).

[142] G. Lochead, D. Boddy, D. Sadler, C. Adams, and M. Jones, *Number-resolved imaging of excited-state atoms using a scanning autoionization microscope*, **arXiv:1212.3270** (2012).

[143] T. C. Killian *et al.*, *Absorption imaging and spectroscopy of ultracold neutral plasmas*, Journal of Physics B: Atomic, Molecular and Optical Physics **38**, S351 (2005).

[144] C. S. E. van Ditzhuijzen *et al.*, *Spatially Resolved Observation of Dipole-Dipole Interaction between Rydberg Atoms*, Phys. Rev. Lett. **100**, 243201 (2008).

[145] E. Hecht, *Optics*, Fourth ed. (Addison Wesley, 2002).

[146] N. Schlosser, G. Reymond, and P. Grangier, *Collisional Blockade in Microscopic Optical Dipole Traps*, Phys. Rev. Lett. **89**, 023005 (2002).

[147] M. Weber, J. Volz, K. Saucke, C. Kurtsiefer, and H. Weinfurter, *Analysis of a single-atom dipole trap*, Phys. Rev. A **73**, 043406 (2006).

[148] W. Alt, *An objective lens for efficient fluorescence detection of single atoms*, Optik - International Journal for Light and Electron Optics **113**, 142 (2002).

[149] R. Fischer, *Optical system design*, Second ed. (McGraw Hill, 2008).

[150] ISO-11146, *Lasers and laser-related equipment – Test methods for laser beam widths, divergence angles and beam propagation ratios*, 2005.

[151] C. Webb and J. Jones., *Handbook of laser technology and applications*, First ed. (Institute of Physics, 2004).

[152] T. Delchar, *Vacuum physics and techniques*, First ed. (Chapman & Hall, 1993).

[153] K. Weatherill *et al.*, *A versatile and reliably reusable ultrahigh vacuum viewport*, Rev. Sci. Instrum. **80**, 026105 (2009).

[154] J. Pritchard, *Cooperative Optical Non-linearity in a blockaded Rydberg Ensemble*, PhD thesis, Durham University, 2011.

[155] W. Cooke, S. Bhatti, and C. Cromer, *Spectroscopic decay-rate measurements below the laser linewidth*, Opt. Lett. **7**, 69 (1982).

[156] S. A. Bhatti and W. E. Cooke, *Power-dependent line shapes of transitions to autoionizing Rydberg states*, Phys. Rev. A **28**, 756 (1983).

[157] E. Pinnington, R. Berends, and M. Lumsden, *Studies of laser-induced fluorescence in fast beams of Sr + and Ba + ions*, Journal of Physics B: Atomic, Molecular and Optical Physics **28**, 2095 (1995).

[158] G. Fraser, *The ion detection efficiency of microchannel plates (MCPs)*, International Journal of Mass Spectrometry **215**, 13 (2002).

[159] New Focus, *MFA Series Miniature Linear Stages User's Manual.*

[160] A. Michelson and E. Morley, *On the relative motion of the Earth and the luminiferous ether*, American Journal of Science **34**, 203 (1887).

[161] P. Krishnaiah, *Analysis of variance*, First ed. (North-Holland, 1980).

[162] L. Mandel, *Sub-Poissonian photon statistics in resonance fluorescence*, Opt. Lett. **4**, 205 (1979).

[163] B. L. Morgan and L. Mandel, *Measurement of Photon Bunching in a Thermal Light Beam*, Phys. Rev. Lett. **16**, 1012 (1966).

[164] H. Paul, *Photon antibunching*, Rev. Mod. Phys. **54**, 1061 (1982).

[165] G. Box and M. Muller, *A Note on the Generation of Random Normal Deviates*, Ann. Math. Statist. **29**, 610 (1958).

[166] R. Loudon, *Quantum theory of light*, Third ed. (Oxford Science Publications, 2003).

[167] T. Liebisch, A. Reinhard, P. Berman, and G. Raithel, *Atom Counting Statistics in Ensembles of Interacting Rydberg Atoms*, Phys. Rev. Lett. **95**, 253002 (2005).

[168] T. Liebisch, A. Reinhard, P. Berman, and G. Raithel, *Erratum: Atom Counting Statistics in Ensembles of Interacting Rydberg Atoms [Phys. Rev. Lett. 95, 253002 (2005)]*, Phys. Rev. Lett. **98**, 109903 (2007).

[169] M. Viteau *et al.*, *Cooperative excitation and many-body interactions in a cold Rydberg gas*, **arXiv:1206.5086v1** (2012).

[170] F. Gounand, T. F. Gallagher, W. Sandner, K. A. Safinya, and R. Kachru, *Interaction between two Rydberg series of autoionizing levels in barium*, Phys. Rev. A **27**, 1925 (1983).

[171] W. Qiang *et al.*, *Magneto-Optical Trapping of 88 Sr atoms with 689 nm Laser*, Chinese Physics Letters **28**, 033201 (2011).

[172] J. Helmcke, S. A. Lee, and J. L. Hall, *Dye laser spectrometer for ultrahigh spectral resolution: design and performance*, Appl. Opt. **21**, 1686 (1982).

[173] A. Wilson *et al.*, *A 750 mW, continuous-wave, solid-state laser source at 313 nm for cooling and manipulating trapped* $^{9}Be^{+}$ *ions*, Applied Physics B: Lasers and Optics **105**, 741 (2011).

[174] R. P. Abel, C. Carr, U. Krohn, and C. S. Adams, *Electrometry near a dielectric surface using Rydberg electromagnetically induced transparency*, Phys. Rev. A **84**, 023408 (2011).

[175] C. G. Alzar, P. Petrov, D. Oblak, J. Mueller, and E. Polzik, *Compensation of eddy-current-induced magnetic field transients in a MOT*, **arXiv:physics/0701251v1** (2007).